Universitatea Politehnica Timișoara

HABILITATION THESIS

Toward New Frontiers for Composite Materials

Assoc. Prof. Mircea NICOARĂ, Eng. Sci. Dr.
Politehnica University Timișoara

Timișoara, 2016
(revision October 23, 2016)

Table of Content

Table of Content 2
Rezumat 4
Abstract 6
Professional and Scientific Achievements 8
Context and motivation 8
Accomplishment of minimum criteria 9
Scientific sources for the habilitation thesis 10
List of abbreviations 12
Introduction 13
Chapter 1. New Ti--based amorphous –crystalline composites for biomedical applications 16
1.1. State-of the art and tendencies in development of titanium alloys 16
1.2. Replacement of Ni as amorphization element in the new alloys 20
1.2.1. Biological effects of Ni and Ga 20
1.2.2. Gallium effect on glass forming ability (GFA) of Ti alloys 21
1.2.3. Experimental evaluation of a new Ni-free alloy 22
1.3. Replacement of Cu as amorphization element 34
1.3.1. Biological effect of copper and silver 34
1.3.2. Design of new alloy composition 35
1.3.3. Thermodynamic considerations on the master alloy 37
1.3.4. Experimental evaluation of the Cu-free alloy 39
Chapter II. Ti-based bulk metallic glass foams for biomedical applications 46
2.1. Main research directions 46
2.2. Fabrication route of the new $Ti_{42}Zr_{40}Ta_3Si_{15}$ alloy 48
2.3. Microstructural evaluation of the $Ti_{42}Zr_{40}Ta_3Si_{15}$ alloy 48
2.4. The thermal stability of $Ti_{42}Zr_{40}Ta_3Si_{15}$ alloy 58
2.5. Mechanical properties of the new porous BMG 66
2.6. Biocompatibility of the $Ti_{42}Zr_{40}Ta_3Si_{15}$ alloy 68
2.7. Conclusions 70
Chapter 3. Advanced Al-based hybrid composites 71
3.1. Basic concept 71
3.2. Hybrid Al-composites by fabricated by mean of reactive sintering 71
3.2.1. Experimental materials and investigations 72
3.2.2. Optimization of sintering parameters 77
3.2.3. Conclusions 82

Chapter 4. Advanced microstructural characterization of composites by mean of image processing 83
4.1. Basic concepts 83
4.2. Experimental materials 85
4.3. Computerized image processing method 86
4.4. Results and discussion 91
4.5. Conclusions. 95
Chapter 5. Career evolution and development prospects 96
5.1. Development of new Ti-based amorphous/crystalline composites 96
5.1.1. Optimization of compositions 96
5.1.2. Structural characterization of the Ti-Zr-Pd-Ag-Sn system 97
5.1.3. Design of fabrication technologies 97
5.1.4. Evaluation of corrosion behavior and biocompatibility 97
5.1.5. Characterization of mechanical properties 98
5.2. Bulk metallic glass foams 98
5.2.1. New BMGFs compositions and morphologies 99
5.2.2. New processing routes 99
5.2.3. Assessment of biocompatibility 100
5.2.4. Characterization of mechanical properties 100
5.3. Discontinuously reinforced Al-matrix composites 100
5.4. Applicative research for new industrial products and technologies 101
Acknowledgements 102
References 103

Rezumat

Prezenta teză de abilitare reprezintă sinteza activităților de cercetare și academice în domeniul științei și ingineriei materialelor desfășurate în perioada 1999-2016, după susținerea publică în 12 martie 1999 a tezei de doctorat cu titlul "*Contribuții la studiul compozitelor metalice armate cu particule ceramice privind producerea și modificarea structurii și proprietăților prin prelucrare mecano-termică*"

Contribuțiile științifice prezentate urmăresc cele mai recente evoluții de la clasicul concept de material compozit cu matrice metalică ușoară (Al, Ti etc.) armat discontinuu cu particule ceramice de dimensiuni microscopice, produse prin procedee convenționale de turnare sau de metalurgia pulberilor, către noi frontiere științifice.

În acest spirit, *Capitolul I* al tezei sintetizează contribuțiile științifice aduse la dezvoltarea compozitelor pe bază de Ti, având matrice amorfă și faze secundare de tip cristalin, pentru aplicații biomedicale. Două mari direcții de cercetare s-au concretizat până acum în acest domeniu. Prima dintre ele este reprezentată prin dezvoltarea unui nou aliaj de titan, având structură compozită amorf/cristalin, obținut prin înlocuirea adaosurilor de Ni, notoriu pentru efectele dăunătoare asupra organismului uman, cu mici adaosuri de Ga. Noul aliaj $Ti_{41.5}Zr_{2.5}Hf_5Cu_{37.5}Ga_{7.5}Si_1Sn_5$ produs sub formă de sârme cu diametru de 2 și 3 mm, fabricat prin *suction casting*, are o structură foarte complexă de compozit amorf/cristalin, matricea amorfă înglobând mai multe faze cristaline, mergând de la dendrite de dimensiuni relativ mari la nano-cristale foarte fine, de aproximativ 10 nm. Cea de a doua direcție de cercetare urmărită o reprezintă dezvoltarea unor compozite pe bază de Ti pentru aplicații de tipul implanturilor ortopedice, fără conținut de Cu, având în vedere efectele citotoxice bine documentate ale acestui element, care a fost înlocuit cu Ag. Aliajul nou proiectat $Ti_{42}Zr_{10}Pd_{14}Ag_{26}Sn_8$, produs prin răcirea ultra-rapidă a topiturii, prezintă o structură microcristalină complexă, având matrice reziduală amorfă. Noul aliaj are câteva caracteristici promițătoare pentru utilizarea ca biomaterial, având în vedere efectul bactericid al Ag metalic și caracterul compozit amorf-cristalin, cu potențial pentru proprietăți mecanice superioare, inclusiv o ductilitate ameliorată față de sticlele metalice masive.

Capitolul al II-lea prezintă contribuțiile științifice din care a rezultat dezvoltarea unor noi materiale poroase, considerate de unele personalități din domeniu ca fiind de asemenea materiale compozite. Un nou biomaterial cu bază de Ti a fost produs folosindu-se un proces avansat, care combină producerea de benzi amorfe prin *melt-spinning* cu procesarea prin metalurgia pulberilor. Aliajul rezultat $Ti_{42}Zr_{40}Ta_3Si_{15}$ are proprietăți remarcabile, ca de exemplu porozitate de 14 vol%, rigiditatea aproximativ 52 GPa, apropiată de modul Young al osului cortical, care este între 4 și 30 GPa, rezistența la compresiune de peste 337 GPa și o bună biocompatibilitate în lichid corporal simulat. După știința noastră, acesta este primul aliaj biocompatibil amorf masiv având proprietăți mecanice apropiate osului uman, fapt subliniat de revizorii *Acta Biomaterialia,* în care s-au publicat rezultatele.

Noile frontiere tehnologice în fabricarea compozitelor pe bază de Al, ranforsate cu particule ceramice sunt sintetizate în *Capitolul al III-lea*. Cercetările în domeniu s-au concentrat mai ales pe compozitele hibride pe bază de Al produse printr-o metodă tehnologică inovativă. Noile compozite au două tipuri de ranforsanți, primul dintre ele este format de alumina introdusă prin înglobare, folosindu-se procedee clasice de metalurgia pulberilor, iar cea de a doua fracțiune de alumină este produsă prin metode *in-situ*, în particular tratamente de sinterizare reactivă.

Cel de al *IV-lea Capitol* ilustrează prin exemple aplicarea procesării computerizate a imaginilor pentru analiza distribuției de particule la unele compozite

cu matrice de Al având ranforsare discontinuă. Această tehnică avansată de investigație permite interpretarea obiectivă a imaginilor microstructurale obținute prin microscopie optică sau electronică, precum și aplicarea metodelor statistice la caracterizarea și optimizarea distribuției de particule, care este responsabilă pentru unele proprietăți critice ale compozitelor, în special ductilitatea și tenacitatea. Analiza a fost realizată pentru a evalua transformările morfologice într-un compozit cu matrice de Al ranforsat cu particule de SiC, produs prin metalurgia pulberilor, pe parcursul procesării secundare prin deformare plastică de grad ridicat.

Producerea materialelor experimentale pentru cercetările prezentate în această teză a fost realizată prin utilizarea unor metode de procesare avansată sau inovativă, ca de exemplu topirea cu arc, turnarea prin presiune sau depresiune, *melt spinning*, precum și tehnici din metalurgia pulberilor, de tip *cryo-milling, presare la cald* și *sinterizare reactivă.* La caracterizarea materialelor s-au folosit *metode* avansate de investigație ca de exemplu analiză calorimetrică diferențială (*DSC*), difracție cu raze X (*XRD*), atât de tip convențional cât și cu radiație sincrotron, microscopie electronică cu baleiaj (*SEM*), microscopie electronică prin transmisie de înaltă rezoluție (*HR-TEM*). Pachete software speciale s-au folosit pentru procesare computerizată a imaginilor microstructurale (microscopie optică, SEM), procesarea curbelor DSC și a spectrelor XRD, proiectarea aliajelor, încercări mecanice, statistică, reprezentare grafică etc.

Rezultatele științifice din domeniul științei și ingineriei materialelor au fost publicate în reviste de prestigiu precum *Intermetallics, Acta Biomaterialia, Acta Materialia, Materials, Journal of Thermal Analysis and Calorimetry, Metall, Journal of Magnetism and Magnetic Materials* sau au fost incluse în volumele unor conferințe internaționale.

Direcțiile de cercetare ilustrate în prezenta teză sunt prevăzute a fi continuate în contextul evoluției viitoare a carierei, în dezvoltarea unor noi compozite cu bază de Ti pentru aplicații biomedicale, care trebuie caracterizate în mod comprehensiv, din punctul de vedere al biocompatibilității și a unor proprietăți mecanice corespunzătoare. O atenție specială va fi acordată compozitelor pe bază de Al, pentru aplicații structurale care presupun proprietăți mecanice superioare asociate unei greutăți specifice reduse. Colaborarea cu firmele industriale prin contacte de cercetare aplicativă va fi de asemenea continuată.

Abstract

The present habitation thesis represents a synthesis of scientific and academic activity in the field of materials science and engineering for the period between 1999 and 2016, after the public defense in March 12, 1999 of the Ph.D. thesis with title "*Contributions to the study of metal matrix composites reinforced with ceramic particles regarding fabrication and changes of structure and properties by mean of heat treatments*".

Scientific contributions that are presented follow the latest evolutions from the classic concept of composite material with light metallic matrix (Ti, Al etc.) discontinuously reinforced with micron-sized ceramic particles, produced by mean of conventional casting or powder metallurgy techniques, toward new scientific frontiers.

In this respect, the *1st Chapter* of the thesis syntheses the scientific contributions for development of Ti-based composites with amorphous matrix and crystalline secondary phases for biomedical applications. Two main directions of researches have been so far concretized in this field. The first direction is represented by the development of a new Ni-free titanium alloy with composite amorphous/crystalline structure, which was achieved by replacement of Ni, which is notorious for its harmful effects to human body, with minor addition of Ga. The new $Ti_{41.5}Zr_{2.5}Hf_5Cu_{37.5}Ga_{7.5}Si_1Sn_5$ alloy fabricated as 2 and 3 mm rods by mean of suction casting method has a very complex structure of an amorphous/nano-crystalline composite, the amorphous matrix embedding several crystalline phases, ranging from relatively large-sized dendrites to very fine nano-crystals of about 10 nm. The second direction that was followed was represented by development of new Ti-based composites without any Cu-content, for applications as orthopedic implants, considering the well-established cytotoxic effect of this element, which was replaced with Ag. The newly designed alloy $Ti_{42}Zr_{10}Pd_{14}Ag_{26}Sn_8$ fabricated by ultra-rapid melt cooling shows a complex microcrystalline structure, with residual amorphous matrix. The new alloy has some promising features for use as biomaterial, considering the bactericidal effect of metallic Ag and the composite amorphous – crystalline character with potential for high mechanical properties, including an ameliorated ductility in comparison with the BMGs.

The *2nd Chapter* presents the scientific contributions that resulted in development of new porous materials, which are considered to be also composite materials by some leading opinions. A new biomaterial with Ti-based amorphous matrix was fabricated using an advanced technique that combines melt-spinning of amorphous ribbons followed by powder metallurgy processing. Resulting $Ti_{42}Zr_{40}Ta_3Si_{15}$ amorphous material has some outstanding properties such as 14 vol% porosity, the rigidity around 52 GPa, close to the Young's modulus of cortical bone, which is between 4 and 30 GPa, a compressive strength higher that 337 GPa and good biocompatibility in simulated body fluid. To our knowledge this is the first biocompatible Ti-based bulk glassy alloy having mechanical properties close to human bone, as underlined by the reviewers of *Acta Biomaterialia*, where the results were published.

New processing frontiers for fabrication of Al-based composites reinforced with ceramic particles are summarized in the *3rd Chapter*. Researches in this field have been focused mainly on new hybrid Al-based composites produced by mean of an innovative fabrication method. The new composites have two types of reinforcements, the first one is alumina introduced by embedment, using classical powder metallurgy techniques, and the second fraction of alumina particles is produced by *in-situ* methods, particularly reactive sintering treatments.

The 4th Chapter illustrates with examples the application of computerized image processing to the analysis of reinforcement distribution for some discontinuously reinforced aluminum matrix composites. This advanced investigation technique allows objective interpretation of microstructural images obtain by light or electronic microscopy, as well the use of statistical methods for characterization and optimization of particle distribution, which is responsible for some critical properties of the composites, especially ductility and toughness. The analysis was performed to evaluate morphological changes in reinforcement distribution for a composite with Al-matrix reinforced with SiC particles, produced by powder metallurgy, during secondary processing by mean of high-ratio plastic deformations.

Fabrication of experimental materials for the researches presented in this thesis was accomplished using some advanced or innovative processing techniques, such as arc-melting, ultra-rapid cooling by mean of suction or pressure casting, melt spinning, as well as powder metallurgy techniques like cryo-milling, hot pressing, and reactive sintering. Materials characterization was performed with some advanced investigation methods like differential scanning calorimetry (DSC), X-ray diffractions (XRD), both conventional and using synchrotron radiation, scanning electron microscopy (SEM), high resolution transmission electron microscopy (HR-TEM). Special software programs were used for computerized image processing of microstructural images (light microscopy, SEM), processing of DSC curves, XRD spectra, alloy design, material testing, statistics, graphic representation, etc.

The scientific achievements in the field of materials science and engineering were published in prestigious journals with large impact on the research community, such as *Intermetallics*, *Acta Biomaterialia*, *Acta Materialia*, *Materials, Journal of Thermal Analysis and Calorimetry*, *Metall*, *Journal of Magnetism and Magnetic Materials*, or included in the proceedings of international conferences.

The research directions that are presented in the thesis are envisioned to be continued in the context of future career evolution, for development of new Ti-based composites for biomedical applications, which should be also comprehensively characterized, regarding biocompatibility and appropriate mechanical properties. Special attention will also be given to Al-based composites for structural applications that require high mechanical properties associated with low specific weight. Collaborations with industrial companies within applicative research contracts will be also continued.

Professional and Scientific Achievements

Context and motivation

The field of advanced and engineering materials has been the main objective in the academic and research activity throughout a professional career of over 25 years.

The teaching subjects of courses and practical laboratories that were conducted during these period were focused almost exclusively on disciplines dealing with fabrication, processing and characterization of materials at the Politehnica University Timisoara (PUT): Powder metallurgy, Composite materials, Heat treatments, Materials science, Particulate and cellular materials etc. Teaching activities have been also performed in French as invited professor at the University of Reims Champagne-Ardennes (*Science des matériaux*), in German at the Robotics specialty of the PUT (*Werkstoffwissenschaft*), and in English at the Politehnica International department of the PUT (*Materials science*) or for international summer schools (*Metallic foams, Al-based composites*).

The fundamental research has ranged over many topics of materials science and engineering: Al-based alloys and composites, Ti-based amorphous alloys and amorphous/crystalline composites, magnetic materials, stainless steels and superalloys, cellular materials, Cu-based alloys etc. Important research activities have been related to the effects produced on materials by the different processing methods: conventional, reactive or selective laser sintering, hot deformation, induction heating, welding, brazing, ultra-rapid casting etc. The research has been supported by 13 research grants, 3 of them international (1 as director) and 10 of them national (2 as director). Another 3 research contracts (value over 10.000 Euro) were coordinated for the benefit of industrial companies.

Applicative research in the field of engineering materials and industrial processing technologies has been concretized in more than 100 contracts, the majority of them in capacity of director (3 of them having a value over 10.000 Euro) with prestigious companies of divers specific: automotive (*Continental Automotive Romania, Continental Automotive Products, Contitech Romania, Dura Automotive, Hella Romania, Leman Industrie, TRW*), electronics (*Kathrein, Elster Rometrics, Flextronics, Regenersis*), industrial and railway equipment (*Sysmec*, *Mahle, Maschio Gaspardo, Astra Rail Industries)* home appliances (*Zoppas Industrie Romania, Elba)*, energy production (*Hidroelectrica, Hidroserv),* etc. The subject of these contracts were technical assistance for development of new products, investigations of non-conformities or failure analysis, assimilation or optimization of processing technologies, improvement of quality assurance, audit for production lines or laboratories, etc.

International cooperation has been an important way for career development by mean of research or teaching mobilities, joint research programs, co-organizing of conferences, seminars and summer schools. Relevant collaborations have been established with universities or institutions like: *Leibniz Institute for Solid State and Materials Research Dresden, TU Dresden, University of Reims Champagne-Ardennes, University of Lille, University Federico II Napoli, University of Applied Sciences Düsseldorf, University of Quebec at Trois-Rivières, Technical University Cluj-Napoca* etc.

Scientific activity resulted in 22 ISI articles, 9 of them as first author. Among these contributions 10 are articles in ISI Thomson Reuters journals, and 7 have an impact factor greater than 0.5, ranging from 1.97 to 6.025. Another 14 articles are indexed in relevant international databases.

The professional activity was completed with managerial activities at the Politehnica University Timisoara, as responsible of license of master programs (Materials science, Advanced Materials and Technologies), member of the board of domain or specialization (Industrial engineering, Medical engineering), director of department (2007-2016, department of Materials and Fabrication Engineering), member of the council of the Mechanical Engineering Faculty (2007-2016). The experience of auditing academic programs has been exercised since 2012 as permanent expert in the 1st Commission for Engineering Sciences of ARACIS (Romanian Agency for Quality Assurance in Higher Education).

Minimum criteria of CNATCDU to support habilitation thesis are accomplished or exceeded.

Accomplishment of minimum criteria

<table>
<tr><th colspan="3">Minimum criteria</th><th>Minimum requested</th><th>Accomplished</th></tr>
<tr><td colspan="3">A1. Teaching & training</td><td>40</td><td>161</td></tr>
<tr><td colspan="3">A2. Research</td><td>300</td><td>499</td></tr>
<tr><td colspan="3">A3. Recognition & activity impact</td><td>60</td><td>316</td></tr>
<tr><td colspan="3">TOTAL (A)</td><td>400</td><td>976</td></tr>
<tr><td colspan="3">Mandatory minimum terms subcategories</td><td>Minimum requested</td><td>Accomplished</td></tr>
<tr><td colspan="3">A.1.1.1. Books / chapters in specialized books as author (1 as first author)</td><td>2 (1)</td><td>4 (1)</td></tr>
<tr><td colspan="3">A.1.2.1. Didactic textbook</td><td>1</td><td>2</td></tr>
<tr><td colspan="3">A.1.2.2. Laboratory guidance / applications</td><td>1</td><td>3</td></tr>
<tr><td colspan="3">A.2.1. Articles ISI Thomson Reuters journals & proceedings</td><td>15</td><td>22</td></tr>
<tr><td rowspan="3">Of which</td><td colspan="2">A.2.1.2 Articles in ISI Thomson Reuters journals</td><td>10</td><td>10</td></tr>
<tr><td colspan="2">A.2.1.2 Articles in ISI Thomson Reuters journals min. 0.5 impact factor</td><td>5</td><td>7</td></tr>
<tr><td colspan="2">A.2.1.2 Articles in ISI Thomson Reuters journals as main author, regardless of the impact factor</td><td>5</td><td>5</td></tr>
<tr><td colspan="3">A.2.2 Articles in journals and volumes of scientific events indexed in international databases</td><td>5</td><td>18</td></tr>
<tr><td colspan="3">A.2.4 Research grants (in competition)</td><td>3</td><td>3</td></tr>
<tr><td rowspan="2">A.2.4.1.2 As director/responsible</td><td colspan="2">International grant</td><td rowspan="2">3</td><td>1</td></tr>
<tr><td colspan="2">National grant</td><td>2</td></tr>
<tr><td rowspan="2">A.2.4.2 As member/participant</td><td colspan="2">International grant</td><td rowspan="2">-</td><td>4</td></tr>
<tr><td colspan="2">National grant</td><td>6</td></tr>
</table>

Scientific sources for the habilitation thesis

The scientific content of the habilitations thesis represents a summary of papers published in journals indexed by ISI or other international databases. Information from presentations at some international conferences, and included in volumes of proceedings were also used.

[1] **M. Nicoara**, L. R. Cucuruz and I. Cartis, " Partikelverstäkter Verbundwerkstoffe – Particle-reinforced composites," *Metall,* no. 1-2, pp. 30-36, 2000.

[2] **M. Nicoara** and A. Raduta, "The Effect of Particle Reinforcement upon Precipitation of Secondary Phases in Composites with Aluminum Matrix," in *Summer School on Mechanical Spectroscopy Q-1*, Aussois, France, 2002.

[3] **M. Nicoara,** A. Raduta, C. Locovei and V.-A. Serban, "Contributions to Thermo-Mechanical Processing of Al-Based Particle-Reinforced Composites," in *Proceedings of the International Colloquium of the European Centre For Emerging Materials And Processes Dresden ECEMP 2010*, Dresden, 2010.

[4] M. Lita, M. Nicoara, “The Use of Amorphous And Quasi-Amorphous Fe–Cr–P-Powder for Fabrication of Magnetic Rheological Suspensions”, *Journal of Magnetism and Magnetic Materials*, vol. 201, pp. 49-52, 1999.

[5] A. Raduta, **M. Nicoara**, C. Locovei, J. Eckert and M. Stoica, "Ti-based bulk glassy composites obtained by replacement of Ni with Ga," *Intermetallics*, vol. 69, pp. 28-34, 2016.

[6] A. Raduta, **M. Nicoara**, C. Locovei, M. Stoica and J. Eckert, "About Replacement of Nickel as Amorphization Element for Fabrication of Ultra-Rapidly Solidified Ti-Zr Alloys," in *Solid State Phenomena - Advanced Materials and Structures V*, Zurich, 2014.

[7] C. Locovei, **M. Nicoara** and A. Raduta, "Sample Preparation and HR-TEM Investigation Techniques of Ti Based, Ga Containing, Amorphous Alloys," in *Solid State Phenomena - Advanced Materials and Structures V*, Zurich, 2014.

[8] **M. Nicoara**, C. Locovei, V. A. Serban, R. Parthiban, M. Calin and M. Stoica, "New Cu-Free Ti-Based Composites with Residual Amorphous Matrix," *Materials*, vol. 331, no. 9, pp. 1-14, 2016.

[9] **M. Nicoara**, A. Raduta, R. Parthiban, C. Locovei, J. Eckert and M. Stoica, "Low Young’s modulus Ti-based porous bulk glassy alloy without cytotoxic elements," *Acta Biomaterialia*, vol. 36, pp. 323-331, 2016.

[10] **M. Nicoara**, A. Raduta, C. Locovei, D. Buzdugan and M. Stoica, "About Thermostability of Biocompatible Ti-Zr-Ta-Si Amorphous Alloys", *Journal of Thermal Analysis and Calorimetry*, vol. 124, pp. 1-7, 2016.

[11] A. Raduta, **M. Nicoara** and C. Locovei, "About Thermostability of Fe-Ni-P Amorphous Alloys", in *Solid State Phenomena-Advanced Materials and Structures IV*, Zurich, 2012.

[12] G. Thalmaier, I. Vida-Simiti, N. Jumate, V. A. Şerban, C. Codrean, **M. Nicoara** and L. Bukkosi, "Thermal Stability of $Ni_{40}Ti_{40}Nb_{20}$ and $Ni_{32}Ti_{48}Nb_{20}$ Tapes Obtained by Rapid Solidification Technique", in *Solid State Phenomena - Advanced Materials and Structures IV*, Zurich, 2012.

[13] **M. Nicoara,** C. Locovei, C. Opris, D. Ursu, R. Vasiu and M. Stoica, "Optimizing the parameters for in-situ fabrication of hybrid al-Al_2O_3 composites" *Journal of Thermal Analysis and Calorimetry*, on-line, 2016.

[14] **M. Nicoara**, A. Raduta and C. Locovei, "Computerized Image Processing for Evaluation of Microstructure in Metallic Matrix Composites" *Solid State Phenomena,* vol. 188, no. Advanced Materials and Structures IV, pp. 124-133 , 2012.

[15] **M. Nicoara**, A. Raduta and C. Locovei, "Computer-aided evaluation of particle distribution in metallic matrix composites" in *Proceedings of the European International Powder Metallurgy Congress and Exhibition - Euro PM 2011*, Barcelona, 2011.

[16] C. Locovei, **M. Nicoara**, A. Raduta and V.-A. Serban, "Contributions to computer-aided evaluation of microstructure for particle reinforced composites by mean of image processing" in *Proceedings of the 4th International Conference "Advanced Composite Materials Engineering"* , Brasov, 2012.

List of abbreviations

AMC - Aluminum matrix composite
BMG – bulk metallic glass
BMGF – bulk metallic glass foam
BSE - back-scattering electrons
DSC - differential scanning calorimetry (calorimeter)
DRAMC - discontinuously reinforced aluminum matrix composite
EDX/EDAX - energy-dispersive X-ray analysis
GFA – glass forming ability
HIP – hot isostatic pressing
HR-TEM – high-resolution transmission electron microscopy
ICDD PDF4+ - International Center for Diffraction Data Powder Diffraction File
IFW - Leibniz Institute for Solid State and Materials Research Dresden
MMC – metal matrix composite
OM - optical microscopy
SBF - simulated body fluid
PM – powder metallurgy
PUT – Politehnica University Timisoara
SE – secondary electrons
SEM - scanning electron microscopy
SLR - supercooled liquid region
SPS - spark plasma sintering
STEM - scanning transmission electron microscopy
T_g - glass transition temperature
T_{rg} - reduced glass transition temperature
T_{liq} - temperature of the liquidus point
TMA - thermomechanical analysis
XRD – X-rays diffraction

Introduction

Development of composite materials has been accompanied over the time with a very complex evolution of the definitions and classifications corresponding to this vast class of materials. Following this spectacular evolution, the classic definition of composite materials, i.e. "*a composite material is a macroscopic combination of two or more distinct materials, having a recognizable interface between them*" [17], elaborated by the American Society of Materials in 2001 looks almost entirely obsolete.

Significant changes have been accumulated in the field of particle reinforced composites. The classical combinations of light metallic matrix and micrometer-sized ceramic reinforcements, the latter embedded by mean of *ex-situ* methods, based on casting or powder metallurgy [1], [2], have been replaced by new creative solutions. Some of them are related with the scientific contributions described by the present thesis:

I. Researches for improving the properties of bulk metallic glasses (BMGs), especially for biomedical applications, eventually evolved in development of new *in-situ* composites consisting in a metallic amorphous matrix containing different dispersed phases, as seen schematically in Figure 1 [18].

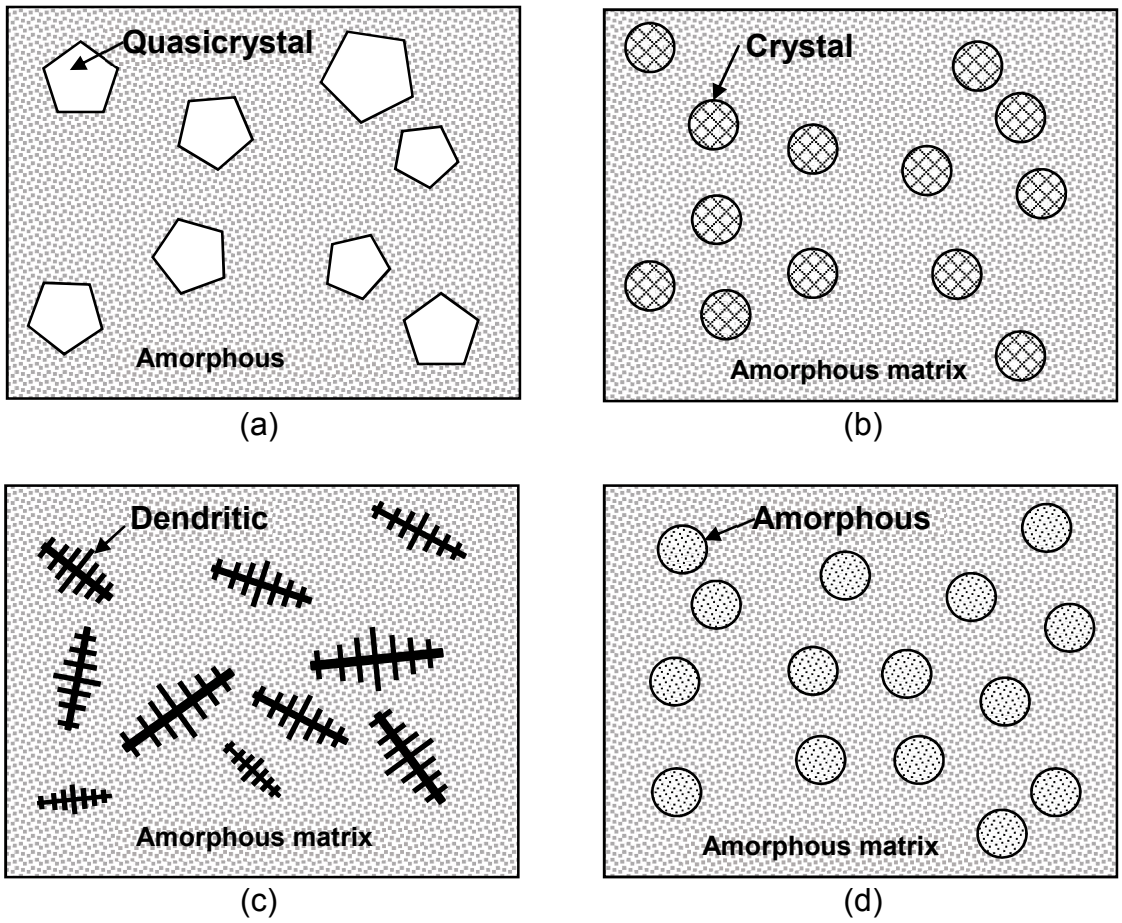

Figure 1. Schematic representation of microstructures of *in situ* composites with amorphous matrix and different second phase dispersions: (a) quasicrystalline phase, (b) spherical shaped nano-micrometer-sized crystals, (c) dendritic phase, and (d) second amorphous phase (after [18]).

The main benefit of this approach is ductilization of BMGs [19], mainly in the case of Ti- and Zr-based composites, in order to take full advantage of higher mechanical properties (high strength, low rigidity) and better corrosion resistance of this advanced class of materials. Original contributions to this particular direction for composite development by mean of rapid cooling techniques will be presented in Chapter 1. The newly formulated alloys have the benefit of better compatibility, since they do not contained allergenic Ni [5], or are also free of Cu [8], which is frequently used as amorphization element for Ti, although has a well-established cytotoxic effect.

II. Although Ti-alloys still represent the first choice for medical implants, an important drawback still persists, which is a higher rigidity than the cortical bone. This fact is responsible for reduction of bone density, and represents one of the important cause for implant failure. A possible solution to that problem is represented by metallic alloys with controlled porosity [20], which are also considered as *composite materials* by some leading opinions [21]. In this respect, Chapter 2 presents some scientific contributions to the development of a new $Ti_{42}Zr_{40}Ta_3Si_{15}$ porous BMG that, to our knowledge, is so far the first bulk metallic glass foam (BMGF) totally free of any harmful elements and having a Young's modulus close to the human bone [9].

III. Metal matrix composites (MMCs) still represent an interesting alternative as structural materials when high mechanical properties should be associated with low specific weight. The most promising direction, for both economic and technological reasons, is represented by the composites with aluminum matrix reinforced by ceramic particles, also called discontinuously reinforced aluminum matrix composites (DRAMCs). In spite of considerable increase of mechanical properties and other advantages, such as vibration damping capacity, reduction of thermal expansion or possible improvement of fatigue behavior, some challenges still stand in front of researchers, especially inferior low ductility and toughness, as well the inability to predict the corrosion behavior [21], [22].

The role of reinforcement is of utmost importance for increasing the mechanical properties of DRAMCs, since strengthening is very complex and could be explained by several different mechanisms [23] :

- "Dislocation-pinning" or "Orowan strengthening", when motion of dislocations inside metallic matrix is impeded by small, hard particles;
- Load transfer between matrix and reinforcement;
- Formation of dislocations resulting from the mismatch of elastic modulus and coefficient of thermal expansion between the hard particles and the metal matrix;
- "Hall-Petch strengthening", which results from refinement of metallic grains and impeding dislocation mobility, as effect of higher proportion of reinforcement and reduced particle diameter.

Therefore recently researches are usually focused on improvement of reinforcements and their effect on properties. Consequently original contributions that are presented in Chapter 3 are consonant with two important development directions:

- Hybrid composites, which are using 2 or more types of reinforcement, with different composition, size, shape, microstructure etc.
- *In-situ* formation of reinforcing phases, as alternative to embedment of micrometer-sized synthetic ceramics (Al_2O_3, SiC, B_4C, WC, SiO_2 etc.). Resulting reinforcing phases are defect-free, have dimensions in sub-micrometer or even nano-meter range and could have more uniform distribution. Since the reinforcement is formed within the matrix, the interface between them is more stable and free of impurities, providing good bonding [24] [25].

IV. One of the most important issue regarding the advanced characterization of DRAMCs is related with the reinforcements, above all uniform distribution of particles inside the metallic matrix, which is critical for some properties like ductility and toughness. Quantitative evaluation of particle distribution is addressed in Chapter 4, using the computerized processing of microstructural images, with some examples of composites produced by mean of classic *blending-pressing sintering* techniques.

The results of researches suggests that changes in particle distribution, and above all removal of particle clustering, could be evaluated quantitatively by mean of image processing, and furtherly processed with statistical tools, which allows precise and objective optimization of the plastic deformation techniques, for further improvement of mechanical properties.

Chapter 1. New Ti--based amorphous –crystalline composites for biomedical applications

1.1. State-of the art and tendencies in development of titanium alloys

Due to major challenges for specific properties, the development of biocompatible materials for orthopedic and dental applications has attracted considerable interest among researchers. From mechanical point of view, such materials must have high mechanical strength associated with low Young's modulus, similar with cortical bone, in order to avoid stress shielding effect of orthopedic implants and degradation of mineral density in patient's bone (osteopenia) [26] [27] [28]. Moreover, acceptable ductility and wear resistance are also desirable for both orthopedic and dentistry applications [29] [30] [31]. Since these materials are also required to operate for long periods in some very specific conditions provided by human organism, e.g. they should be resistant to bio-corrosion and must promote development of new cells and tissues without any toxic, irritating, inflammatory or allergic reactions, which could be produced if harmful elements are released [32].

Titanium alloys still rise the highest research interest among biomaterials for orthopedic and dental applications since they possess the most favorable combination of properties [28], [33], [34], In terms of mechanical properties, titanium alloys have good mechanical strength and ductility [35], as well as acceptable wear resistance [36]. They also have excellent resistance to bio-corrosion [36], they stimulate the proliferation of new cells and tissues [33], and reported incidence of adverse toxic, irritating, inflammatory or allergic reactions produced by released elements is relatively moderate [33]. Therefore, over the years, some titanium alloys like Ti-6Al-4V and Ti-6Al-7Nb became standard solution for medical implants [33]. In spite of undeniable advantages, classical crystalline alloys based on titanium still present some inadequate properties: certain alloying elements such as vanadium, aluminum, nickel, etc. could release harmful metallic ions inside human body, having well established allergenic or cytotoxic effects [37], [38]. They also have considerable higher rigidity than cortical bone, which is responsible for stress shielding effect of orthopedic implants and degradation of mineral density in patient's bone. For example, commercially pure titanium has the rigidity of approximately 100 GPa, while stainless steel, tantalum and cast Co-Cr alloys have more than 200 GPa. Ti-6Al-4V alloy, which became over the years the most popular for fabrication of implants because of its high mechanical properties and moderate price, has the Young's modulus around 112 GPa, many times higher than human bone, which has values between 4 and 30 GPa [28], [29], [32], [33], [39]. Another persistent problem is that they still present relatively low bioactivity in relation with human tissues [33], [35], [36], [38], [40].

Development of the Ti-based glassy alloys based on rapid cooling techniques revealed some considerable improvements in comparison with the already classical Ti-6Al-4V and Ti-6Al-7Nb crystalline compounds [41]. It has been proved that the lack of grain boundaries, as well as of segregations and other structural heterogeneities, enhances corrosions resistance and improves mechanical properties such tensile strength and wear resistance [42]. At the same time such metallic glasses have lower Young's Modulus than crystalline alloys, correlated with high elastic strain limit of approximately 2%, which is almost double than similar crystalline metallic alloys [43]

Attempts to improvement of mechanical properties eventually lead to development of new titanium based alloys. For example, both titanium β alloys and bulk metallic glasses (BMGs) received considerable attention in recent decades. While alloying with β-stabilizing systems, containing Nb, Zr, Ta, Fe, Cr, Mo, etc. may reduce

modulus under 80 GPa, processing and microstructure control, as well as fabrications costs still remain problematic [29].

Development of titanium based BMGs fabricated by mean of rapid cooling techniques open new opportunities, since amorphous alloys have no grains, boundaries, dislocations and other discontinuities, and therefore display higher mechanical strength and corrosion resistance. On the same time, since their deformation mechanism are different in comparison with crystalline alloys, they have a unique combination of high yield strength and lower Young modulus.

Metallic glasses could offer also technological advantages based on their good formability. Plastic deformations could be performed at high ratio at temperature levels between glass transition (*Tg*) and crystallization (*Tx*), similar to thermoplastic forming [42]. This special feature has been valorized for massive amorphous alloys with thickness over 1 mm, called bulk metallic glasses (BMGs), allowing fabrication of components with complex shapes by mean of different deformation methods [42], [44], [45]. Very recently, it was shown that bulk porous Ti-based BMGs, replicating the topological features of the cortical human bones and with mechanical properties close to them, can be successfully prepared by thermoplastic forming of amorphous alloy powders [9].

The metallic glasses were discovered only in the last half century [46]. Among them, the titanium-based amorphous alloys are newcomers [47]. The first Ti-based amorphous alloys produced by rapid cooling were based on a Ti-Zr system with various additions of harmful transition metals [48]. They were reported in 1993 and in 1994 the first titanium based BMG with the composition Ti-Zr-Ni-Be was patented [49]. Many progresses in alloy design of Ti-based BMGs were recorded beginning with 1998, such as development of some alloying families as Ti–Ni–Cu–(Zr, Be) [50], Ti–Ni–Cu–(Sn, Si) [51] [52] [53] , Ti-Zr-Be-(Cr, Al, Ni, Fe) [54] [55] [56] etc. Researches have been constantly focused on larger critical dimensions for amorphous samples, enhanced mechanical properties and improved biocompatibility. One of the largest rod diameters that have been achieved so far for Ti-based glasses (i.e. 14 mm) are credited to the $Ti_{40}Zr_{25}Cu_{12}Ni_3Be_{20}$ alloy fabricated in 2005 [50]. More recently (in 2010), a new $(Ti_{41}Zr_{25}Be_{28}Fe_6)_{91}Cu_9$ alloy with an exceptionally critical size larger than 32 mm was synthesized [57]. In spite of their exceptional GFA these families of alloys have been subject to strong criticism because of the presence of alloying elements such as Be or Ni, considered to be detrimental to human health [38] [32].

One of the alloy class with relatively good GFA, allowing the fabrication of rods with diameters up to 10 mm, is grounded on the Ti-Zr-Cu-Pd family. The glassy alloys were developed by Inoue and co-workers in 2007 [58] based on a $(Ti\text{-}Zr)_{50}(Cu\text{-}Pd)_{50}$ concept [41]. The main purpose of this new approach was to eliminate nickel and beryllium, which are known to substantially improve the GFA of titanium-based metallic alloys, but in the same time some of the most allergenic elements (i.e. Ni) or with well documented cytotoxic effects (i.e. Be) [59]. This direction for development of BMGs has been followed by many researchers and improvements of both mechanical properties and GFA have been achieved so far by mean of additional alloying with small proportions of elements such as Sn, Si, Ta, Nb, Co or In [41], [58], [60] [61], [62], [63], [64], [65], [66], [67]. The newly developed BMGs in the Ti-Zr-Cu-Pd system represent an important progress regarding possible biomedical applications, since they also have high corrosion resistance, mechanical strength up to 2000 MPa, and Young's modulus as low as 80 GPa [65], [68], [69]. Although biocompatibility seems to be improved in comparison with classic amorphous alloys Ti-6Al-V and Ti-45Ni [70], the most serious problem consists in the presence of copper, which is considered

highly cytotoxic and could not be completely replaced so far as amorphization element with other biocompatible additions.

In spite of considerable progresses in terms of properties, some drawbacks of BMGs still persists. Although localized deformation inside metallic glasses may be considerable, at macroscopic level ductility is low. Therefore, latest developments are based on the concept of “bulk metallic glass composites” providing broad range of mechanical properties, with different combinations of strength and ductility. The amorphous matrix of metallic alloy is reinforced with different forms of second phase particles, such as nano-sized quasi-crystals, crystalline phases at nano- or micrometer-size, dendritic crystals, or even a secondary amorphous phase [18]. Moreover, the lower amorphization capacity of some alloying elements (other than Ni or Be) could be also interesting for fabrications of nano or ultra-fine grained materials, considered to be the possible next generation of biomaterials [29]. Smaller grains means that proportion of atoms located at grain surface is considerable higher, therefore such alloys have greater surface energy and present roughness profiles down to nanometer scale. This fact is promoting better biocompatibility because bone-forming cells have higher affinity to nano-roughness, similar to natural inorganic components of bone, ranging between 20 to 80 nm long and 2 to 3 nm in diameter [29].

One of the utmost important issue for development of new alloys is the biological safety of alloying elements, which are used to improve the glass forming ability (GFA) or other microstructural properties, since resulting titanium-based alloys should be resistant to bio-corrosion and should not be harmful to human body. Over the years, a large number of additions have been used to increase the critical diameter of BMGs. However many compositions are releasing toxic and even highly toxic ions. Nickel is still use for its high amorphization capacity, but his allergenic effect as well as suspicions over its genotoxicity, carcinogenicity, and potential mutagenicity to human body are known for many years [71], [72], [73]. Other elements like Co, Cr, Fe, Mo, V and Mn cause severe adverse tissue reactions, while Zn and Be are one of the most cytotoxic elements. Discovery of Ni-free BMGs based on the Ti-Cu-Zr-Pd was considered a major breakthrough for fabrication of BMGs [58], but presence of large amounts of Cu gives high sensitivity to pitting corrosion, while highly cytotoxic effect of Cu is well documented [74] [75] . Design of new biocompatible Ti-based alloys is now based on a list of non-recommendable or “toxic” alloying additions, as well as a list of elements seen as non-problematic, also called “vital”. The first list usually contain Be, Al, Mo, V, Cr, Mn, Fe, Co, Ni, Cu, Zn, Ag, while “eligible” alloying elements may contain Nb, Ta, Zr, Si, Sn, Pd, In, Sr, B, Ca, and Mg [76] [38] [77].

So far none of the alloying elements that could be accepted as not harmful could provide enough GFA for amorphization of Ti-based alloys, in order to fabricate by rapid cooling some components with critical dimension over 1mm. Therefore, development of new amorphous alloys was focused on producing amorphous ribbons with biocompatible Ti-based compositions, and additions of Zr, Si, Ta, Pd, Nb, usually by melt spinning techniques [78], [79], [80], [81]. Resulting alloys have good in vitro biocompatibility response, as well as better electrochemical stability and very low cytotoxicity, in comparison to amorphous alloys containing Cu, Ni or Al, which highly recommended them for biomedical applications [82] [83]. Amorphous ribbons could be subsequently processed via powder metallurgy.

One of the most important technological problem to be solved is that existing titanium-based BMGs usually contain harmful elements such as Ni, Cu, Al or Be, in order to provide sufficient glass forming ability (GFA) for bulk components. Therefore

newly developed biocompatible alloys containing additions of Zr, Si, Ta, Pd, Nb are fabricated as thin amorphous ribbons, by mean of rapid cooling techniques, such as melt spinning. Resulting biomaterials have better electrochemical stability and excellent biocompatibility response [78], [79], [80], [81], [82], [83]. Ribbons could be furtherly processed via powder metallurgy techniques, which usually include milling to amorphous powder and consolidation by mean of hot pressing or extrusion. Parameters control during powder metallurgy processing also allows fabrication of bulk amorphous materials with controlled porosity, usually called bulk metallic glass foams (BMGFs) [20]. Fabrication of porous materials by mean of powder metallurgy could provide biomechanical compatibility, since resulting porosity reduces the Young's modulus close to rigidity of human bone. Superficial porosity also increases the interface between bone and implant offering better implant fixation. Higher porosity and pore interconnectivity stimulate cell migration and bone growth at better mechanical properties than scaffolds bioactive ceramics [84], [85], [86] [87].

1.2. Replacement of Ni as amorphization element in the new alloys

The present habilitations thesis presents some significant contributions that were made in order to eliminate the allergenic or toxic elements, as much as possible, and in the same time to create new nano/ultra-fine grained structures. Results regarding possible the effect of the replacement of Ni with Ga on the GFA and structure of the well-established $Ti_{41.5}Zr_{2.5}Hf_5Cu_{37.5}Ni_{7.5}Si_1Sn_5$ BMGs [88] [89] was the subject of some articles published in prestigious journals, with good impact over researching community [5], or presented at international conferences [6]. The copper, which is still present in the alloy composition, is regarded some time as possible cytotoxic element [77]. However, compared to nickel, it is less harmful [74] and therefore its presence up to a certain level might be tolerated. Additionally, the GFA of the starting compositions is relatively good, i.e. BMGs with diameters up to 6 mm can be produced [88] [89].

1.2.1. Biological effects of Ni and Ga

Total replacement of Ni as amorphization element is considered mandatory, since this element is known as allergenic to human body for many years [71]. Meanwhile gallium, is generally considered as non-toxic for biomedical use [38]. The allergenic effects of nickel are already well documented and beyond any doubt, especially as major cause for contact dermatitis: nickel and its salts were listed as Category A by the German Federal Institute for Risk Assessment, as result of very rigorous study elaborate between 1985 and 2001 by dermatologists from universities, representatives from the chemical industry and members of regulatory authorities [72]. Allergens belonging to Category A have “proven strong contact allergenic effect in humans”. Classification is the result of the fact that “in larger collectives 1% or more of the patients react positive and that several independent case studies and experimental data on humans are available”. Apart from proven allergenic effects, poor biocompatibility of nickel includes also relatively high corrosion in biological fluids, high cytotoxicity, haemolytic behavior in particulate form, as well suspicions over its genotoxicity, carcinogenicity, and potential mutagenicity [73]. Above all, carcinogenicity being a stochastic phenomenon, and even a single cancerous cell can ultimately lead to a fatal tumor, there are serious concerns to completely eliminate nickel as alloying element in all biomaterials.

Although the metabolic mechanism of gallium in human body is not fully understood, it is certain that incorporation of gallium inside bone tissue by mean of insertion into hydroxyapatite is protecting it from resorption and is improving the biomechanical properties of the skeleton. It has also been determined that small quantities of gallium increase calcium and phosphorus content of bone. Gallium compounds seem also to be effective in treatment of severe hypercalcemia and have direct, non-cytotoxic effects on osteoclasts [90]. Experimental researches proved that gallium could be effective in the treatment of severe disorders associated with accelerated bone loss, by reducing osteoclastic resorption without negatively affecting osteoblasts [91]. Therefore, hydroxyapatite containing gallium ions in proportion up 11% in mass has been proposed as novel material recommended for grafts and implants stimulating bone growth, by mean of enhanced osteosynthesis and calcium retention *in loco* [92].

Gallium-doped phosphate-based glasses used to produce medical devices also show antibacterial activity, inhibiting bacteria growth and formation of biofilms responsible for some serious airway infections [93]. Recent studies [94] [95] reveal that gallium-containing phosphosilicate bioglasses evidence improved ability to

functionalization for better bonding with biomolecules, such as drugs, proteins, peptides, etc. Beneficial effects of gallium have been reported also on sol-gel derived bioactive glasses. These bioceramics of third generation are characterized by excellent bioactive behavior and biocompatibility, which recommend them for applications in the fields of scaffold preparation, drug delivery, coating of stainless steel implants, tumor treatment, etc. Small amounts of gallium compounds improve formation on superficial layer of hydroxycarbonate apatite, responsible for bonding between the glass and the host bone [96].

1.2.2. Gallium effect on glass forming ability (GFA) of Ti alloys

Although replacement of nickel with gallium would be beneficial from the point of view of biocompatibility, the newly formulated nickel-free alloys should be able to produce amorphous or other nanostructured phases. As mentioned previously in this work, the experimental material is based on an already known $Ti_{41.5}Zr_{2.5}Hf_5Cu_{37.5}Ni_{7.5}Si_1$ Sn_5 BMGs [88] [89] able to be fabricated upon rapid cooling as rods with diameters up to 6 mm. In this alloy composition the nickel was replaced by gallium. Nickel has a well-established effect on increasing the GFA of Ti-based alloys fabricated by mean of rapid cooling of the melted alloy, and any replacing element must comply *ab-initio* with the most important empirical criteria for formulation of amorphous alloys. Although none of these criteria formulated by Inoue [97] shows universal applicability, they require that (1) the alloy has at least three components-large number of components seeming to improve the GFA, (2) the atomic sizes of mains components are different with more than 12% and (3) there are negative heats of mixing among the elements, which could improve homogenous mixing of different elements within initial melt. In this regard, the newly formulated alloy has a considerable number of composing elements, which complies with the first empirical rule.

Table 1.1. Chemical composition of the alloy (given in both atomic and weight percent) and the radii of the constituent atoms [99], as well as the atomic mismatch and the heat of mixing between Ga and the rest of the constituent atoms. For comparison, the heat of mixing with Ni is also given [98][1].

Element	Ti	Zr	Hf	Cu	Ga	Si	Sn
Atomic [%]	41.5	2.5	5.0	37.5	7.5	1	5
Mass [%]	29.96	3.44	13.45	35.91	7.88	0.42	8.94
Atomic radius [pm]	146.15	160.25	157.75	127.80	139.20	115.30	162.00
Atomic radii mismatch [%]	5	13	12	8	--	17	16
Heat of mixing with Ga [kJ/mol]	-23	-40	-34	+1	--	-17	+1
Heat of mixing with Ni [kJ/mol]	-35	-49	-42	+4	not for interest	-40	-4

[1] Reprinted with permission by Elsevier.

Table 1.1 summarizes the chemical composition of the alloy (given in both atomic and weight percent) and the radii of the constituent atoms [98], as well as the atomic mismatch and the heat of mixing between Ga and the rest of the constituent atoms. For comparison, the heat of mixing with Ni is given as well [99].

Gallium is supposed to replace nickel, which has an atomic radius of 124.59 pm [98]. Atomic size mismatch between gallium and other components complies with Inoue's second rule in case of zirconium (13%), hafnium (12%), silicon (17%) and tin (16%). Atomic mismatch is less than 12% relative to titanium (5%) and copper (8%), which are two of the most important components. However, the nickel element, which is providing good GFA to the Ti-Zr-Hf-Cu-Ni-Si-Sn alloy, does not fully respect this rule as well. It has good atomic mismatch relative to titanium (15%), zirconium (22%), hafnium (21%) and tin (23%). However, it has a difference of atomic radius of 7% in comparison with silicon, an only 3% with copper, which is best represented in composition, after titanium.

An evaluation of the heat of mixing for gallium with other element leads to the following conclusions: mixing with titanium, zirconium, hafnium and silicon is expected to be homogenous, since heat of mixing is strongly negative (-23 kJ/mol, -40 kJ/mol, -34 kJ/mol and -17 kJ/mol, respectively). Melt homogenization could be slightly more difficult relative to tin and copper, the latest being the most abundant after titanium, which could rise some metallurgical problems, since heat of mixing is slightly positive (about 1 kJ/mol for all three elements). However, nickel has even more difficult problem with copper, the heat of mixing being 4 kJ/mol [99] Although preliminary considerations suggests that replacement of nickel with gallium seems to be somehow less effective in terms of amorphization capacity, there is an imperative requirement for elimination of toxic and allergenic elements, which is justifying efforts for development of nickel-free BMGs.

1.2.3. Experimental evaluation of a new Ni-free alloy

As mentioned above, a new Ti-based alloy was designed expressly for the research program, based on the above mentioned alloy. The investigated samples were prepared in several steps. First, the master alloy with nominal composition $Ti_{41.5}Zr_{2.5}Hf_5Cu_{37.5}Ga_{7.5}Si_1Sn_5$ (at.%) was prepared from pure elements (purity 99.9% and better) by arc-melting under Ti-gettered Ar 99.998% atmosphere. The master alloy button was then flipped and re-melted several times in order to assure the homogeneity. The master alloy ingot was then crushed in small pieces and these were further used to produce samples upon suction casting method. In order to study the reliability and the repeatability of the casting method, several samples with different geometries were produced: rods with diameters up to 3 mm and length up to 50 mm, as well as 10 mm wide, 1.5 mm thick and 30 mm long plates.

In order to prove the homogeneity of the structure and uniform distribution of the phases, all samples were analyzed at room temperature by X-ray in transmission configuration, using the monochromatic high-energy high intensity synchrotron beam at the ID11 beamline of the ESRF Grenoble, France. The incident X-ray beam had an energy of 100 keV, which correspond to a wave length λ = 0.0123984 nm. The samples were transversally scanned at different positions all the way through their entire length. However, due to the small λ, the presence of crystalline phases cannot be resolved within acceptable accuracy due to the high number of crystalline reflections, which overlap. Therefore, selected samples were further investigated by X-ray in Bragg-Brentano configuration (FEI X'Pert PRO MPD diffractometer with a copper anode X ray tube (λ = 0.0155 nm), PixCEL detector, vertical $\theta - \theta$ goniometer and spinning

sample holder) in continuous scanning mode using a step size of 0.0130 degree and 80 seconds step time at room temperature. The patterns were further analyzed using the X'Pert HighScore Plus software linked with the ISCC PDF-4+ Database.

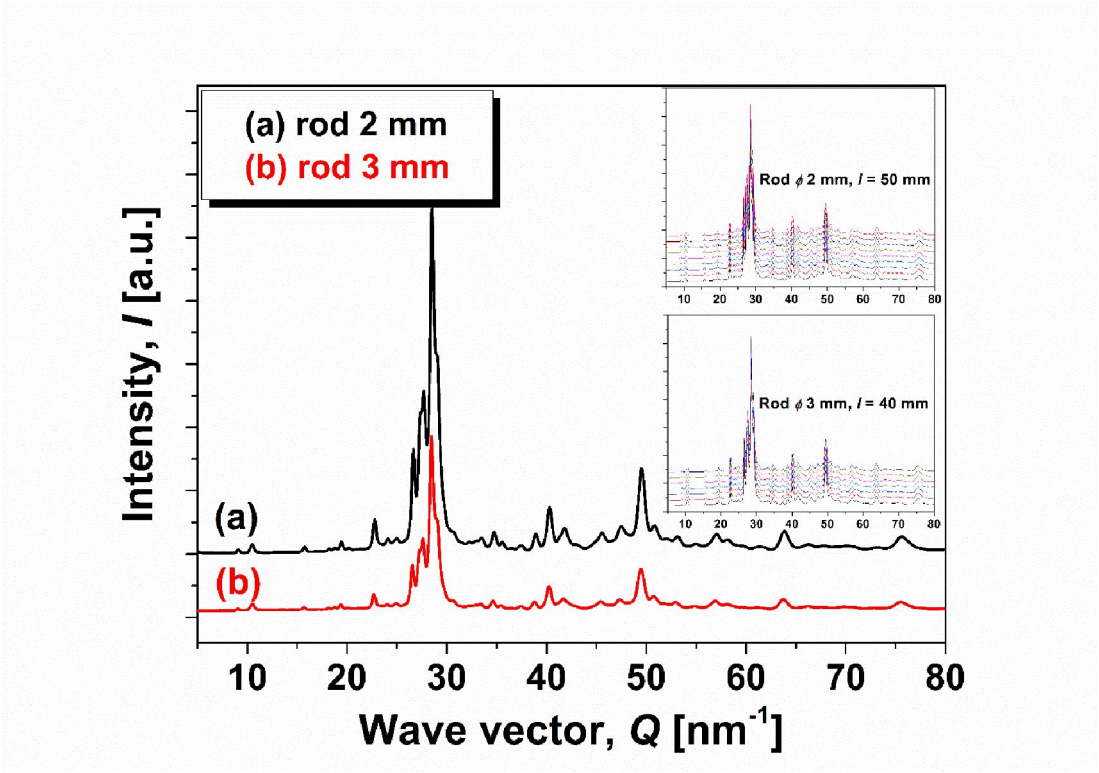

Figure 1.1. Representative X-ray diffraction patterns (measured in transmission configuration using synchrotron radiation) for $Ti_{41.5}Zr_{2.5}Hf_5Cu_{37.5}Ga_{7.5}Si_1Sn_5$ rods with 2 and 3 mm diameter. The insets show the complete scan all the way through their length [5][2] [3].

Figure 1.1 shows the representative diffraction patterns for 2 mm and 3 mm diameter rod-shaped samples. For better physical understanding, as well as to facilitate the comparisons, the diffracted intensity is plot as a function of Q wave vector ($Q = 2\pi\sin\theta/\lambda = 2\pi/d$, where θ is the diffracted angle and d the inter-planar distance). As mentioned in the experimental part, in order to prove the homogeneity, all rod and plate-shaped samples were scanned through their entire length. The insets in Figure 1.1 show for clarity all patterns characteristic to the 2 and 3 mm diameter rod samples, measured at different positions. As one can clearly see, there are no visible differences between samples. Moreover- and this can be seen better in the insets- there the broadening of the patterns at Q values around $Q_1 \approx 28$ nm^{-1} and $Q_2 \approx 48$ nm^{-1} is observed, which is characteristic to amorphous/nanocrystalline structures. Furthermore, the ratio $Q_2/Q_1 \approx 1.71$, in very good agreement with the value predicted for a perfect icosahedron (i.e. 1.7) [100] [101], therefore confirming the amorphous nature of the matrix.

Altogether, these results indicate that the samples are homogeneous and may have an identical structure consisting of crystalline phases embedded in an amorphous matrix. Due to these results, for the further analyses only the rods with 3 mm diameter

[2] We are grateful to Dr. M. Stoica co-authors of [5] for the synchrotron investigations performed in the frame of the experiment HD 613 at ESRF Grenoble.
[3] Reprinted with permission by Elsevier.

were considered. The selection was done on the basis that the 3 mm diameter rod may be used for manufacturing screws or pin samples for medical use. However, these aspects, as well as the mechanical properties of selected samples, are not within the purpose of the research program.

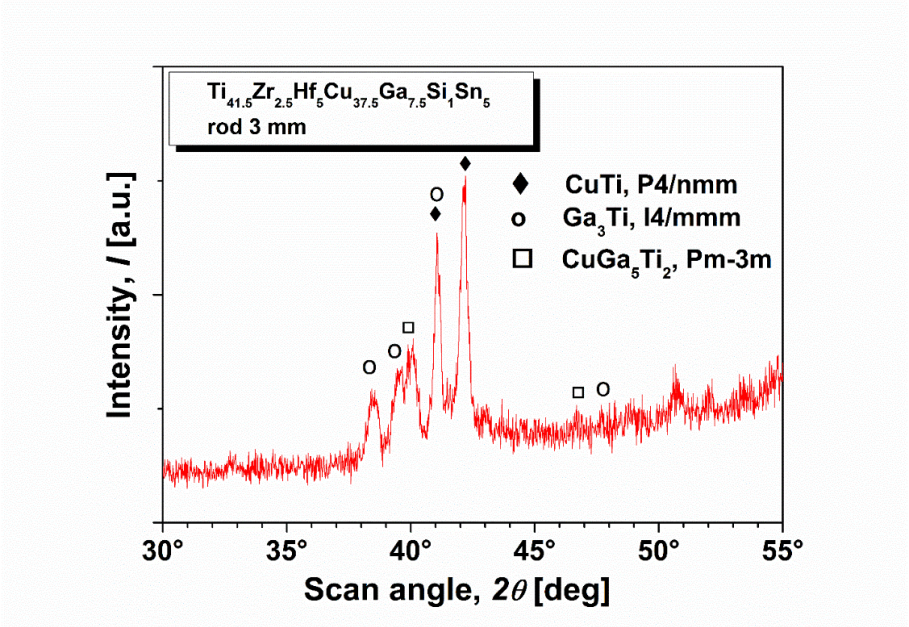

Figure 1.2. XRD patterns of the $Ti_{41.5}Zr_{2.5}Hf_5Cu_{37.5}Ga_{7.5}Si_1Sn_5$ bulk samples with 3 mm diameter, Cu K-α radiation (λ = 0.0155 nm) [5][4] [5].

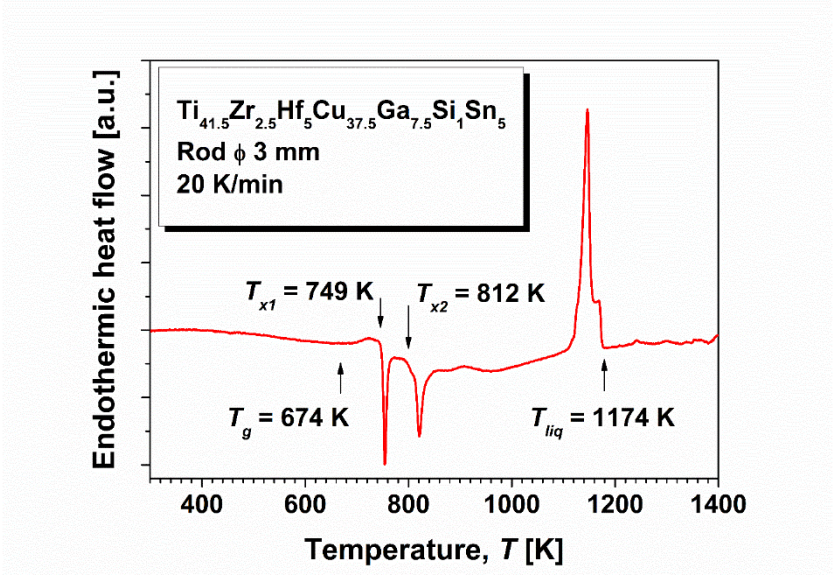

Figure 1.3. DSC thermograms for the $Ti_{41.5}Zr_{2.5}Hf_5Cu_{37.5}Ga_{7.5}Si_1Sn_5$ rods with 3 mm diameter. The onset of the main events are indicated by arrows and marked accordingly [5][5].

Due to extremely abundant details collected upon XRD in transmission using hard X-ray produced by synchrotrons, the overlap of several diffraction peaks can

[4] Special thanks for contributions in interpretation of XRD patterns to M. Stoica co-author of [6] [8] [9] [10] [13] and D. Ursu co-author of [13].
[5] Reprinted with permission by Elsevier.

make the identification of the crystalline phases rather difficult. This is why few samples were checked also in Bragg-Brentano configuration using Cu radiation.

Figure 1.2 shows the patterns collected for the $Ti_{41.5}Zr_{2.5}Hf_5Cu_{37.5}Ga_{7.5}Si_1Sn_5$ alloy sample with 3 mm diameter. For clarity, the plot was limited between 2θ=30° and 2θ = 55°. The diffraction profile seems to be somehow diffused suggesting a certain amorphous component. However, there are also strong evidences of the presence in considerable proportion of some crystalline phases, which were identified as tetragonal γ-CuTi, Ga_3Ti and possibly $CuGa_5Ti_2$. However, there are also some peaks which could not be assigned and, most probably because of the complexity of the current alloy, they come from distorted or complex phases.

Table 1.2. Summary of thermal stability data, comparison between the actual alloy Ni-free and the starting alloy, Ga-free [88][6].

Alloy	T_g [K]	T_x [K]	ΔT_x [K]	T_{liq} [K]	T_{rg}
Ga 7.5% (this work)	674	749	75	1174	0.57
Ni 7.5% (from [88])	693.33	757.52	64.19	1176.07	0.590

In order to check the thermal stability of the cast samples, as well as to prove their nature as composite samples, small slices of the cast samples were heated up to a temperature of 1400 K under Ar flow in a Netzsch differential scanning calorimeter (DSC). The heating rate was set at 20 K/min. The glass transition temperature T_g, the crystallization temperatures T_x and the liquidus temperature T_{liq} were measured as the onsets of their corresponding events in the DSC curves.

The thermograms are presented in details in Figure 1.3. As suggested by the XRD results, there it is an amorphous matrix, which has a clear glass transition point with the onset at T_g = 674 K (401°C). The glass-transition event is followed by a distinct supercooled liquid region (SLR) and two separate exothermic reactions, with the onset at T_{x1} = 749 K (475°C) and T_{x2} = 812 K (539°C), respectively. The liquidus point of this alloy is T_{liq} = 1174 K (901°C), which is relatively low for a titanium-based alloy and thus may facilitate industrial fabrication via rapid cooling from the melt. Therefore, it is proved that the samples are composites, with crystalline phases embedded in an amorphous matrix, which shows an extension of the SLR ΔT_x of 75 K and reduced glass transition temperature $T_{rg} = T_g / T_{liq}$ of 0.57.

All together, these values indicate a good GFA of the matrix, with a high thermal stability against crystallization [48]. However, its actual composition is not known, but the characteristic temperatures are extremely close to those measured for the Ni-containing alloy, which was the starting point of this research [88]. All these temperatures and parameters are summarized in Table 1.2.

Interesting is to observe that in the case of Ga-containing alloy, the remained amorphous matrix seems to have a more extended SLR (i.e. 75 K instead of 64.19 K) and a comparable reduced glass-transition temperature. Moreover, both alloys melt almost at the same temperature (1174 K for Ga-containing alloy, 1176.07 K for Ni-containing alloy) and this proves that there are no essential differences in the melt

[6] Reprinted with permission by Elsevier.

behavior. Also, the Ga-containing alloy shows in DSC two very clear, well-separated crystallization events (see Figure 1.3), as well as in the case of Ni-containing BMG sample, where one can remark a second crystallization event with the onset at approximately 820 K [88].

Therefore, one can conclude that the replacement of nickel by gallium does not essentially affect the master alloy and it may become fully amorphous if it is cast as sample with reduced dimensions.

This assertion is confirmed by the optical microscopy investigations, which were performed on an Olympus BX 51M or an Olympus LEXT metallographic microscope. Figure 1.5.a shows the transition area of the upper part of the 2 mm rod, containing a transition area from fully amorphous to fully crystalline structure.

Selected samples cut from rods were metallographically processed, etched and examined by mean of scanning electron microscopy (SEM) using a FEI Quanta 250 FEG scanning electronic microscope equipped with an EDAX SDD Apollo X sensor, in order to evaluate the microstructures, as well as distributions of the most important metallic atoms. The pictures were taken in back-scattered (BSE) mode, as well as secondary electron (SE) mode.

Figure 1.4 shows the SEM appearance of the cross-sectional slice cut from a $Ti_{41.5}Zr_{2.5}Hf_5Cu_{37.5}Ga_{7.5}Si_1Sn_5$ rod with 3 mm diameter. As can be observed at a first glance, the sample is homogenous and shows a fine distribution of dendritic structure. However, in the left picture (SE mode, topological contrast), which was made at a lower magnification, one can see that the sample preserves a margin which does not show at this scale any feature.

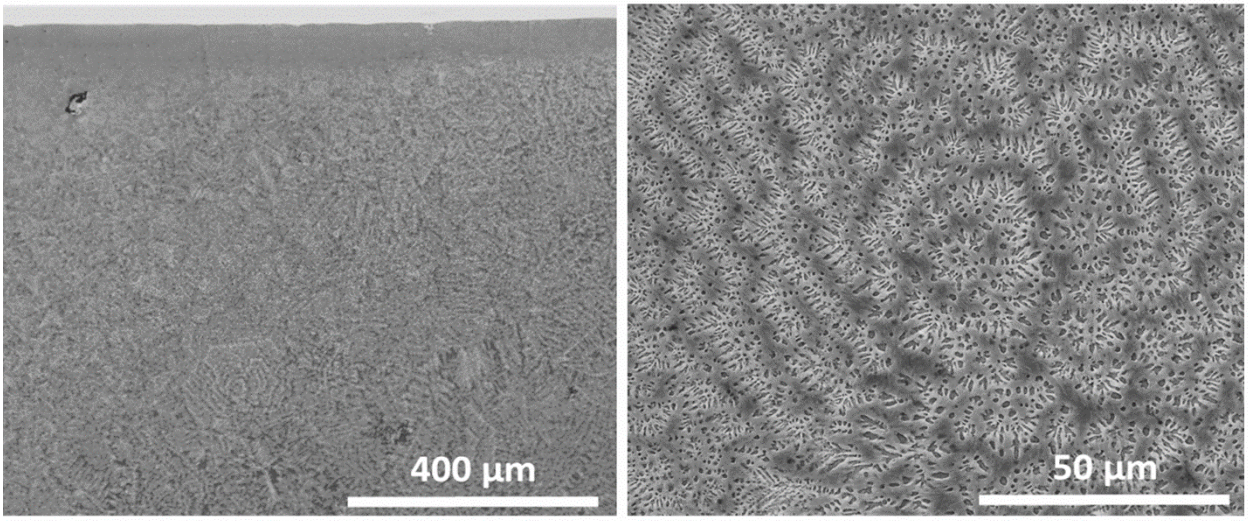

Figure 1.4. SEM micrographs taken from a slice cut perpendicularly to the axis of a $Ti_{41.5}Zr_{2.5}Hf_5Cu_{37.5}Ga_{7.5}Si_1Sn_5$ cylinder with 3 mm diameter. Left pictures: SE mode, low magnification. Right picture: BSE mode, higher magnification [5][7] [8].

The SEM magnifications are (in general and here in particular) not high enough to confirm with acceptable confidence the amorphous nature of that layer. However, taking in account that the margins were in direct contact with the copper mold during

[7] Special mention for A. Raduta and C. Locovei, co-authors of [5], for significant contribution in accomplishment and interpretation of SEM investigations

[8] Reprinted with permission by Elsevier.

casting (i.e. there is the highest cooling rate), as well as the XRD and DSC results, we can expect to have around an amorphous cover. Moreover, because the temperature gradient decreases from the margins to the center, there also a structure gradient extending over no more than 500 μm can be observed. In the center of the sample (right picture in Figure 1.4, BSE mode, contrast upon composition) it is presented the middle of that slice.

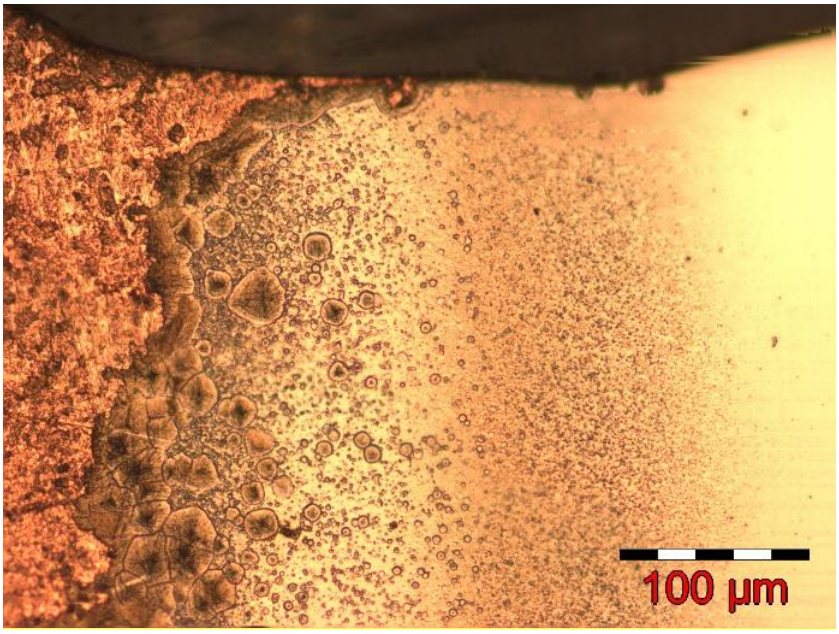

a. Transition area of a 2 mm diameter rod in Ti-Zr-Hf-Cu-Ni-Si -Sn alloy displaying a complex structure from fully amorphous to fully crystalline structure.

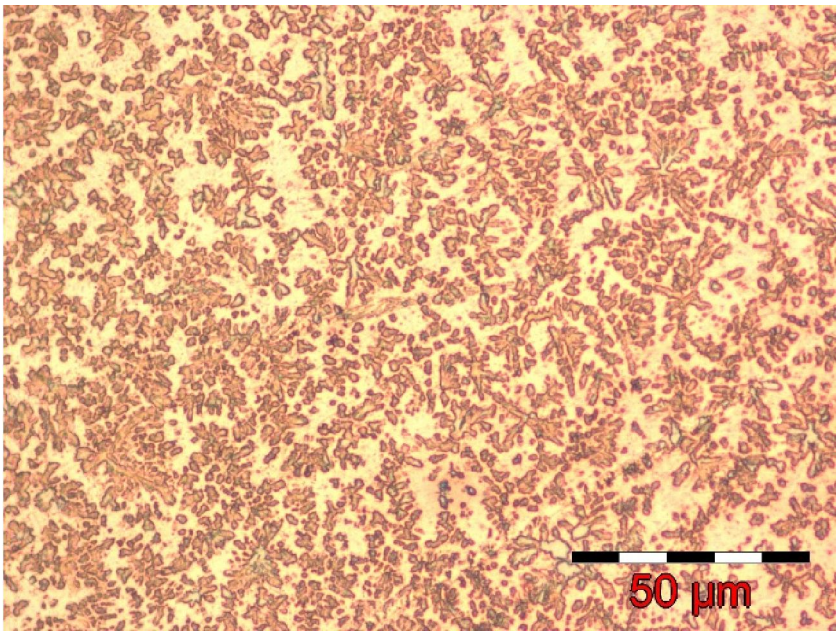

b. Casting crystalline structure in an amorphous matrix, in a 2mm rod in Ti-Zr-Hf-Cu-Ga-Si-Sn alloy, central region.

Figure 1.5. Typical OM aspect of Ti-Zr ultra-rapidly solidified alloys [5][9] [10].

[9] Special thanks for A. Raduta, co-author of [2] [3] [5] [14] [16], and L. Soveja, research engineer at the Politehnica University Timisoara, for contributing to the optical investigations presented by this thesis.
[10] Reprinted with permission by Elsevier.

There are basically three types of features. First of all are to be observed the dendrite marks- because the dendrites were etched-out during the metallographic sample preparation. Then, around the dendrite arms (i.e. the interdendritic space), there it seems to be a white area, from which the dendrites emerged. These white areas are separated by dark areas, which appear to have an acicular morphology. Due to the differences in contrast in this BSE image, it is possible to conclude that the whiter area may contain elements with higher number of electrons, while the dark spikes are rich in elements with lower Z number. Investigations based on light microscopy are consonant to previous observation (Figure 1.5), regarding the dendritic appearance of some crystalline phases, as well as the transition from amorphous to crystalline within the 3 mm rod sample.

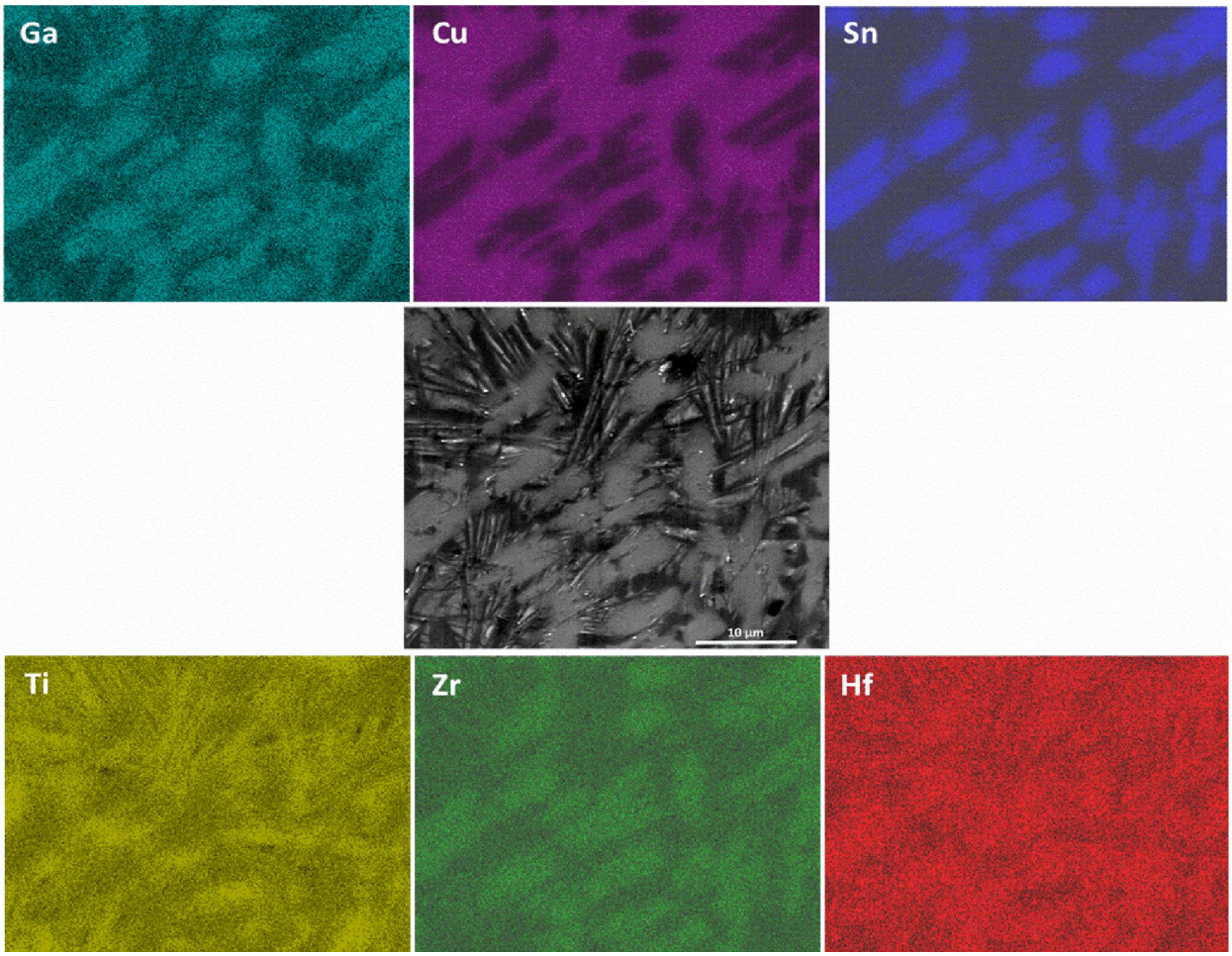

Figure 1.6. Energy-dispersive X-ray mapping displaying the distribution of the elements in the studied cross-section, slice cut from a $Ti_{41.5}Zr_{2.5}Hf_5Cu_{37.5}Ga_{7.5}Si_1Sn_5$ cylinder with 3 mm diameter. The central pictures shows the investigated area (SEM image, SE mode) [5][11] [12].

In order to confirm these findings, the elemental mapping was performed. Figure 1.6 shows the distribution of the elements (as marked in each picture), which may be present in the sample. The mapping was accomplished on the area shown in the

[11] Element mapping investigations were achieved with the contribution of C. Locovei, co-author of [5].
[12] Reprinted with permission by Elsevier.

central SEM picture (SE detector). There one can observe the acicular dark areas, the white areas (in fact light-gray in this actual picture) and the empty spaces in between, which are left by the missing dendrites. The element mapping shows that these light-gray areas certainly contain Ga, Sn and Zr. These islands contain Hf as well, but this element seems to be more uniform distributed, i.e. it appears also between the islands. This confirms the hypothesis that these areas contain heavier elements. Ga is almost exclusively distributed in the brighter areas, but some light traces are also visible within the phases with acicular morphology. Then, the acicular structures are TiCu (maybe with some Hf). The outcomes are in agreement with the phases identified upon XRD (see Figure 1.2). CuGaTi compounds are hidden within the γ-TiCu and thus the missing dendrites are GaTi- which is very likely because Ga is a soft metal and therefore may be easy worn-out or chemically dissolved upon metallographic preparation.

Larger magnification were obtained by mean of high-resolution transmission electron microscopy (HR-TEM) investigations, using a FEI Tecnai G2 200 kV S/TEM microscope. All the investigations were carried out at 200 kV accelerating voltage. These small scale microstructural investigations are based in consideration of the preliminary investigations by mean of DSC, XRD, synchrotron diffraction and SEM, which evidenced that the newly designed alloy is multi-phased and seems to contain both amorphous and crystalline components.

TEM lamella preparation [7] was conducted using a dual beam FIB microscope FEI Quanta 3D. In order to protect the lamella from the beam damage, a 1 x 2 x 20 µm (T x W x L) Pt layer has been deposited exactly over the area of extraction of the sample (Figure 1.7.a). After Pt deposition two 20 x 15 x 12 µm (L x W x D) trenches were dug using Ga ions focused beam (Figure 1.7.b). For crystalline metallic materials the “J cut” is performed 1 µm away from the trenches walls (Figure 1.7.c). For amorphous materials and especially for Ga containing amorphous materials the “J cut” of the lamella should be done 2…3 µm away from the walls and at least 2.5 µm wide (Figure 1.7.d). The microprobe manipulator is handled carefully as close as possible (maximum 150 nm away from the lamella). A new layer of 1 x 4 x 3 µm (T x W x L) of Pt is deposited on the lamella-manipulator interface (Figure 1.7.e). This layer acts as a welding spot between lamella and manipulator needle.

Once the welding is secured, the lamella is cut free (Figure 1.7.f) and then carefully attached to the half-moon 3 mm diameter TEM holder using Pt deposition. Then the lamella is cut free from the needle (Figure 1.7.g). Now, the lamella is ready for the final milling that ensures a thickness of 100 to 150 nm, which, in turn, ensures electron transparency (Figure 1.7.h).

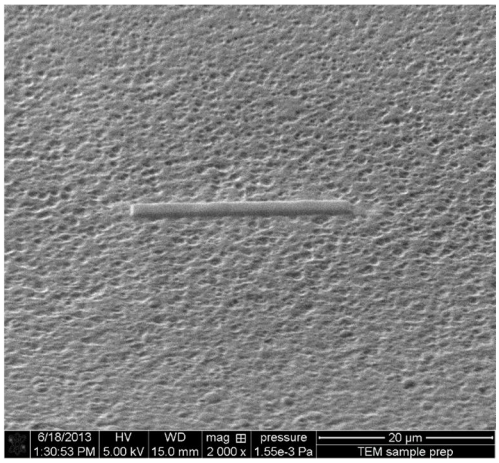

a. Protective Pt layer deposition

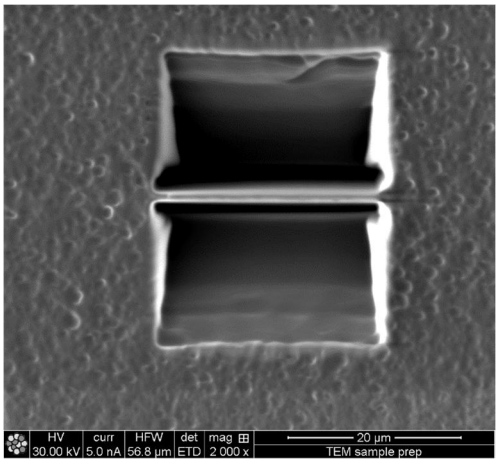

b. Front and back trench of lamella

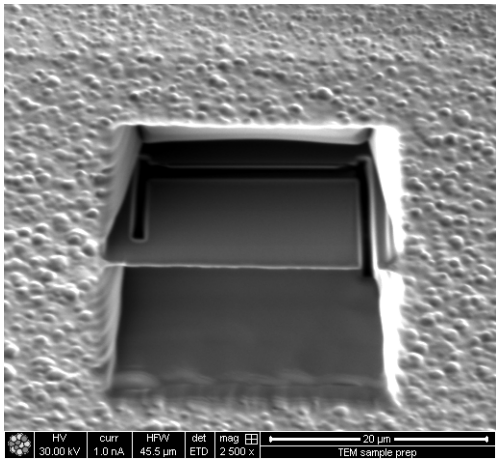

c. Standard “J cut”

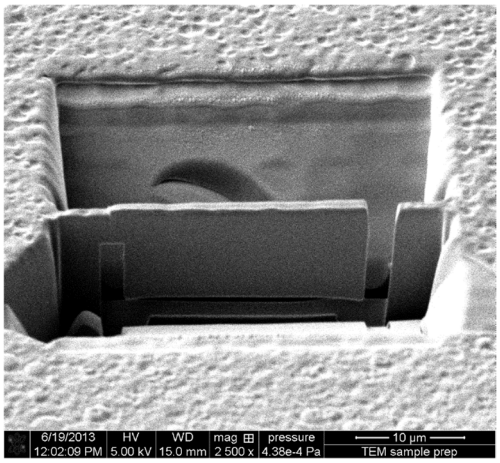

d. “J cut” on amorphous metallic material

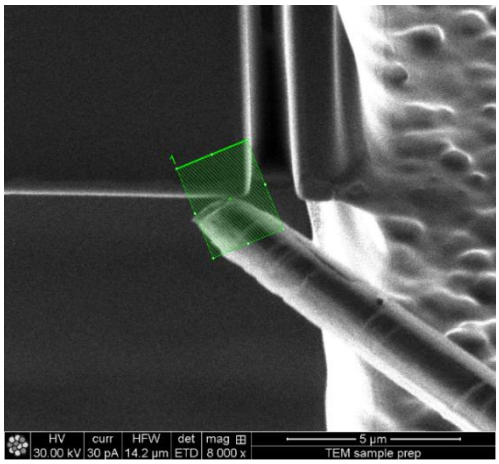

e. Needle to lamella Pt welding

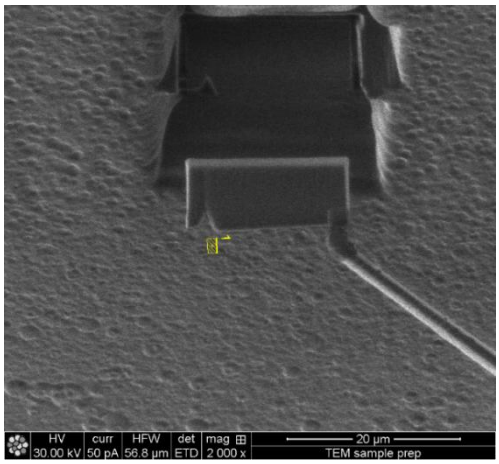

f. TEM lamella extraction

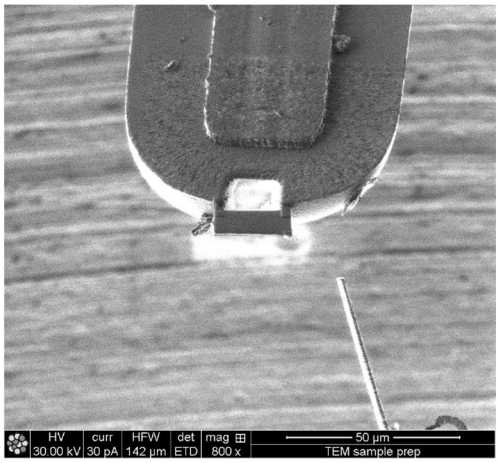

g. Attached to half-moon TEM holder

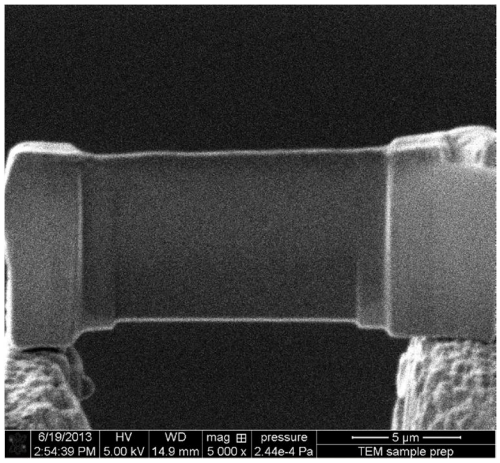

h. Final milling of lamella

Figure 1.7. FIB TEM lamella preparation [7][13] [14]

[13] HR-TEM investigations illustrated in this thesis were accomplished with the contribution of C. Locovei, co-author of [7] [8] [9] [10] [13], and interpreted with the help of M. Stoica and A. Raduta, to whom the author is grateful.

[14] Reprinted with permission by Trans Tech Publications Inc.

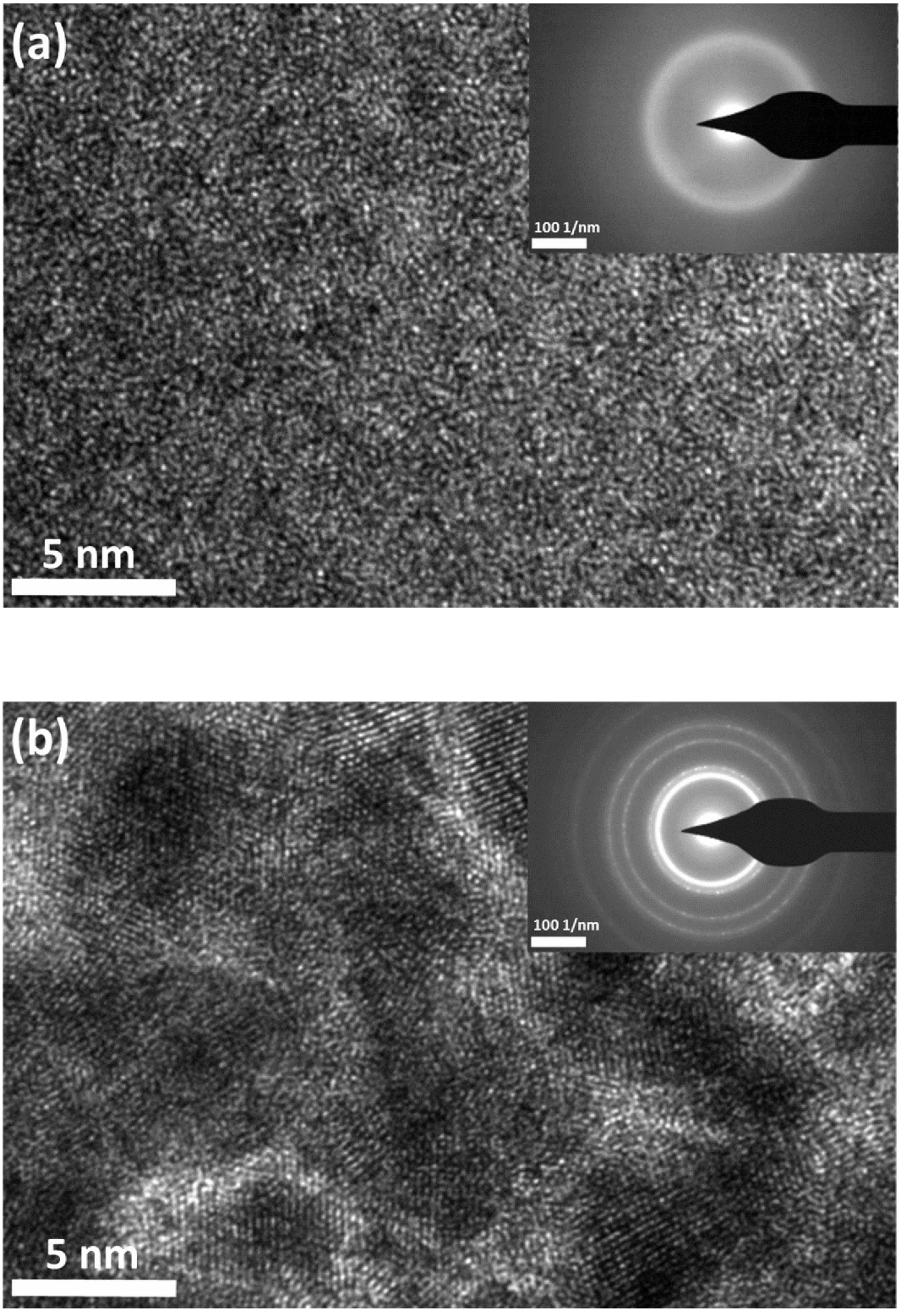

Figure 1.8. HR-TEM images taken from the light-gray zone in Figure 5: (a) amorphous structure of the alloy matrix characterized by disordered disposition of atoms and (b) mixture of nanocrystals and amorphous zones in the same investigated area. The insets show the corresponding SAED patterns [5] [15].

[15] Reprinted with permission by Elsevier.

The HR-TEM investigation areas were mostly located in matrix, because the crystalline features are too big for such small-scaled microscopy. However, as anticipated by previous investigations (DSC, XRD and SEM) the structural phases evidenced on rapidly cooled alloy samples show considerably complexity, and therefore a very precise phase analyze on micro-grains cannot be performed. In order to complete the analyses, the high-angle annular dark-field imaging (HAADF) on scanning transmission electron microscope (STEM) was employed. The annular dark field image is formed only by the very high angle, incoherently scattered electrons (as opposed to Bragg scattered electrons), hence it is highly sensitive to variations in the atomic number of atoms in the sample.

Figures 1.8 (a) and (b) show the HR-TEM images taken from a specific island, which was identified in Figure 1.5 as a light-gray zone. Figure 1.8 (a) proves that the mentioned areas are or contain amorphous phase. Additionally, the corresponding selected area electron diffraction pattern (SAED) is presented in the inset. There only diffuse rings can be observed, confirming the amorphous nature of the investigated zone. However, some fine crystals may be observed in the very close neighborhood (i.e. still in the same island as discussed previously), as shown in Figure 1.8 (b). The nanocrystals are no larger than 10 nm and they appear with dark contrast in the micrographs. The corresponding SAED patterns are presented in the inset. Despite few clear crystalline rings, the broad haloes corresponding to the amorphous matrix are also present.

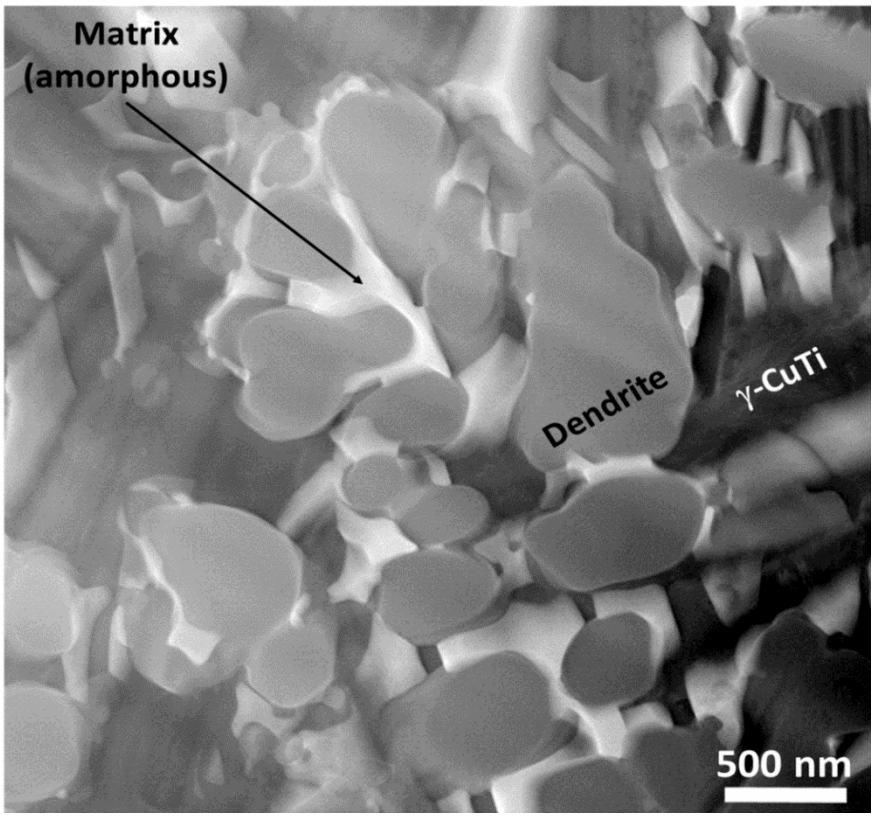

Figure 1.9. STEM-HAADF micrographs, sample cut by FIB from a $Ti_{41.5}Zr_{2.5}Hf_5Cu_{37.5}Ga_{7.5}Si_1Sn_5$ bulk samples with 3 mm diameter showing a very clear contrast upon composition [5][16].

[16] Reprinted with permission by Elsevier.

Figure 1.9 shows the HAADF micrographs, which evidence a very clear contrast upon composition. The results are in perfect agreement with previous findings. There one can distinguish between the light γ-CuTi crystals, the dendrites and the residues of the amorphous matrix. As supposed upon SEM investigation (Figure 1.5), corroborated with XRD results (see Figure 1.2), the dendrites are probably Ga-Ti compounds, while the matrix contains the rest of Ga, Sn, Zr, Hf.

In conclusion, the replacement of replacement of Ni with Ga is expected to give significant advantages in terms of biocompatibility, since the harmful effects of Ni are removed, while Ga seems to bring benefits for bone recovery. The GFA ability of the alloy is somehow reduced, since the 2 and 3 mm rods are not completely amorphous anymore, but the master alloy may become fully amorphous if it is cast as sample with reduced dimensions. The γ-CuTi crystals, the dendrites and the residues of the amorphous matrix are marked in the picture.

However, based on analogy with other alloys, the resulting composite structure consisting of amorphous matrix and several crystalline phases may be even more favorable in terms of mechanical properties, especially ductility. Therefore future researches should be focused on the evaluation of mechanical properties and biocompatibility.

1.3. Replacement of Cu as amorphization element

The main objective of these researches [8] is the development of new titanium-based amorphous alloys or amorphous/crystalline composites completely free of copper.

The replacement of coper is made with silver, which could be considered more biocompatible. Regarding the biosafety, it is known since long time that silver has an antimicrobial effect [102]. The biological effect of both copper and silver and the differences between them, showing that it is safer to use silver instead of copper, have been documented based on an exhaustive literature review.

1.3.1. Biological effect of copper and silver

Biocompatibility evaluation of different materials, which are in contact with human body for long periods, is a very complex issue [35]. Allergenic, cytotoxic and inflammatory effects are some of the most important properties that are usually investigated for assessment of metallic alloys for biomedical use [33], [34]. Unlike nickel, cobalt or chrome, neither copper nor silver have been reported so far for significant allergenic potency [103]. Therefore, studies are focused on the cyto-compatibility and possible inflammatory reactions. Materials cytotoxicity is most commonly estimated *in-vitro* by relative viability, proliferation and morphological changes of different cell lines in contact with metallic alloys for some periods of time, while the test of inflammatory reactions consisted of quantifying the multinucleated giant cells (MGC) appearing in monolayer cell cultures. These results could be aggregated with measurements of the rates on which ions of alloying elements are released from biomaterials, since metallic ions released by biomedical implants represent the main cause of unwanted secondary reaction in organism. Resulting cytotoxicology index (CI) allows scoring of metallic alloys between CI=0, when the tested alloy is highly cytocompatible, and CI =100 for highly cytotoxic or even lethal materials or substances. Although effects of pure copper and silver may be comparable in terms of *in-vitro* viability of cell cultures, the ranking by the CI reveals the most unfavorable effect of copper-containing alloys, while the presence of silver as alloying element is not an unfavorable factor, mostly because silver ion release rate seems to be very low. For example a palladium-based alloy containing 28 mass percent of silver has a CI of only 18, while a palladium alloy with 20 mass percent of copper has CI= 43 [104]. Cytotoxicity ranking of casting alloys evaluated by cell culture tests revealed that Au, Pd and Ti were the least cytotoxic (rank 1), followed by Ag (rank 2), then Ni (ranked 4) and finally Cu (rank 5), which is the most cytotoxic [105]. *In-vitro* experiments of long-term and low-dose exposure to metallic ions determined that Ag^{+} and Hg^{2+} did not produce any deterioration of cell cultures even after 4 weeks, while increase of cell death for Cu^{2+} and Ni^{2+} was significant [106].

Major concerns about biosafety of silver lead recently to more detailed studies, which concluded that silver neither had cytotoxicity nor resulted in inflammatory expression if effective concentration of released ions into the organism is maintained within certain limits, specific for each type of organism. [107]. Only few relatively alarming results have been reported so far, exclusively on dental alloys with high silver content, indicating that silver may have in the worst conditions only intermediate cytotoxic effect, while copper is considered highly toxic element, belonging to the same category as zinc and nickel [75]. A more general classification by tissues reaction around metallic implants considers reaction to silver of “capsule” type, triggering only moderate reactions from organism, in same category as metals like aluminum, iron,

molybdenum and gold, but also consecrated biomaterials such as stainless steels or Co-Cr alloys [108]. Meanwhile copper belongs to the “toxic” group together with vanadium, nickel and cobalt. Members of highly biocompatible “vital” response category are platinum, tantalum, niobium, titanium and zirconium [76]. Most worrying, some reports evidence genotoxicity of copper, which could be responsible for DNA damages, via some oxidative mechanisms, similar as cadmium, chromium, mercury, nickel, vanadium and lead [109].

The most recent reference works on metallic implant biomaterials consider that although health effects of silver are still disputed, metallic silver is non-toxic, while only some silver salts are. Meanwhile, apart cytotoxic effect, excessive copper amounts have been linked to neurodegenerative diseases (Alzheimer, Menkes, Wilson) [34].

On the same time, germicidal and antimicrobial effects of silver ions are frequently emphasized. It has been documented that silver not only reduces bacterial adhesion, but also inhibits bacterial growth, having pregnant bacteriostatic effect on highly dangerous bacteria such as *Bacillus subtilis*, *Escherichia (E.) coli* etc. [107], [110]. Anti-biofilm activity was reported against *Pseudomonas aeruginosa* and *Staphylococcus epidermidis* [111]. Silver ions were determined to be non-toxic, safe antibacterial for human body, within certain limits. They also possess anti-fungal activity, anti-inflammatory effect, anti-viral and anti-angiogenic activity. It may be added that almost all researches stresses out that safely applied therapies imply control on released concentrations of silver ions [111].

It may be concluded that, considering necessary precaution about resulting concentration of released ions, silver has already won considerable attentions for applications in cosmetics, ophthalmology alloying element for fabrication of anti-microbial surgical tools, additive for synthetic elastomers in medicine, even coatings on titanium implants [112]. Therefore it may be considered that using silver as amorphization element for fabrications of titanium-based BMGs may be reasonable from the point of view of health safety, with respect of some precautions and as result of specific investigations regarding *in-vivo* biocompatibility for certain applications.

1.3.2. Design of new alloy composition

Composition of new biocompatible alloys is determined using the molecular orbital method for the b.c.c. Ti, based on two alloying parameters, bond order (*Bo*) and the metal d-orbital energy level (*Md*), which are determined theoretically. Parameter *Bo* measures the covalent bond strength between Ti and an alloying element, while *Md* correlates the electronegativity and the metallic radius of elements.

The values $\overline{Bo}$ and $\overline{Md}$ for the alloys are determined as atomic compositional averages of the parameters for each pure metal used as alloying element, calculated by Morinaga [113]:

$$\overline{B_o} = \sum_{i=1}^{n} x_i (B_o)_i \qquad (1.1)$$

$$\overline{M_d} = \sum_{i=1}^{n} x_i (M_d)_i \qquad (1.2)$$

Coordinates $\overline{Bo}$ and $\overline{Md}$ are locating each alloy inside a distribution chart area corresponding to an estimated structural state: amorphous, glassy, BMG, crystalline etc. [114]. The chart portion belonging to the area of bulk amorphous glasses is shown

in Figure 1.10 and the list of $\overline{Bo}$ and $\overline{Md}$ for some alloying elements are given in Table 1.3.

Table 1.3. *Bo* and *Md* values for alloying elements in b.c.c. Ti [113].

Element	***Bo***	***Md*** **(eV)**
Ti	2.790	2.447
Zr	3.086	2.934
Pd	2.208	0.387
Cu	2.114	0.567
Ag	2.094	0.196
Sn	2.283	2.100
Nb	3.099	2.424

Table 1.4. Compositions and orbital method parameters of considered alloys [8].[17]

Alloy	*Ti (% at.)*	*Zr (% at.)*	*Pd (% at.)*	*Cu (% at.)*	*Ag (% at.)*	*Sn (%at.)*	*Bo*	*Md (eV)*
$Ti_{45}Zr_{10}Pd_{10}Cu_{31}Sn_4$	45	10	10	31	–	4	2.532	1.689
$Ti_{42}Zr_{10}Pd_{14}Ag_{26}Sn_8$	42	10	14	–	26	8	2.517	1.589

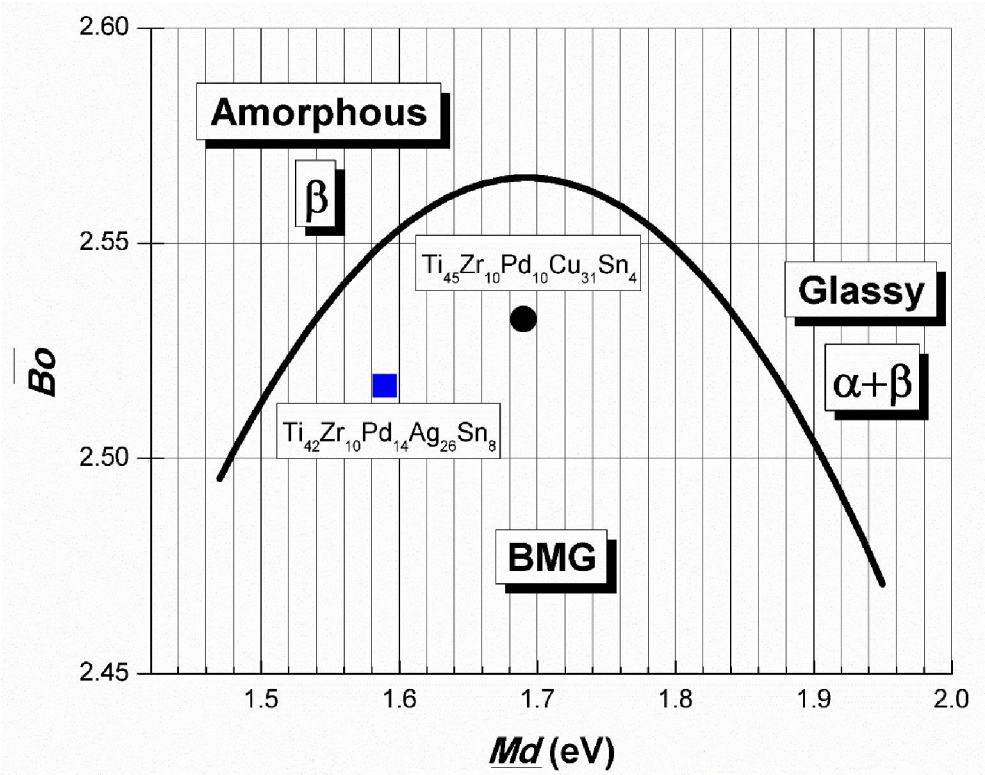

Figure 1.10. Positions of $Ti_{45}Zr_{10}Pd_{10}Cu_{31}Sn_4$ and $Ti_{42}Zr_{10}Pd_{14}Ag_{26}Sn_8$ alloys on the distribution chart of amorphous and glassy alloys, based on *Bo* and *Md* parameters [8][17] (after [114])

[17] Open access, editor MDPI AG Basel, Switzerland, financed by Politehnica University Timișoara.

The reference alloy for development of new copper-free compositions is the BMG with atomic composition $Ti_{45}Zr_{10}Pd_{10}Cu_{31}Sn_4$, having critical diameter of 4 mm and compression strength of 1970 MPa [68]. The parameters determined by molecular orbital method are $\overline{Bo}$ = 2.532 and $\overline{Md}$ = 1.689, which situate the alloy inside the BMG area (see the position of the round dot in Figure 1.10), confirming the d-electron alloy design theory. Replacement of copper with silver requires that resulting alloy remain inside the BMG area, therefore final composition was optimized to produce appropriate values of $\overline{Bo}$ and $\overline{Md}$. Optimization result is presented in Table 1.4, while in Figure 1.10 the square symbol corresponding to the new $Ti_{42}Zr_{10}Pd_{14}Ag_{26}Sn_8$ alloy is positioned inside the amorphous bell.

1.3.3. Thermodynamic considerations on the master alloy

Figure 1.11 shows schematically the enthalpy of mixing ΔH^{mix} for each atomic pair of all alloy constituents, emphasizing the values characteristic to Cu-containing pairs (Figure 1.11 (a)) and Ag-containing pairs (Figure 1.11 (b)). The values were taken from reference [99], i.e. calculated using Miedema's model for the corresponding binary liquids.

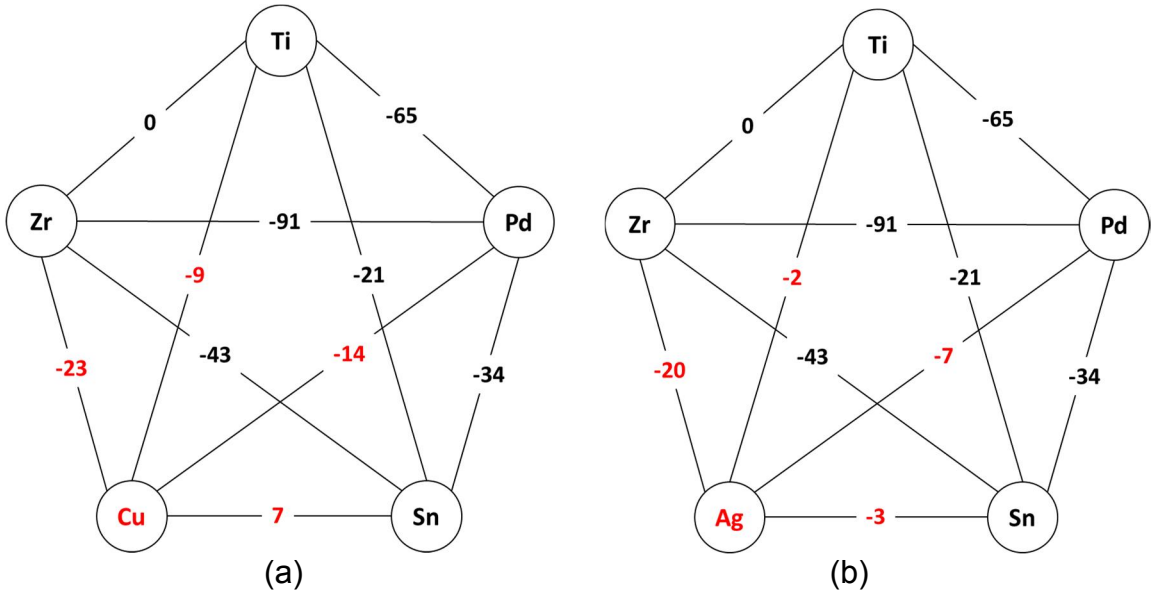

Figure 1.11. Mixing enthalpies ΔH^{mix} between the atomic pairs of the alloy constituents (in kJ/mol), emphasizing (a) Cu-containing alloy and (b) Ag-containing alloy [8][18] [19].

As it can be observed, the mixing enthalpies are in general negative, with two exception: Ti-Zr, which is zero and Cu-Sn, which is + 7 kJ/mol. The negative mixing enthalpies may indicate the possibility to form an alloy with a higher degree of dense randomly packed atomic configurations and multiple interatomic interactions in the liquid state, therefore being prone to amorphization. In fact, the starting Cu-containing composition $Ti_{45}Zr_{10}Pd_{10}Cu_{31}Sn_4$, respects the three empirical rules as formulated by Inoue [47] and hence showing a good GFA. According to them, the replacement of Cu by Ag should be beneficial for glass-formation, because Ag has only negative heats of

[18] Thermodynamic consideration were made with the consistent help of M. Stoica, co-author of [8].
[19] Open access, editor MDPI AG Basel, Switzerland, financed by Politehnica University Timișoara.

mixing with all elements. Experimentally observed, the new $Ti_{42}Zr_{10}Pd_{14}Ag_{26}Sn_8$ master alloy is off eutectic and shows a large temperature interval over which liquid and solid coexists. The reasons is analyzed later. Therefore the casting was performed with the alloy in the homogeneous liquid state, as it is described furtherly. Even so, the resulted rods exhibit a clear phase separation. As it will be shown, one of the separated phases contains Ag up to 80 at%. Thus, it is interesting to study in details the phase diagrams of binary alloys with Ag. Nevertheless, the analysis of only binary atomic pairs and binary alloys may not reflect accurately the situation in the quinary alloy, but in the absence of more elaborate models it may give at least some qualitative explanations of the observed behavior.

Ag is miscible with Pd over the entire compositional interval, in both liquid and solid state [115]. Therefore, the mixing with Pd should not put any problem. With Sn, Ag is miscible in the liquid state [115]. In the solid state, Sn is soluble in Ag over several at. %. It forms also intermetallics like $Ag_{0.8}Sn_{0.2}$ and Ag_3Sn. For more Sn the binary alloy decomposes and at ~96.5% Sn there it is an eutectic. The solubility of Ag in Sn below its melting temperature is almost zero. However, the total Sn content in the alloy is 8 at%, therefore only the Ag-rich part of the phase diagram might be for interest- and in this interval Sn may completely dissolve in Ag.

More problematic are the binary Ag-Zr and Ag-Ti alloys [115]. In both cases, the elements are miscible in the liquid state. In the solid state, Ag stabilizes the high-temperature phases of Ti and Zr. At room temperature, the solubility of Ag in Ti or in Zr, as well as Ti or Zr in Ag, is almost inexistent. Both Ag-Ti and Ag-Zr are not miscible in solid state over the entire compositional interval. However, there are few intermetallics, like AgTi and $AgTi_2$ or AgZr and $AgZr_2$. The AgTi compound is stable for a compositional interval of 50 ± 2%. As a detail, the Cu-Ti and Cu-Zr phase diagrams are characterized by the formation of far more intermetallic compounds- so in terms of competing crystalline phases and following the Inoue's findings [47] it seems that the Cu-containing alloy may have a better GFA. Moreover, silver has a higher radius as compared with copper, i.e. 0.144 nm as opposed to 0.128 nm, which makes the atomic radius mismatch between silver and titanium smaller, titanium having its metallic radius of 0.147 nm.

Ti and Zr are completely miscible as well, in both liquid and solid state [115]. There is a large temperature interval (compositional dependent, with the minimum low temperature 600 °C and minimum high temperature 1554°C), in which the ZrTi solid solution is of the type bcc β-Ti and below of the type hcp α-Ti.

Pd and Ti form solid solution from room temperature up to the melting point (i.e. up to at least 1400 °C, function of composition) in the Pd-rich side (Ti up to 20 at%), while above 50 at.% Ti the bcc β-Ti type solid solution is stable at temperatures above 500…900°C, and bellow the Pd-Ti alloy showing an eutectoid decomposition [115].

Altogether, it is therefore not wrong to suppose that the entire alloy may be treated as a pseudo-binary (Ag,Sn,Pd)-(Ti,Zr,Pd) alloy. The casting features are completed by the further experimental investigations. Fig. 1.12 presents an optical micrograph (OM) of the coarse separation in the 5 mm diameter rod. Even if the alloy was quenched from the homogeneous liquid state, as it is in this actual case, the cooling rate is not high enough to freeze that state and obtain a fully amorphous phase. The spherical appearance and the morphology indicate that the precipitation took place in the liquid state and then it was frozen upon quenching. Subsequently, each domain developed its own microstructure, as it will be shown later. The 5 mm diameter rods are characterized by a hard outer shell, the dark contrast in Figure 1.12, and a soft core, as illustrated by the light contrast in Figure 1.12. Judging from the appearances

it reasonable to suppose that the soft core is very rich in Ag, while the hard margins are Ti rich. Hence the coexistence of liquid and solid phases can be assumed to have the root in the Ag-Ti phase diagram, but nevertheless the new quinary $Ti_{42}Zr_{10}Pd_{14}Ag_{26}Sn_8$ liquid alloy has multiple atomic interactions.

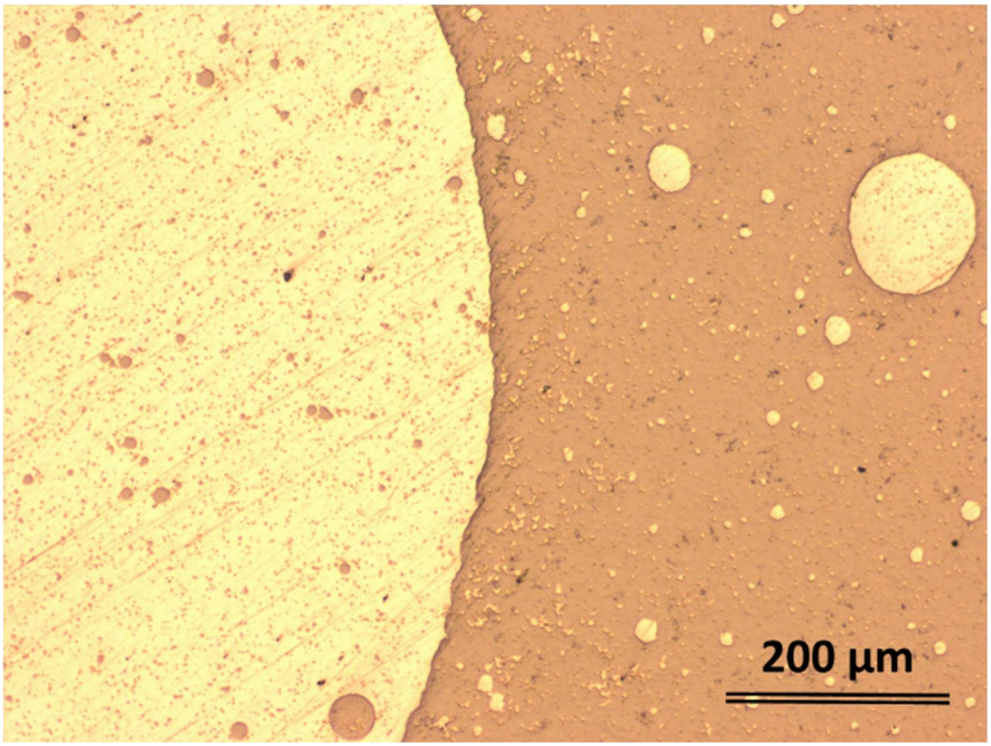

Figure 1.12. Optical micrographs showing the coarse separation from the liquid state. Centrifugal-cast rod with 5 mm diameter [8][20].

1.3.4. Experimental evaluation of the Cu-free alloy

As mentioned previously, the 5 mm diameter rods are characterized by a soft inner core and a much harder outer shell. Figure 1.13 (a) shows the appearance of the border zone between such two areas (optical microscopy, transversal section). The brighter area is the soft zone, while the darker area the hard one. Both dark and bright phases also embed globules that seem to be secondary separations of the same constituents. Additionally, one can observe the formation of some dendrites (marked by an ellipse in both Figure 1.13 (a) and (b)). Unlike the 5 mm sample, the smaller rods with 2 and 3 mm diameter did not form large distinct bright and dark areas, only separations between bright-colored phase inside the dark matrix, similarly to 5 mm rod (see Figure 1.13 (b)). The higher cooling rate attained during casting by the rods with smaller diameters made the precipitated features to be finer, thus for the clarity, the OM image in Figure 1.13 (b) was taken at higher magnification (see the scale bar). The larger magnification reveals not only the existence of another phase, the dendritic-shaped black-colored as marked in both Figure 1.13 (a) and (b), but also the presence of a much finer structure embedded in the dark phase.

Scanning electron microscopy (SEM) using back-scattered electrons (BSE) mode, and energy dispersive X-ray analysis (EDX) were performed on samples extracted from transversal section of 5 mm and 2 mm diameter rods, using a FEI

[20] Open access, editor MDPI AG Basel, Switzerland, financed by Politehnica University Timișoara.

Quanta 250 FEG scanning electronic microscope equipped with an EDAX SDD Apollo X sensor. Considering the complexity of resulted microstructure, quantitative investigations were performed separately on characteristic zones, in order to determine compositions of microstructural constituents. Large scale magnifications by mean of SEM (Figure 1.13) reveal the complex nature of dark constituent evidenced by mean of optical microscopy, as well as homogeneous appearance of the bright phase.

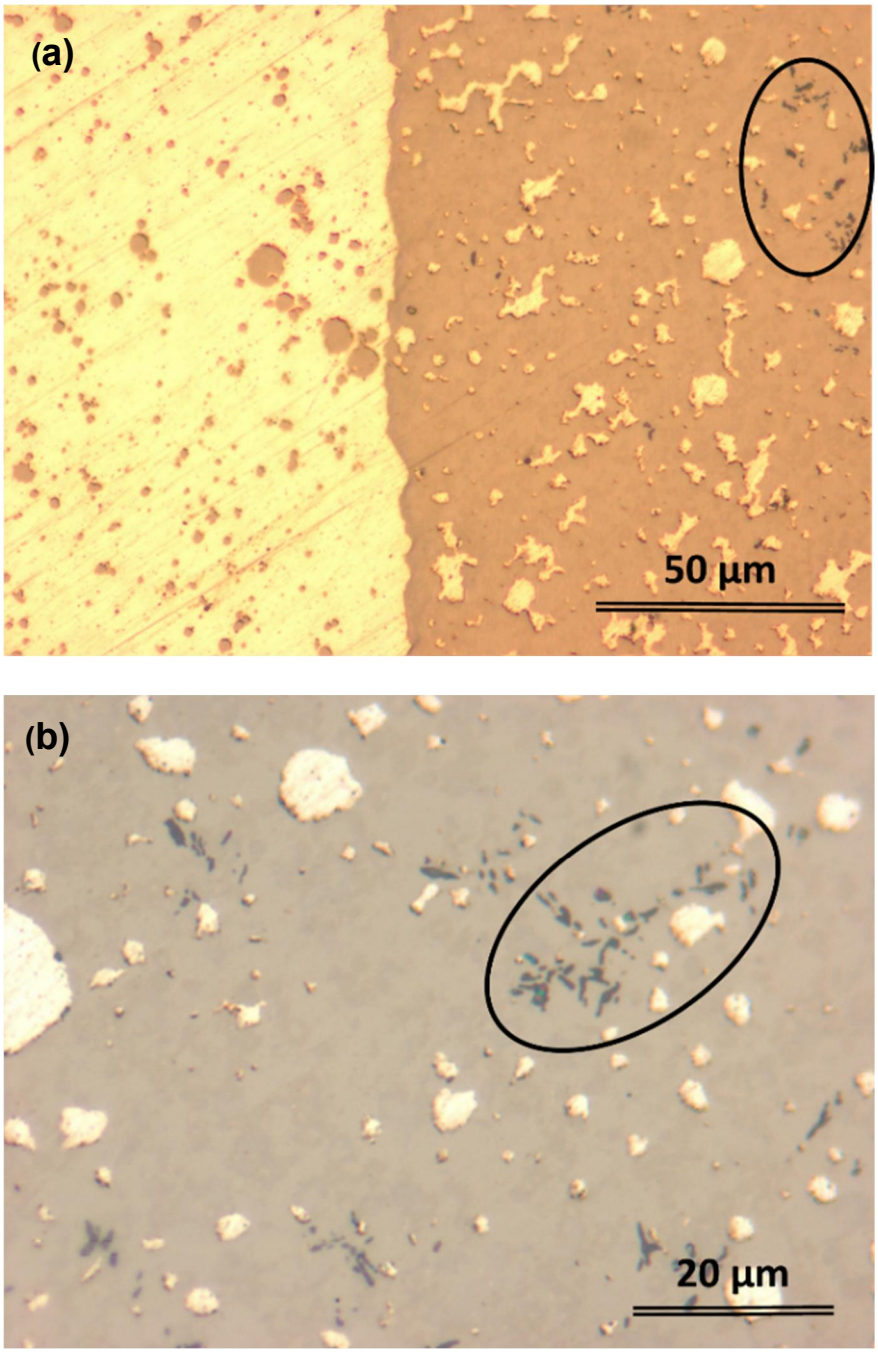

Figure 1.13. Optical micrographs showing the phase separation in (a) 5 mm diameter rod and (b) 2 mm diameter rod [8][21].

[21] Open access, editor MDPI AG Basel, Switzerland, financed by Politehnica University Timișoara.

Several features can be easily identified in Figure 1.14. The bright, mechanically soft area (see the polishing scratches) labelled there with 1, should be the bright area as seen in the optical micrographs. The EDX analyses confirmed that it is almost 100 % Ag, as it was supposed previously. The harder zone contains polygonal crystals with hexagonal appearance (labelled with 2), which may be an intermetallic phase. There are also another brighter phase(s), labelled with 4 and 6, then a darker dendrite (labelled with 5) and the matrix (labelled with 3). Finer dendrites are observed also in the spherical separation (left side of Figure 1.14 (a)), but they were not marked here in order to keep the micrographs as clear as possible. The EDX analysis of all these features revealed the corresponding elemental composition and the data are summarized in Table 1.5.

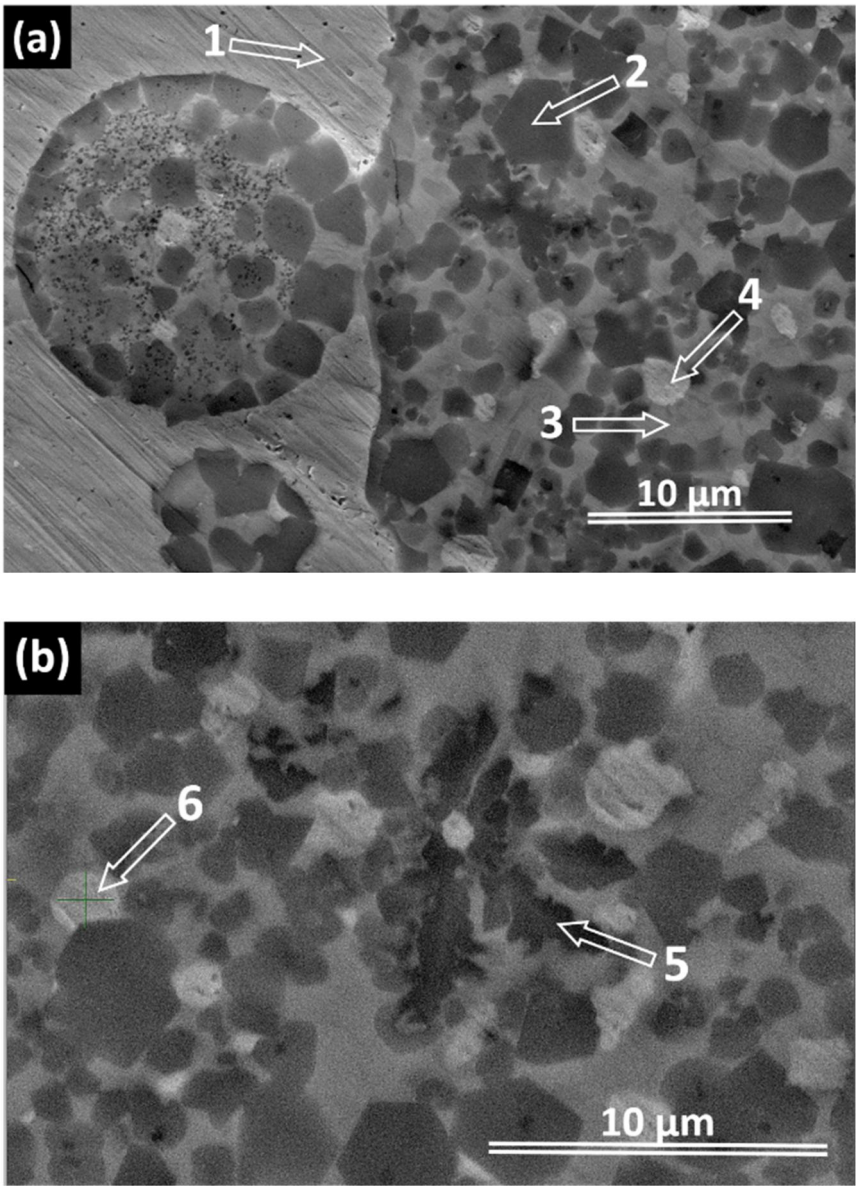

Figure 1.14. SEM micrographs and position of characteristic zone for EDX analysis. (a) Transversal section trough 5 mm diameter rod; (b) Transversal section trough 2 mm diameter rod [8][22].

[22] Open access, editor MDPI AG Basel, Switzerland, financed by Politehnica University Timișoara.

As concluded in section 1.1.3.3 and based on thermodynamic aspects, the early precipitation is indeed Ag-rich in a TiZrPdSn liquid matrix. The bright zones 4 and 6 are again Ag rich and they formed most probably by a secondary precipitation during rapid quenching. The dendrite (i.e. the dark fifth zone) is almost 50-50 Ti-Zr, therefore it is not wrong to suppose that it is a bcc β-Ti type solid solution. The intermetallic phase, marked in Fig. 1.14 with 2, has a more complex composition. Nevertheless, judging from all possible combinations, the most plausible one is of the type $Ti_{3.2}Pd_{0.8}$. The featureless gray area marked here with 3 seems to have the approximated composition $Ti_{29.26}Zr_{32.72}Pd_{24.14}Ag_7Sn_{6.88}$. Judging from the absence of any features, it is to suppose that this matrix is amorphous. Nevertheless, the actual magnification is not high enough to rule-out the presence of additional small crystalline features. Further studies, as transmission electron microscopy, are under considerations. Anyway, preliminary casting tests with a closed composition, $Ti_{30}Zr_{32}Pd_{24}Ag_7Sn_7$, revealed that a fully amorphous ribbons may be fabricated upon melt spinning (results not presented here).

Table 1.5. Atomic compositions of labelled zones in Figure 1.14 [8][23].

Element	Zone 2	Zone 3	Zone 4	Zone 5	Zone 6
Pd	13.60	24.14	0.96	10.89	4.32
Ag	3.97	7.00	75.06	2.28	53.51
Sn	7.54	6.88	1.66	6.37	3.60
Ti	52.37	29.26	0.85	39.93	14.34
Zr	22.51	32.72	21.47	40.54	24.23
TOTAL	100	100	100	100	100

The structure of the rapid-quenched rod samples appears to be relatively heterogeneous, with coarser features as the diameter increases. This is certainly related to the casting parameters and the cooling rates attained by the samples during preparation. The rods with larger diameters are cooled at lower rates as compared to the rods with smaller diameter, therefore the observed microstructural differences (see for example Fig. 1.13). However, as seen in Fig. 1.14, the crystalline precipitations seem to be identical, so the casting parameters influence only the microstructure. As a consequence, further optimization of all parameters during sample preparation may lead toward samples with more homogeneous structure.

The samples were investigated by X-ray diffraction in Bragg-Brentano configuration (FEI X'Pert PRO MPD diffractometer with a copper anode X-ray tube having λ = 0.155 nm, PixCEL detector, vertical θ-θ goniometer and spinning sample holder) in continuous scanning mode using a step size of 0.0130 degrees and 80 seconds step time, at room temperature. The patterns were further analyzed using the X'Pert HighScore Plus software linked with the ICDD PDF-4+ Database.

Surprisingly, in contrast with the numerous elements as observed in SEM, the XRD revealed only few features. Figure 1.15 shows the diffraction pattern stemming from the (a) 2 mm and (b) 3 mm diameter rod. The main 3 peaks are characteristic to the fcc-Ag. The patterns show only few other crystalline peaks, as the one centered at 2θ = 46° in Figure 1.15 (a) and 2θ = 44°, 2θ = 46° and 2θ = 62° in Fig. 5 (b). These peaks cannot be identified with acceptable accuracy.

[23] Open access, editor MDPI AG Basel, Switzerland, financed by Politehnica University Timișoara.

Figure 1.16 presents the thermograms of the 5 mm diameter rod, for both ductile core and hard margin. There are clear differences, the most notable being a huge relaxation-like up to 650 °C and a single melting peak (curve (b)- the core).

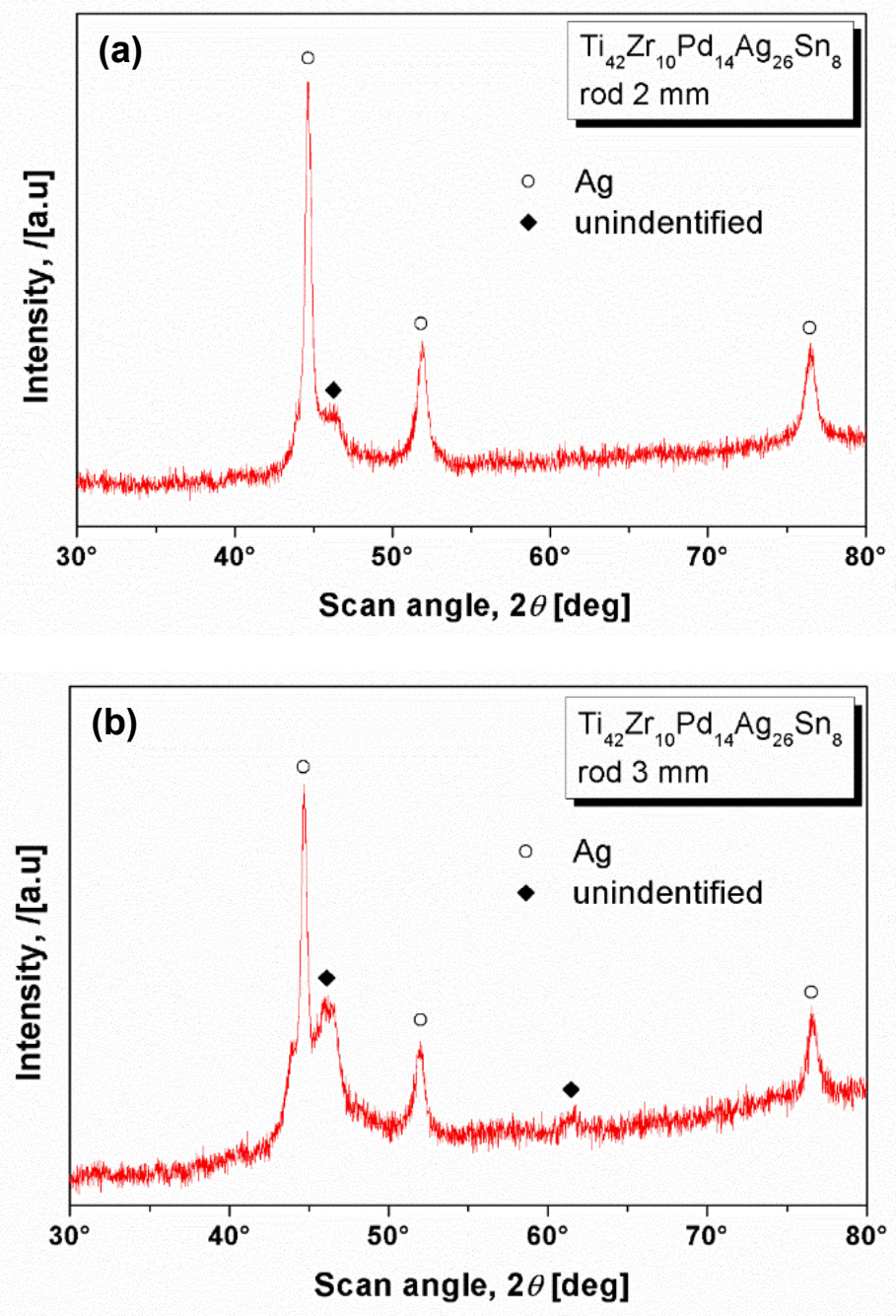

Figure 1.15. XRD patterns of the $Ti_{42}Zr_{10}Pd_{14}Ag_{26}Sn_8$ bulk sample: (a) 2 mm and (b) 3 mm diameter [8][24].

Due to the technical limitations, the DSC was performed only up to 1000 °C, temperature at which, as observed during casting, the alloy is in the liquid + solid state. The liquidus temperature of the core (measured as the onset of the melting event) is at 965 °C, proving that this core is almost pure Ag (i.e. melting temperature 962 °C).

[24] Open access, editor MDPI AG Basel, Switzerland, financed by Politehnica University Timișoara.

Therefore, the relaxation-like event may be generated by the annihilation of the mechanical stress induce upon rapid cooling or by the huge thermal expansion that characterizes the Ag metal. The hard margin (curve (a)) show a double endothermic peak prior 1000 °C. The first of them may be associated with the melting of Ag, stemming from the rest of the Ag trapped in the Ti-rich area and as identified in SEM pictures, while the second one is most probably an allotropic transformation.

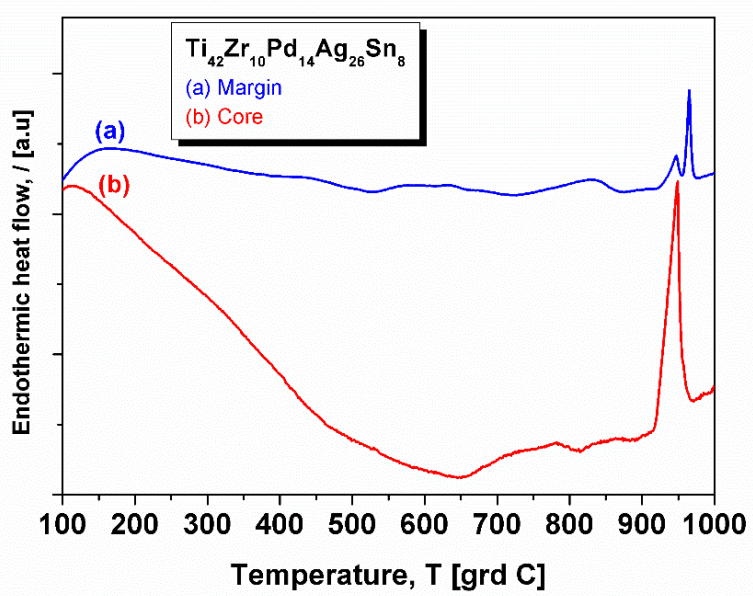

Figure 1.16. DSC thermograms of the 5 mm diameter rod [8][25].

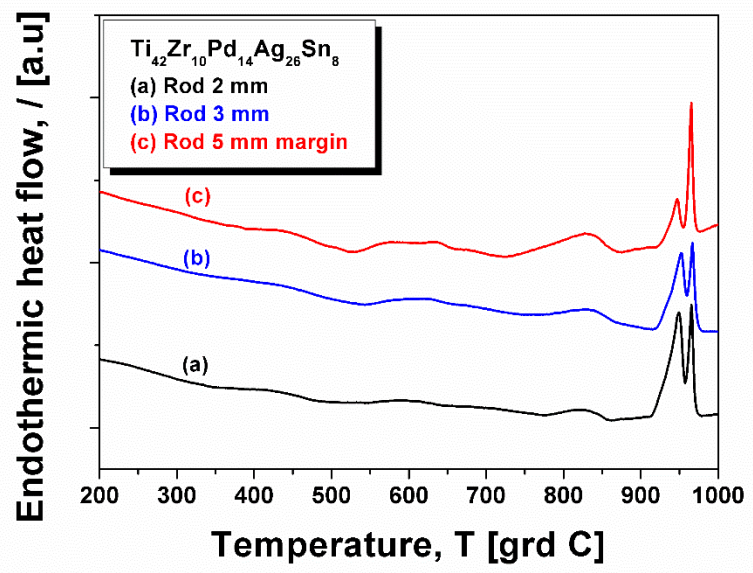

Figure 1.17. DSC thermograms of rods with 2 mm and 3 mm diameter. For comparison, the thermogram stemming from the margins of 5 mm diameter rod is also presented [8][25].

The curve show also a small exothermic event at around 550 °C (which may be associated with the crystallization of the remnant amorphous phase) and a small

[25] Open access, editor MDPI AG Basel, Switzerland, financed by Politehnica University Timișoara.

endothermic peak centered at approximatively 840 °C. This peak indicate as well an allotropic transformation, and, together with the exothermic one, it is present as well in the thermograms measured for 2 mm and 3 mm diameter rods (Figure 1.17, curves (a) and (b) respectively). For better comparison, the DSC curve of the hard margin of the 5 mm diameter rod is re-plotted in Figure 1.17 (curve (c)). All curves show the melting event characteristic to Ag, more pronounced in the case of 2 mm and 3 mm diameter rods, because there the precipitated Ag is better dispersed.

In conclusion, despite the fact that the new designed alloy $Ti_{42}Zr_{10}Pd_{14}Ag_{26}Sn_8$ has the composition inside the BMG domain, the rapidly quenched samples show a complex microcrystalline structure, with only residual amorphous matrix. Therefore it seems that alloys design by mean of molecular orbital method seems to have limitation, and replacement of Cu with Ag did not result in fully amorphous structure. Nevertheless the resulting alloy has some promising features for use as biomaterial. Investigations performed in the newly formulated $Ti_{42}Zr_{10}Pd_{14}Ag_{26}Sn_8$ alloy reveal the composite amorphous – crystalline character with potential for high mechanical properties, including a higher ductility in comparison with the BMGs.

More interesting crystalline fraction is represented predominantly by metallic Ag, which separates as small globules with dimensions within few micrometers range. This microstructural configuration could take full advantage of bactericide effect of metallic silver, as well as high mechanical properties of composite matrix.

Chapter II. Ti-based bulk metallic glass foams for biomedical applications

2.1. Main research directions

Researches have been on development and characterization of an innovative porous Ti-based BMG that contained exclusively biocompatible elements [9][26]. It is well known that orthopedic and dental implants have to meet several requirements that could be antagonistic for some metallic alloys: enhanced mechanical resistance, appropriate load bearing capacity- simultaneously with low rigidity, similar to human bone- and they must prevent the stress shielding effect as well as the reduction of bone density (osteopenia). Conventionally, implants have a modulus of elasticity considerable higher than cortical bone. For example, commercially pure titanium has a rigidity of approximately 100 GPa, while stainless steel, tantalum and cast Co-Cr alloys have more than 200 GPa [29], [34]. The Ti-6Al-4V alloy, which has become over the years the most popular alloy for fabrication of implants because of its high mechanical strength and moderate price, has a Young's modulus around 112 GPa, which is several times higher than the values of 4…30 GPa characteristic for the human bone [29].

Attempts to improve the mechanical properties eventually led to development of new titanium based alloys [29], [77]. For example, both β-Ti alloys and Ti-based bulk metallic glasses (BMGs) have received considerable attention in recent decades [38] [84] [116] [117]. While alloying with β-stabilizing systems, containing Nb, Zr, Ta, Fe, Cr, Mo, etc. may reduce the modulus to below 80 GPa, the processing, precise microstructure control and fabrication costs still remain problematic [29]. The development of titanium-based BMGs fabricated by rapid cooling techniques opens new opportunities, since amorphous alloys have no grains, no grain boundaries, no dislocations and no other discontinuities, and therefore display higher mechanical strength and corrosion resistance than conventional crystalline materials [118], [42]. At the same time, since their deformation mechanism is different in comparison with crystalline alloys [119] [120], they exhibit a unique combination of high yield strength and lower Young modulus. Their formability based on the super-plastic behavior of the amorphous structure is also considered attractive for efficient fabrication of components with intricate shapes [42]. One of the main advantages of metallic glasses is that they may be thermoplastically formed at elevated but technically accessible temperatures [121]. Upon heating into the temperature interval between temperature (T_g) and the crystallization temperature (T_x), the glassy alloys behave as a viscous liquid. The temperature interval between T_g and T_x is usually named supercooled liquid region (SCL) and there the metallic glass may be shaped like a polymer [121].

Another important issue is the biological safety of the alloying elements, which are used to improve the glass forming-ability (GFA) or other properties, since the resulting titanium-based alloys should not be harmful to the human body and at the same time resistant to bio-corrosion. Over the years, a large number of additions have been used to increase the critical diameter of BMGs [122]. However many compositions release toxic and even highly toxic ions. Nickel is extensively used for its capability to increase the GFA of Ti-based multicomponent alloys, but its allergenic effect, as well as suspicions over its genotoxicity, carcinogenicity and potential mutagenicity to the human body, are known for many years [71], [72], [73]. Other

[26] The research program was supported by the German Academic Exchange Service (Deutscher Akademischer Austausch Dienst – DAAD) at the Leibniz Institute Dresden under the supervision of prof Jurgen Eckert and M.Stoica, co-authors of [9].

elements like Co, Cr, Fe, Mo, V and Mn cause severe adverse tissue reactions, while Zn and Be are among the most cytotoxic elements. The discovery of Ni-free BMGs based on Ti-Cu-Zr-Pd was considered a major breakthrough for fabrication of BMGs [58], but the presence of large amounts of Cu gives sensitivity to pitting corrosion in saline fluids, expelling ions with well-documented highly cytotoxic effect [74] [75]. The design of new biocompatible Ti-based alloys is now based on a list of non-recommendable or "toxic" alloying additions, as well as a list of elements seen as non-problematic, also called "vital". The first list usually contains Be, Al, Mo, V, Cr, Mn, Fe, Co, Ni, Cu, Zn, while "eligible" alloying elements are Nb, Ta, Zr, Si, Sn, Pd, In, Sr, B, Ca, and Mg [38] [76] [77]. So far none of the alloying elements that could be accepted as not harmful could provide enough GFA for amorphization of Ti-based alloys, in order to fabricate components with critical dimensions beyond 1 mm by rapid cooling. Therefore, the development of new metallic glasses based on biocompatible Ti-based compositions was focused on producing amorphous ribbons, usually employing melt spinning techniques [78], [79], [80], [81].

Amorphous ribbons could be subsequently processed via powder metallurgy. This new approach also allows fabrication of amorphous materials with controlled porosity, i.e. bulk metallic glass foams (BMGFs) [20]. Combining melt-spinning with powder metallurgy could solve also the problem of biomechanical compatibility of the elastic modulus between bone and implant, since porous metallic glasses could provide adjustable Young's moduli, which could be considerable lower than for dense alloys, and have better resemblance to human bone.

Implant porosity could also bring some other important benefits for orthopedic and dental implants, both when the porosity is only superficial or affects the whole section. For example, superficial porosity increases the interface between implant and bone and provides better mechanical interlocking. The pores may drastically affect the mechanical behavior of the material as a whole. Here one should mention the pioneering work of Inoue, Wada and Louzguine-Luzgine, which analyze the stress concentration around spherical pores [123]. Porous implants could also improve cell adhesion and promote ingrowth of living tissues. However, the optimum pore size and amount of porosity is still subject of intensive debate [29]. Among many reported results, it seems that pores should have maximum size of 100 μm, but larger pores up to 800 μm could sometimes result in improved bone ingrowth [29]. Certainly there it is a link between the age of a patient and the required pore sizes [86]. Generally a higher porosity is beneficial, since it promotes cell migration and transport, but it shall not deteriorate the mechanical properties. Pore interconnectivity could also trigger bone growth, because is favors body fluid transport [124], [125]. Metallic scaffolds have been produced so far using numerous fabrications routes based on sintering of powders or fibers, selective laser melting, plasma spraying, machining, shot blasting, electrochemical oxidation, acid etching etc., with pore sizes ranging between 400 μm and submicron dimensions . The porosity is also very diverse, ranging from 13 to 87 vol. % [85], [86], [126]. Very recently, G. Xie, F. Qin, S. Zhu and D.V. Louzguine-Lugzin succeeded to produce porous Ni-free Ti-based BMG by spark plasma sintering and studied the corrosion behavior in Hanks' solution [127]. They used a mixture of the gas-atomized $Ti_{45}Zr_{10}Cu_{31}Pd_{10}Sn_4$ glassy alloy powder and solid salt (NaCl) powder. The composite samples were immersed into warmed water at 333 K to eliminate the salt phase and the porosity of the samples was measured to be about 50% and 60%.

Researches summarized in the present thesis [9] consider the latest trends in the development of biocompatible alloys, and therefore focuses on the fabrication of Ti-based amorphous alloys, totally free of any harmful element.

Since additions of Zr, Ta and Si, which were decided as alloying elements, cannot provide sufficient GFA for direct casting of bulk components, the $Ti_{42}Zr_{40}Ta_3Si_{15}$ (in atomic %) or 30.37Ti 55.07Zr 8.20Ta 6.36Si (in weight %) alloy was cast as thin ribbons, which were subsequently processed via powder metallurgy techniques. The design of the processing parameters for milling and consolidation of the amorphous ribbons into bulk material took two important conditions in consideration: a) the alloy should preserve its amorphous structure, and b) the resulting mechanical properties should be comparable to human bone in terms of both compression resistance and Young's modulus.

Amorphous 14 vol. % porous pellets with 10 mm diameter and several mm in thickness were produced. To our knowledge this is the first biocompatible Ti-based bulk glassy alloy having mechanical properties close to human bone. These researches may open the gate towards the fabrication of medical implants or scaffolds with immediate effect on bone regeneration.

2.2. Fabrication route of the new $Ti_{42}Zr_{40}Ta_3Si_{15}$ alloy

A master alloy ingot with nominal atomic composition $Ti_{42}Zr_{40}Ta_3Si_{15}$ was prepared by arc melting using high purity elements (purity 99.85 % and better). The ingot was flipped and the melting was repeated three times in titanium-gettered argon atmosphere in order to provide good homogeneity. Pieces of the master alloy were then used to cast amorphous alloy ribbons on a single-roller Bühler melt spinner. The alloy was inductively melted in a graphite crucible and ejected at 1973 K through a round nozzle with 2 mm diameter onto the surface of the Cu-wheel revolving with a tangential speed of 35 m/s. The ejection took place at 400 mbar Ar overpressure. The distance between wheel and crucible was maintained at 1.2 mm. The resulting ribbons were 5 mm wide and 45 μm thick. The casting parameters assure a cooling rate of the order of 10^6 K/s. Ti and Zr may react during melting with the graphite crucible, forming TiC and ZrC. However, according to our previous results and casting experience, the carbides sticks as a thin layer on the internal crucible walls and, as will be shown further, no carbides form in the melt. The slight compositional depletion in Ti does not further affect the GFA. However, some C may be dissolved during melting and it can be eventually found in the melt-spun ribbons.

The ribbons were cut into small pieces, and then ball milled in a planetary mill (Retsch PM400) under argon atmosphere, using hardened steel balls and vials at 300 rpm. All sample handling was carried out in a glove box under purified argon atmosphere (less than 0.1 ppm O_2 and H_2O). The ball-to-powder weight ratio was about 10:1. Since preliminary experiments indicated that the ribbons are ductile at normal temperature and adhere to vial and balls, milling at cryogenic temperature was adopted for a total time of 1 hour. The vials were immersed in liquid nitrogen for 15 minutes and then immediately milled for another 15 minutes. The cycle was repeated four times. The resulting powders were sieved to below 300 μm for subsequent consolidation. Disks with 10 mm in diameter and about 3 mm thick were finally fabricated by uniaxial hot pressing under argon atmosphere. The compaction took place at 823 K and the machine load of about 70 kN was kept constant for 3 minutes.

2.3. Microstructural evaluation of the $Ti_{42}Zr_{40}Ta_3Si_{15}$ alloy

Selected samples of ribbon, milled powder and consolidated pellets were investigated by scanning electron microscopy (SEM) using a FEI Quanta 250 FEG scanning electronic microscope in order to evaluate the microstructures, as well as the

final porosity of consolidated alloy. The analyses were performed using the secondary electron (SE, i.e. topological contrast) and back-scattered electron (BSE, i.e. contrast upon composition) modes. To check the structure of the starting ribbons, as well as of the compacted samples, high-resolution transmission electron microscopy (HR-TEM) was also performed. The investigations were carried out at 200 kV accelerating voltage on a FEI Tecnai G2 200 kV S/TEM microscope. The TEM samples were prepared with a FEI Quanta 3D dual beam microscope, using focused beams of gallium ions.

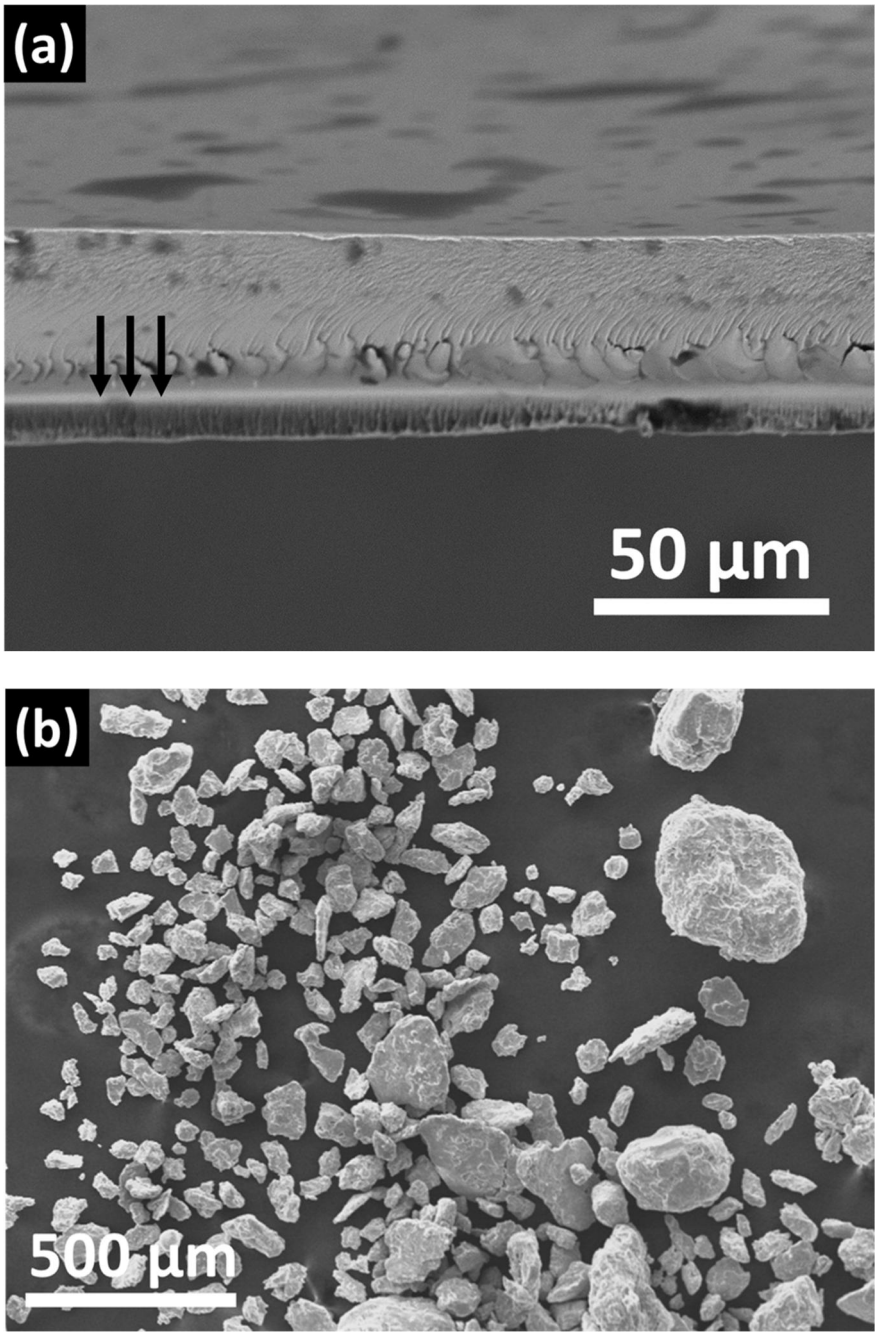

Figure 1.18. SEM micrographs, BSE mode. (a) melt-spun ribbon, cross-section fracture appearance upon bending. The black arrows indicates the zero-load fiber. (b) the same ribbons after cryo-milling [9][27].

[27] Reprinted with permission by Elsevier.

The micrograph presented in Figure 1.18 (a) (SEM, BSE) depicts a fractured cross-section of the starting material, i.e. an amorphous melt-spun ribbon. The thickness of the ribbon is relatively constant, approximatively 45 μm. What is interesting to observe is the appearance of the fracture surface, which indicates a brittle-ductile fracture mode. The ribbon was sectioned by bending, therefore one face supports tensile loads, while the opposite is in compression. Consequently, there should be a median line, which faces zero mechanical load. This line is marked in Figure 1.18 (a) by black arrows and is placed far from the middle of the cross-section. This indicates that one of the fracture mechanism is dominant, i.e. in this case the ductile behavior. Hence, the mechanical milling at room temperature of such ribbons is extremely difficult- instead of fragmenting them one would obtain laminates. Therefore, the milling was performed at cryogenic temperatures, as it was described in previous. The resulting powders are presented in Figure 1.18 (b) (SEM, BSE). They are irregular and have different dimensions, which further will contribute to the compaction process, assuring also a very good mechanical interlocking.

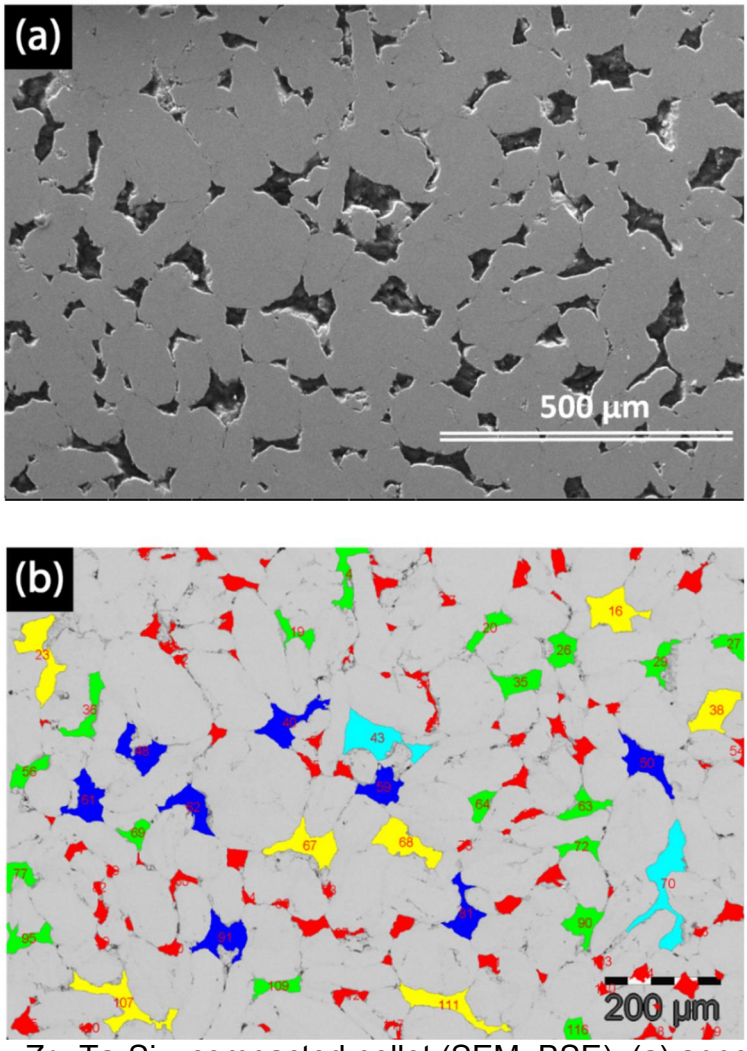

Figure 1.19. $Ti_{42}Zr_{40}Ta_3Si_{15}$ compacted pellet (SEM, BSE). (a) appearance of the polished cross-section. (b) same appearance after image processing [9][28] [29].

[28] Special thanks to C. Locovei, co-author of [9] [15] [16], for contribution in the computerized processing of microstructural images contained by the present thesis.
[29] Reprinted with permission by Elsevier.

Figure 1.19 (a) (SEM, BSE) shows the appearance of $Ti_{42}Zr_{40}Ta_3Si_{15}$ compacted pellets, here a polished cross-section. The particles are very good interlocked and plastically deformed, which assures robustness and mechanical anisotropy of the fabricated bulk samples. There are no evident crystalline entities (at this scale) and the uniform contrast indicates compositional homogeneity. The porosity of the sample was evaluated by graphical methods, i.e. analyzing the contrast differences of the photographed area, and it was found that the relative volumetric density of the sample is 86 vol. %, which gives a porosity of 14 vol. % (Figure 1.19 (b)).

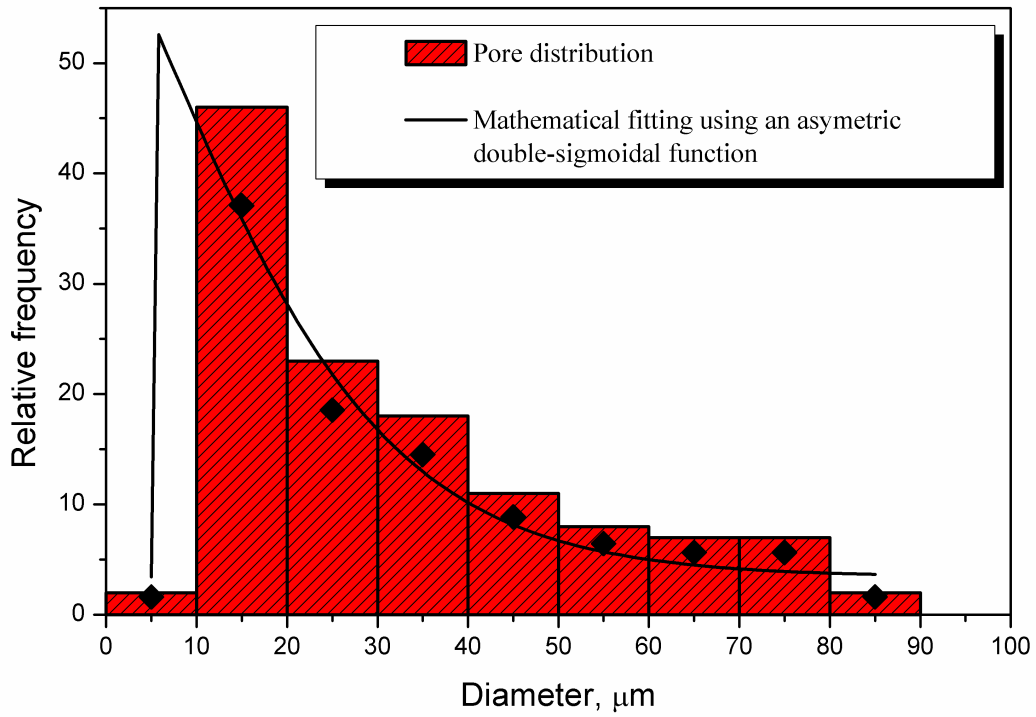

Figure 1.20. Distribution of the pore dimensions and the corresponding fitting curve [9][30].

The distribution of the dimensions of the pores is presented in form of a histogram in Figure 1.20. Almost half (i.e. ~46 %) of the total number of pores have an average dimension of 15 microns. Interestingly, there are only very few pores below 10 microns, i.e. ~2 % of the total number of pores. Upon mathematical processing of the distribution it was found that the best fitting is performed by an asymmetric double sigmoidal function, represented by Eq. (1.3), which provides highest determination coe□cient (R2 = 0.93). For clarity, the fitting is drawn in Figure 1.20 as a continuous line.

$$y = y_0 + \frac{A}{1+\exp\left(-\frac{x-x_c+w_1^{1/2}}{w_2}\right)}\left(1 - \frac{1}{1+\exp\left(-\frac{x-x_c-w_1^{1/2}}{w_3}\right)}\right) \qquad (1.3)$$

[30] Reprinted with permission by Elsevier.

In Equation (1.3) y represents the relative frequency of the pore dimensions (the ordinate in Figure 1.20), while x is the pore diameter (abscissa in Figure 1.20). Therefore y_0 is the offset of the relative frequency, while x_c is the center of the curve, A the amplitude of the function and w_1, w_2 and w_3 the width of the used functions. The numeric values were obtained by fitting and are given in Table 1.6.

Table 1.6. The fitting coefficients of asymmetric double sigmoid function in Eq. (1) [9][31].

Offset y_0	Center x_c	Amplitude A	Width w_1	Width w_2	Width w_3
3.42231	5	101.42153	5.7248E-20	1.45652E-9	13.25477

The asymmetric distribution of dimensions of resulting pores may be caused by the fact that no operation of powder selection was performed except sieving below 300 μm. As it is observed from Equation (1.3) and Figure 1.20, above a certain diameter (i.e. 15 μm), the pore dimensions decrease more or less in an exponential manner. It may be expected that separation of particles in narrow granulometric fractions could provide better pore distribution. Therefore, by adjusting the particle sizes and compaction conditions one may tailor the porosity of the final sample and so the resulting (bio)mechanical properties.

Figure 1.21 (SEM, SE) shows for comparison the appearance of a human femur. The actual pictures were taken from a cross-section of the bone, in two different places. In order to compare the metallic compacted pellet with the bone, the micrographs were arranged in such way than the scale bars have the same apparent length (i.e. 500 μm) in all 1.19 and 1.21 pictures.

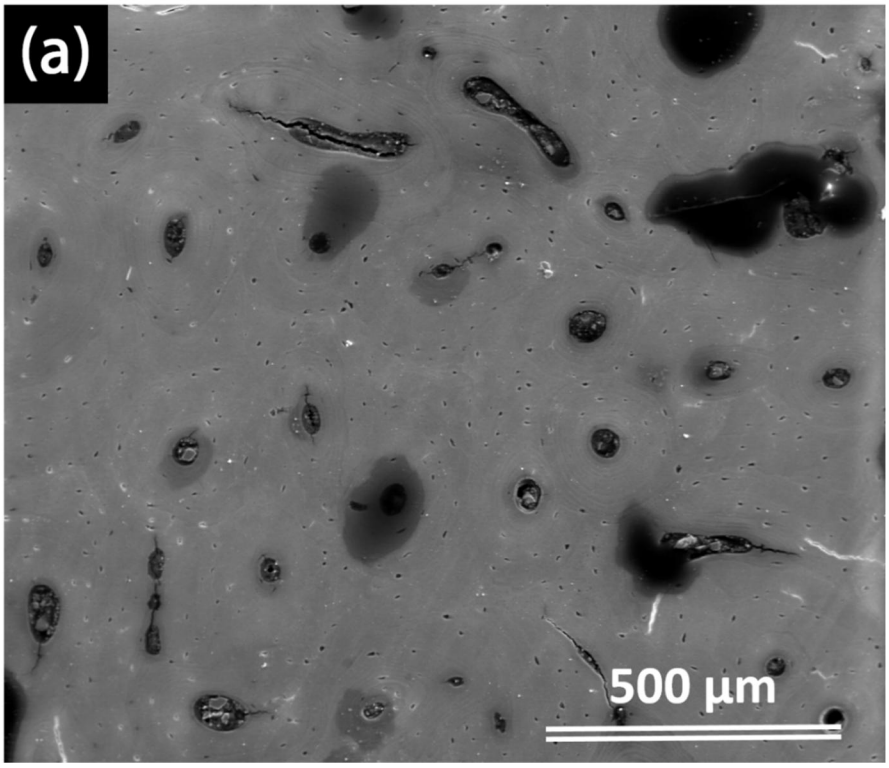

[31] Reprinted with permission from Elsevier.

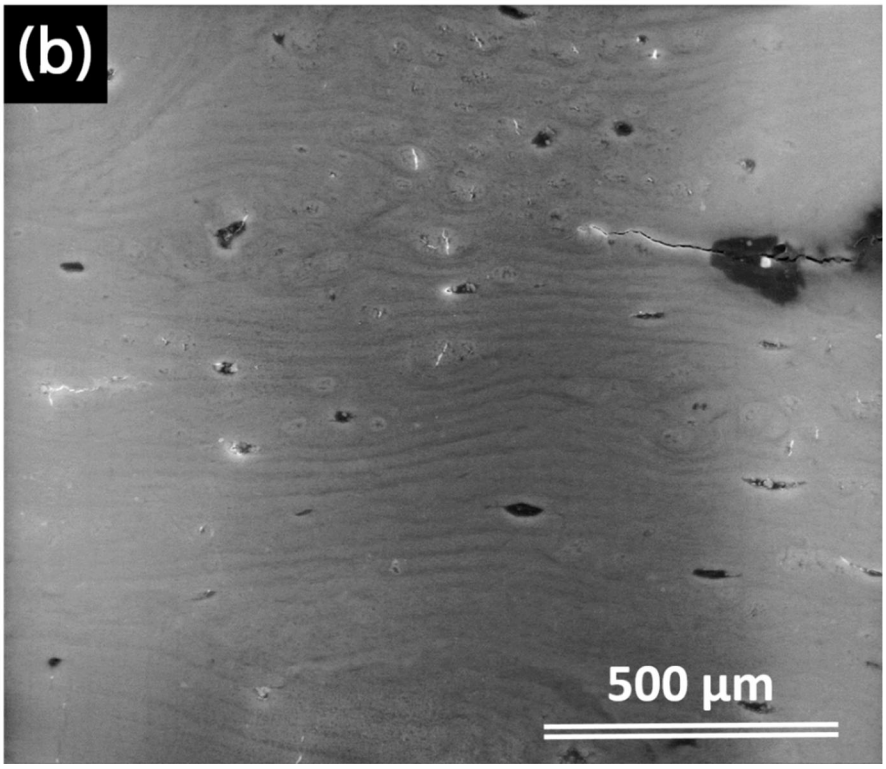

Figure 1.21. Cross-section of a human femur [9][32] [33].

As usual, one can observe two types of pores, big pores with dimensions in the mm-range and small pores with dimensions around 10-15 microns. It is known that at the micron scale and above, bone tissue is in fact a hierarchical composite [128]. At the lowest level (~100 nm scale), it is a composite of mineralized collagen fibrils. At the next level (1- to 50-µm scale), these fibrils can be arranged in two forms, either as stacked thin sheets (i.e. lamellae of about 25-30 µm thickness, as seen here in Figure 1.21 (b) that contain unidirectional fibrils with alternating angles between layers or as a block of randomly oriented woven fibrils. It seems that lamellar bone is most common in adult humans, whereas woven bone is found in situations of rapid growth, such as in children and large animals, as well as during the initial stages of fracture healing [128].

Figures 1.22 (a) and (b) (SEM micrographs, SE mode) show the detailed morphology of the compacted $Ti_{42}Zr_{40}Ta_3Si_{15}$ pellet at higher magnification. One can clearly see that the compaction is realized through the viscous flow of the amorphous ribbons. Furthermore, the fine, brighter filaments, may be due by the presence of Ti and/or Zr oxides on the ribbons surface. Such layers are prone to form during milling and during hot compaction and may provoke extra, very fine porosity, as can be seen at higher magnification in Figure 1.22 (b). Such fine porosity is highly desired; due to the capillarity, the small pores promote blood circulation. The filaments/lamellae seen in Figures 1.22 (a) and (b) resemble with the bone lamellae as seen in the bone cross-section presented in Figure 1.21 (b). Therefore, it is not wrong to conclude that the morphology of the $Ti_{42}Zr_{40}Ta_3Si_{15}$ compacted pellets resembles somehow to that of the bone. Nevertheless, upon optimization of milling time, chosen powder fraction and

[32] Images of human bone have been produced with the help of prof.dr. F. Tatu and A. C. Miu MD from ‘‘Victor Babeș” University of Medicine and Pharmacy of Timisoara.
[33] Reprinted with permission by Elsevier.

compaction parameters (i.e. *fine tuning* of preparation parameters), one may obtain compacts with morphologies that perfectly mimic the human bone. In conclusion, such compacted pellets can be successfully used for the envisaged application as biocompatible bone implants.

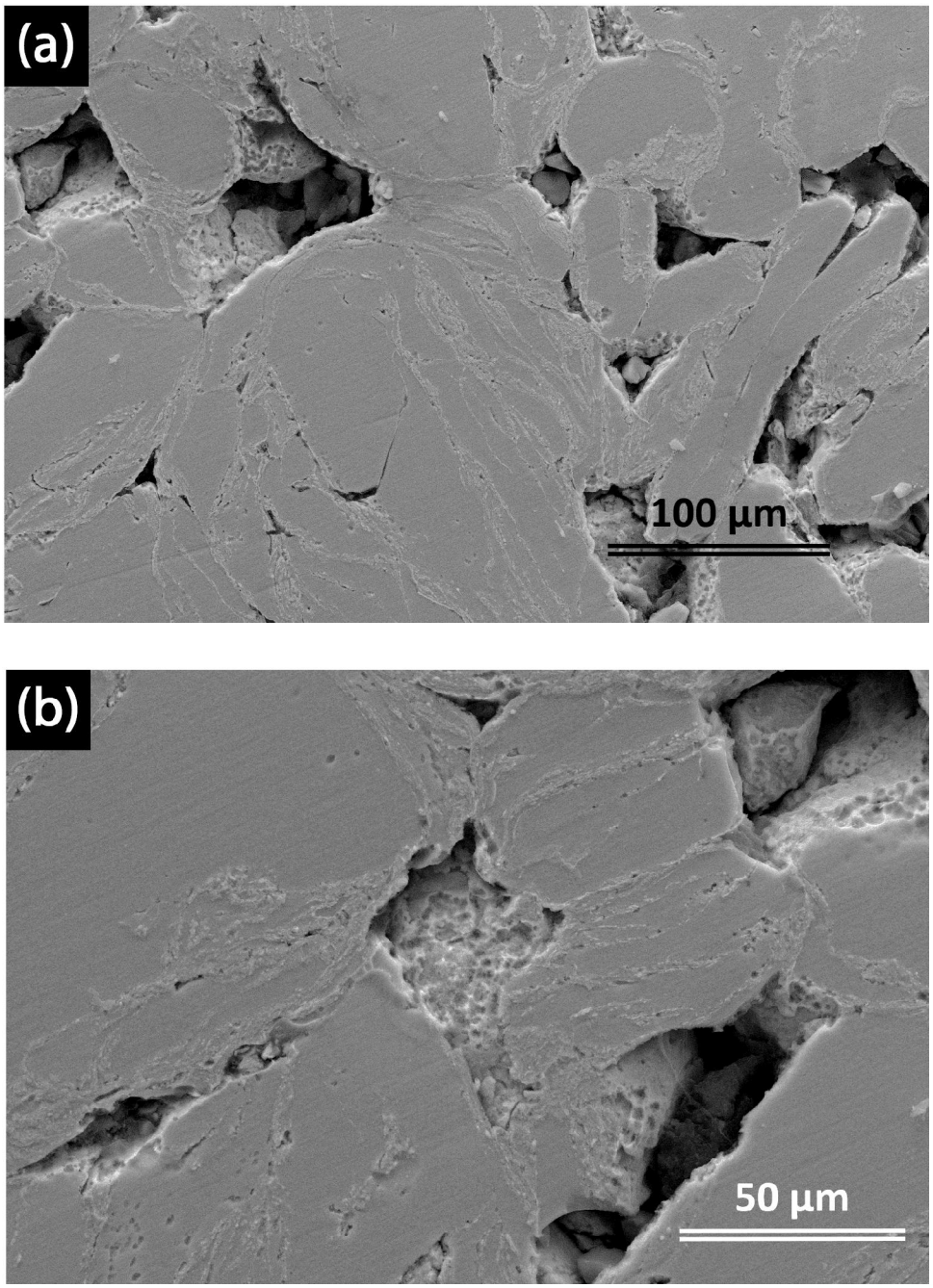

Figure 1.22 (a) and (b) SEM micrographs, SE mode, showing at higher magnifications the appearance of the $Ti_{42}Zr_{40}Ta_3Si_{15}$ compacted pellet cross-section from Fig. 1.19(a) [9][34].

X-rays diffraction (XRD) was performed on ribbons, powder and consolidated disks in order to determine the possible deviations from the amorphous nature of the

[34] Reprinted with permission by Elsevier.

$Ti_{42}Zr_{40}Ta_3Si_{15}$ alloy along its fabrication route. The investigations were performed on an Inel Equinox 1000 high resolution X-Ray diffractometer with curved position sensitive detector, using Co radiation (λ = 1.78897 Å).

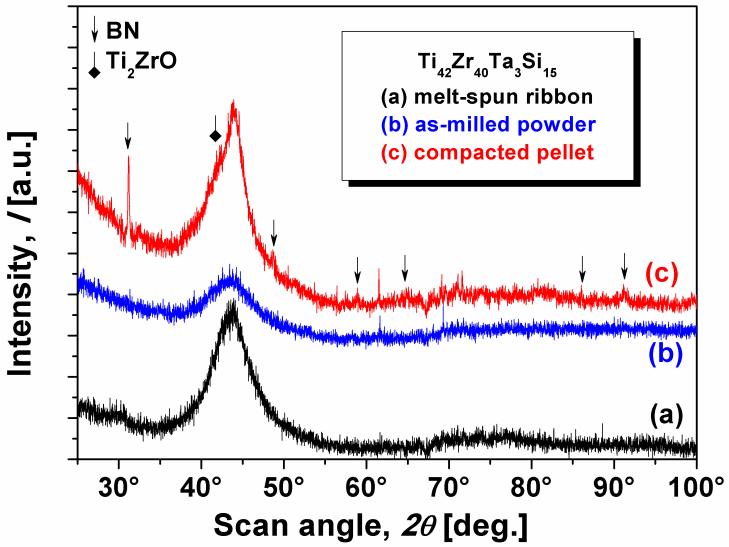

Figure 1.23. XRD for $Ti_{42}Zr_{40}Ta_3Si_{15}$ glassy alloy at every stage: melt-spun ribbon, as-milled powders and hot compacted pellets [9][35].

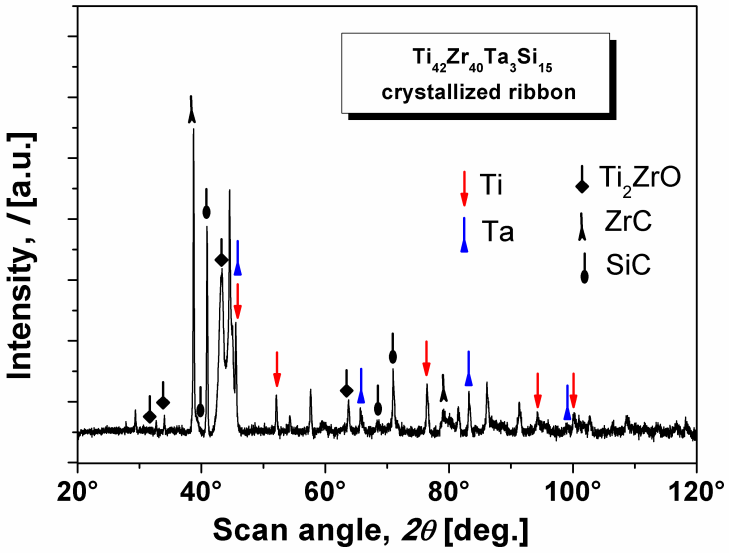

Figure 1.24. XRD corresponding to $Ti_{42}Zr_{40}Ta_3Si_{15}$ alloy after complete crystallization. The phases present there are completely new and not seen in the diffraction measured for the compacted product [9][35].

[35] Reprinted with permission by Elsevier.

To obtain a compact with good macroscopic properties, one has to be sure that the starting material (i.e. the melt-spun ribbon), the milled powders and the compact are structurally identical. The XRD investigations revealed that the samples are amorphous at all stages and the processing parameters enabled to avoid crystallization. Figure 1.23 presents the XRD patterns at every stage.

They are characterized by the presence of broad peaks, indicating an amorphous structure. Whereas the melt-spun and milled ribbons are with no doubt amorphous, the pattern corresponding to the compacted pellets shows some sharp Bragg peaks. They are characteristic for the complex Ti2ZrO phase, which, as mentioned previously, may form either during milling by reaction with the residual oxygen in the milling vials (i.e. oxygen trapped/adsorbed in the vial walls and/or milling balls, eventually traces in the Ar atmosphere or because of sealing flaws- the vials suffered strong cooling-heating thermal cycling, which may bring large dilatations and contractions) or, most probably, during heating for compaction.

The SEM micrographs in Figures 1.23 and 1.24 already provided some evidence for the existence of oxide layers. The rest of the sharp reflections was identified as hexagonal boron nitride (BN), which is the lubricant used during the compaction (otherwise the pellets cannot be extracted from the compaction die). However, as it was anticipated before, no TiC or other carbides were found. This indicates that if there it is a reaction between the master alloy and the casting crucible, this is not pronounced or at least does not influence the experimental results.

In order to rule out the possibility of crystallization during the compaction and to study the appearance of carbides, pieces of the melt-spun ribbons were separately annealed at 1273 K, which is a temperature where the alloy is fully crystallized (the thermal behavior will be in detail described further in the next section). The corresponding XRD patterns are shown in Figure 1.24. Numerous crystalline reflections are present and they could be only partially identified. However, among the possible phases are bcc β–Ti, bcc-Ta, complex oxides as Ti2ZrO, some ZrC and SiC.

The un-marked peaks in Figure 1.24 could correspond to some intermetallic compounds like ZrSi and ZrSi2, but their identification could not be done with accuracy.

Together with the previous results, these findings indicate that indeed the master alloy may react with the graphite crucible during melting prior to casting, but the formation of carbides would require either a much higher temperature or a longer reaction time. Therefore, for the short manipulation time, structural modification induced by C can be completely ruled out. Even in the case of carbide formation, the carbides would not affect the biocompatibility of the final product.

For a more detailed analysis, HR-TEM was employed. Figure 1.25 (a) shows a typical micrograph of a melt-spun ribbon. No traces of crystallinity are observed, the micrograph displays only a homogeneous gray contrast.

The inset shows the selected area diffraction pattern (SAED), where only amorphous diffraction rings can be observed.

However, for the compacted sample (Figure 1.25 (b)) very fine crystalline entities with dimensions below 10 nm can be found (marked by white ovals).

Whether these nanocrystals are formed upon sample preparation or upon compaction it is not clear. There are not enough details to identify them precisely and it cannot be ruled-out that they are Ti_2ZrO or BN, as observed in the XRD patterns.

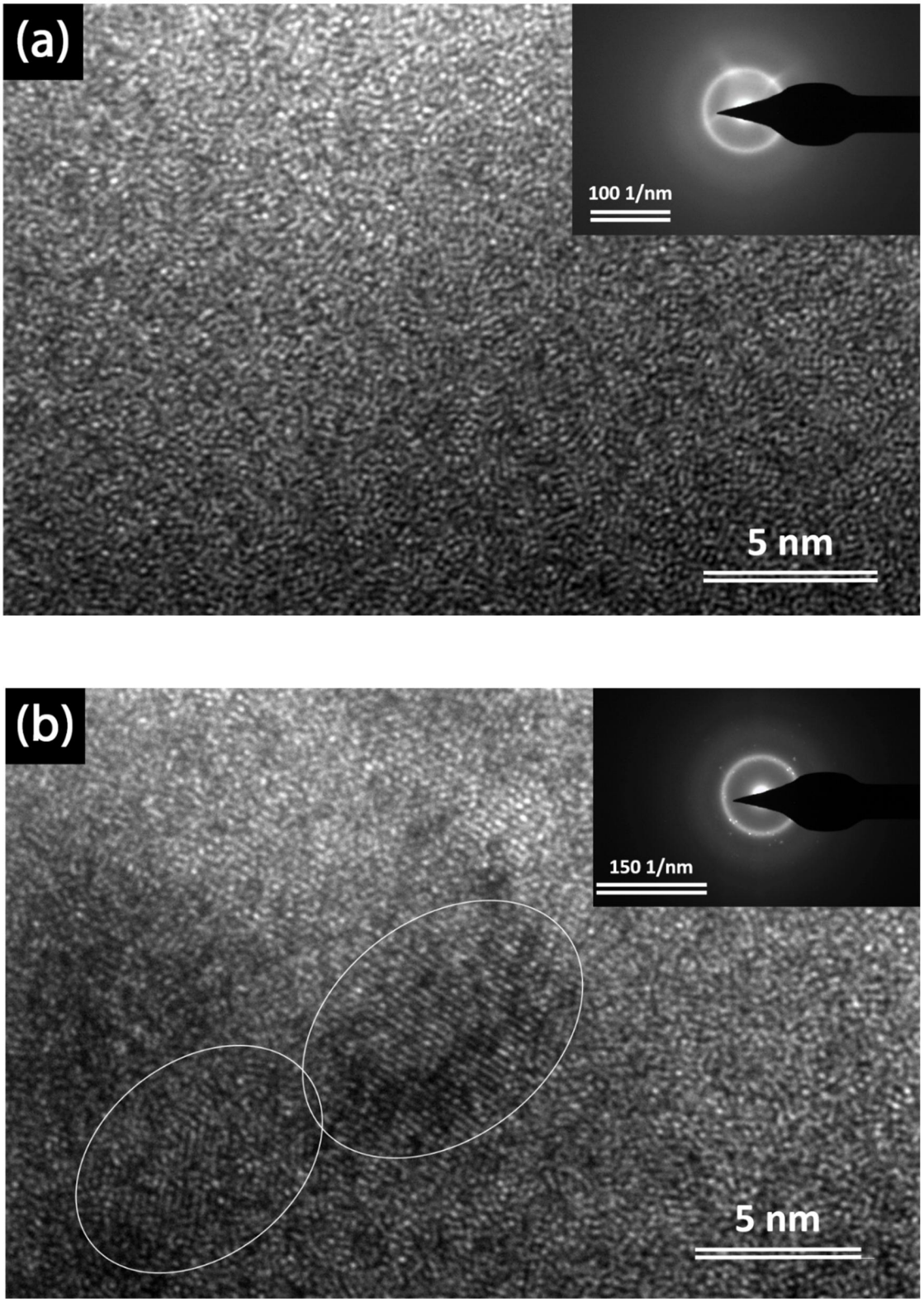

Figure 1.25. HR-TEM micrograph of $Ti_{42}Zr_{40}Ta_3Si_{15}$ glassy alloy. (a) Melt-spun ribbon and (b) compacted pellet. The insets show the selected area diffraction patters [9][36].

[36] Reprinted with permission by Elsevier.

2.4. The thermal stability of $Ti_{42}Zr_{40}Ta_3Si_{15}$ alloy

The thermal stability of the alloy at different fabrication stages, i.e. ribbon, powder, and hot pressed disk, was determined by heating small samples of the material up to a temperature of 1200 K under Ar flow in a Netzsch differential scanning calorimeter (DSC). The heating rate was set to 20 K/min. The glass transition temperature T_g and the crystallization temperatures T_x were measured as the onsets of their corresponding heat flow events in the DSC curves. The corresponding crystallization enthalpy, ΔH_x, was measured by integrating the exothermic crystallization event.

The thermal stability and the evolution of crystallization are displayed in Figure 1.26, which shows the DSC thermograms for as-spun ribbons, as-milled powders and compacted pellets, all recorded at 20 K/min heating rate. The behavior of all the different specimens is similar (but not identical) and all products are amorphous.

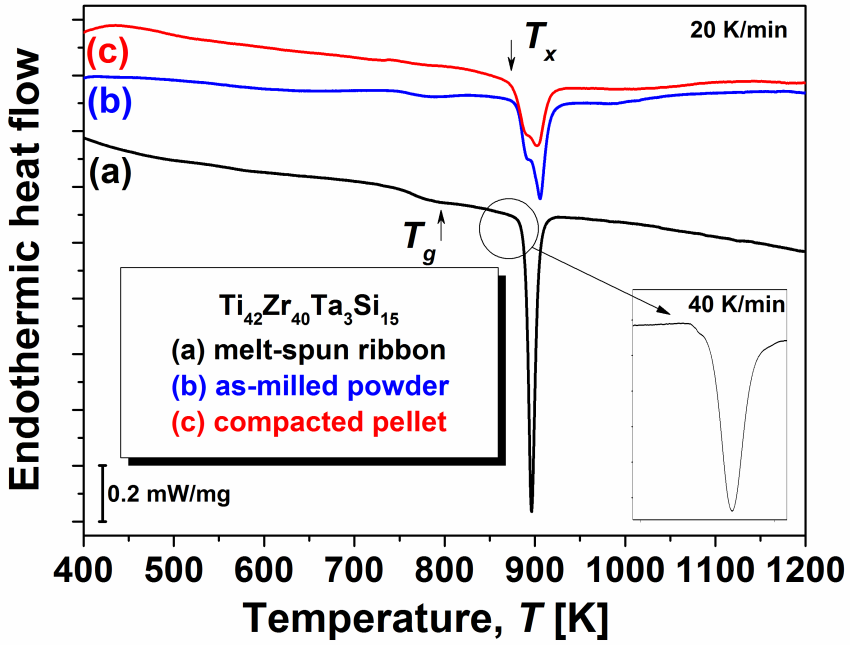

Figure 1.26. DSC thermograms, measured at 20 K/min, for melt-spun ribbon, as-milled powder and compacted tablet. The inset shows a detail, measured at 40 K/min, just before the main exothermic event [9][37] [38].

Table 1.7. Glass transition temperature T_g, crystallization temperature T_x, extension of the supercooled liquid region $\Delta T_x = T_x - T_g$, crystallization enthalpy - ΔH and the amorphicity degree measured for different samples. The absolute errors for thermal measurements are ± 1.5 %[38].

Sample	T_g [K]	T_x [K]	ΔT_x [K]	$-\Delta H$ [J/g]	Amorphicity
Ribbon	786	889	103	32.25	100%
Powder	782	879	97	24.51	76%
Compact	776	874	98	22.43	70%

[37] Special thanks for contributions in the interpretation of DSC curves contained by the present thesis to M. Stoica and A. Raduta, co-authors of [9] [10].
[38] Reprinted with permission by Elsevier.

The melt-spun ribbons, as well as the as-milled powders and the compacted pellets, show a characteristic glass transition event, followed by one or more clear exothermic events, characteristic to the crystallization. The main thermal parameters (i.e. glass transition temperature T_g, crystallization temperature T_x, extension of the supercooled liquid region $\Delta T_x = T_x - T_g$, crystallization enthalpy $-\Delta H$) are summarized in Table 1.7. Additionally, the degree of amorphicity (i.e. the amount of amorphous phase in the metallic alloy) was calculated as the ratio between the actual crystallization enthalpy and the enthalpy corresponding to a 100 % amorphous sample (i.e. in this case the melt-spun ribbons).

In the case of ribbons the crystallization proceeds mainly through a sharp exothermic event. In the case of as-milled powder, the crystallization proceeds through two overlapped exothermic events. The glass transition slightly shifted toward lower temperatures (i.e. 782 K as compared to 786 K for the ribbon, see Table 1.7). The corresponding crystallization temperature shifts as well, from 889 K to 879 K, this time more consistently. As a consequence, the extension of the supercooled liquid region decreases by 6 degrees, which is definitely larger that the possible measurement errors (which are ± 1.5 %). However, it is still large enough to assure a proper time-temperature window for hot compaction. Furthermore, the total crystallization enthalpy is lower, i.e. -24.51 J/g compared with -32.25 J/g. This may indicate that the milled powders contain a fraction of already crystallized products. All these differences could be provoked as well by the slight oxidation during milling, and this would be in agreement with the other experimental observations described previously.

The compacted pellet shows as well two overlapped crystallization events, but this time more apparent. The glass transition and the crystallization shift both towards lower temperatures by almost the same amount, i.e. 6 and 5 degrees, respectively, and consequently the extension of the supercooled liquid region remains almost the same. The crystallization enthalpy decreases only slightly compared to the milled powder.

Apparently, in the case of ribbons only one crystallization event prevails. In fact the first crystallization event is also seen, as evidenced by the DSC analysis performed at 40 K/min (see the inset in Figure 1.26).

The observed behavior can be explained in the following way. The crystallization proceeds normally through the formation of two crystalline phases, from which one either has very low volume fraction or further transforms in something else. The formation of one of these phases is catalyzed in the as-milled and compacted powder and this could have two reasons. It may form directly during milling, and this would explain the reduced crystallization enthalpy, but then some extra reflections should appear in the corresponding XRD patterns- unless the crystalline volume fraction is small and therefore below the detection limit. The second possibility is related to the presence of oxygen, which may provoke changes in the thermal stability and the crystallization behavior. Then, upon compaction, this phase may grow due to the increase of the atomic diffusivity at elevated temperatures. This supposition is sustained by the further reduction in the crystallization enthalpy, but again, the presence of this phase cannot be seen in XRD. Anyway, one should not forget that the HR-TEM micrograph (Figure 1.25 (b)) shows some (nano)crystalline features. Nevertheless, a small amount of (nano)crystallization is not excluded nor harmful, if the targeted properties (i.e. mechanical and biocompatibility) are not changed.

Since one of the most important technological problem during processing of amorphous ribbons by mean of powder metallurgy is conservation of amorphous structure along the fabrication route, especially when heating is involved, the

thermostability of new formulated composition should be determined in terms of critical transformation points and activations energy. Therefore a separate research program [10] is dedicated to the evaluation of thermal stability for the fully amorphous $Ti_{42}Zr_{40}Ta_3Si_{15}$ ribbons during fabrication based on calculation of activation energy for crystallization.

As mentioned before, the GFA of considered alloy is too low for casting of BMG components, i.e. having critical dimensions above 1 mm. Therefore, the fabrication route includes casting of thin ribbons by mean of melt spinning, which allows amorphization of alloys with low GFA. The ribbons are subsequently milled and resulting powder consolidated by mean of hot pressing. Investigations of differential scanning calorimetry (DSC) for calculation of activation energy of crystallization, were performed using samples of about 20 mg under argon gas on the same Netzsch differential scanning calorimeter (DSC) as before. This activation energy for crystallization is useful for further optimization of hot pressing parameters, i.e. processing temperature and duration.

Ribbons fabricated by ultra-rapid cooling are in a metastable state, characterized by a higher internal energy than the stable crystalline state. Consequently, during heating, the amorphous alloys tend to reduce the level of free energy during the first stage of transformation, while amorphous structure is still preserved, and crystallization occurs during the second stage of transformation. Heating below crystallization point produces reduction of the free energy as result of relaxation processes, which includes short-range structural changes, causing also some changes of physical characteristics, such as specific volume, specific heat, hardness, ductility etc. Structural changes during second stage of heating involve some polymorphous reactions, which produce crystallization, without any changes of chemical composition. Some amorphous alloys have more complicated crystallizations associated with reactions of decomposition [129].

It is of utmost importance to determine crystallization temperature of amorphous alloys, since large majority of applications require preservation of amorphous structure for stability of properties, throughout subsequent processing and further on during the entire life of components. Alloys compositions that are furtherly processed by mean of powder metallurgy must have transformation temperature as high as possible because consolidation of powder involves hot processing, such as sintering, pressing, extrusion etc.

Crystallization of metallic glasses could be characterized by indicating the formation rate of crystalline germs Q, the crystals growth rate V and activation energy of crystallization E_a. If isothermal crystallization is considered, parameter Q is determined by using the following relation:

$$Q = Q_0 \times e^{-\frac{N\Delta G_C}{RT}} \times e^{-\frac{E_n}{RT}} \qquad (1.4)$$

The symbols in equation (1.4) have following significations: Q_0 – rate on which the grain number increases from 10^{30} to 10^{35} germs·cm^3, N – Loschmidt's number, E_n – activation energy necessary to pass an atom over the limits of nucleus, ΔG_c – amount of free energy required to form nuclei having radii equal to critical radius.

Similarly, equation (1.5) expresses the crystals growth rate:

$$V = V_0 e^{-\frac{Q_q}{RT}} \left(1 - e^{-\frac{\Delta G_C}{RT}}\right) \qquad (1.5)$$

where symbols have following meaning: Q_q – quantity of energy necessary for an atom to leave amorphous state and associate to crystal, ΔG_C – change of free energy during crystallization, V – crystal growth rate, and V_0=a_0×v_0, where a_0 is the atomic diameter and v_0, is the atomic jump frequency.

If the temperature level T is much below the melting point T_f of alloys, i.e. there is a very high undercooling, changes of energy ΔGc >> RT, equation (1.4) and (1.5) can be expressed respectively as [130]:

$$V = V_0 e^{-\frac{Q_q}{RT}} \qquad (1.6)$$

and

$$Q = Q_0 e^{-\frac{EQ_n}{RT}} \qquad (1.7)$$

New formulas in equation (1.6) and (1.7) indicate that both the growth and crystallization rates could be similarly expressed with the Arrhenius equation.

The activation energy of crystallization E_a [Jmol^{-1}] could be calculated following Kissinger's relation [131], [132], [133] [134], [135], [136]:

$$ln\left(\frac{T_v^2}{V_i}\right) = \frac{E_a}{RT_v} + A \qquad (1.8)$$

The symbols have the following meanings: T_v [K] – temperature point corresponding to maximum crystallization rate, Vi [Ks^{-1}] – heating rate used to determine the DSC curve, R [Jmol^{-1} K^{-1}] – universal constant of gases, A – constant specific to analyzed material [137], [138].

Activation energy for crystallization of certain phase E_a could be determined based on eq. (1.8) as the slope of the line represented in following coordinates:

$$ln\left(\frac{T_v^2}{V_i}\right) = F\left(\frac{1}{T_V}\right) \qquad (1.9)$$

The amorphous nature of the cast ribbons was proved by both XRD and TEM. Figure 1.25 shows the HR-TEM image of as cast $Ti_{42}Zr_{40}Ta_3Si_{15}$ amorphous ribbons. The electron diffraction (SAED) pattern corresponding to the selected area is presented in the inset, right side of the picture. The HR-TEM micrographs shows only the random disordered distribution, which is typical to amorphous structure. The 2D SAED pattern presents also only the amorphous halo, as characteristic to the amorphous structure. Additionally, the XRD performed in Bragg-Brentano configuration did not evidenced any crystalline sharp reflection, as seen in Figure 1.23. Therefore, it can be concluded with no doubts that the cast $Ti_{42}Zr_{40}Ta_3Si_{15}$ ribbons are fully amorphous.

Figure 1.27 shows the DSC curve of amorphous melt-spun ribbons measured at a 20°Cmin^{-1} constant heating rate, in a slightly different representation in comparison with figure 1.26. Despite the fact that the $Ti_{42}Zr_{40}Ta_3Si_{15}$ ribbons were proved to be fully amorphous, the glass-transition event in the curve is quite weak. Often marginal glass formers do not exhibit a glass transition, at least at conventional heating rates as those used in this work [129]. In fact the first authors who studied this composition, H. Lin et al. [78], encountered serious difficulties in determining correctly the glass-transition temperature. In our case, as it is seen in Figure 1.27, a small but clear endothermic

event associated to the glass transition can be seen. This is in agreement with our previous findings [9]. The glass transition temperature, measured as the onset of this event, is T_g = 513°C. Further, the samples crystallizes through a single, sharp exothermic peak, heaving the onset at T_x = 616°C.

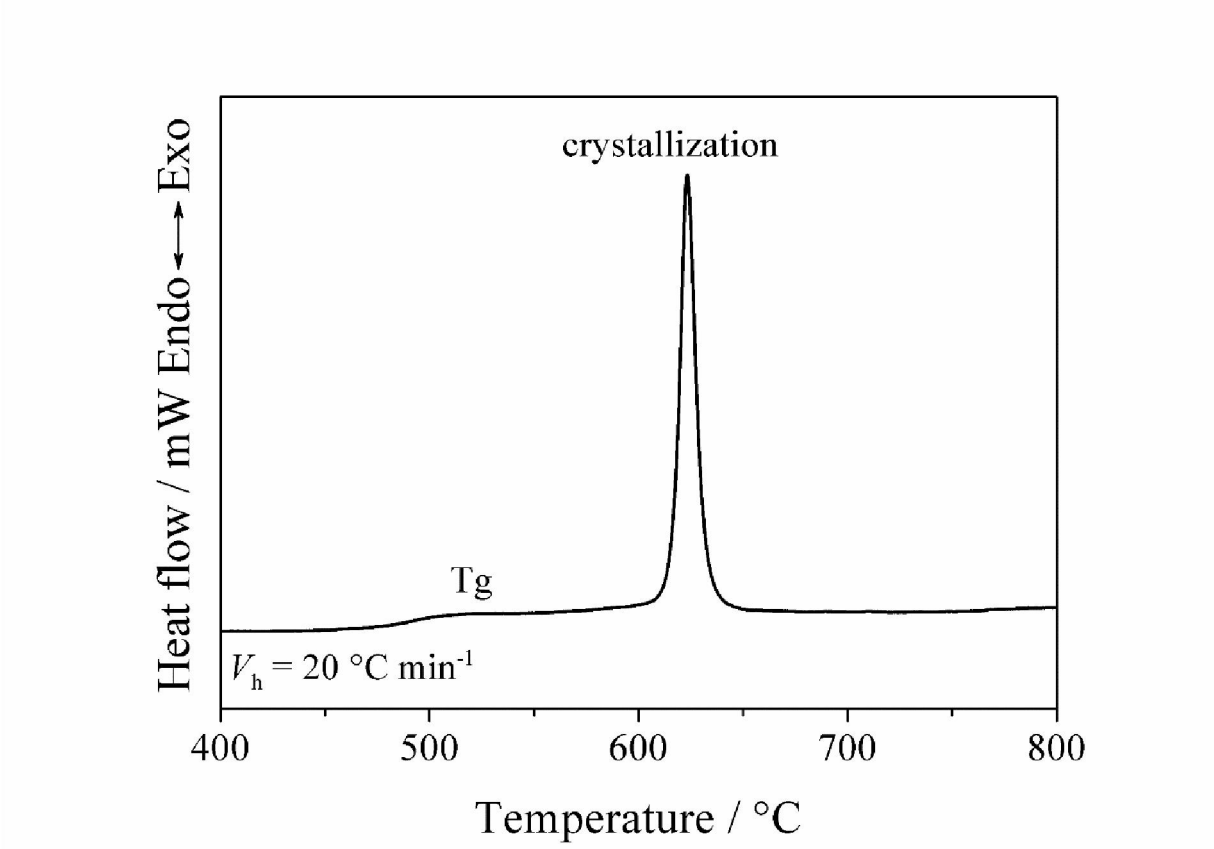

Figure 1.27. DSC curve for $Ti_{42}Zr_{40}Ta_3Si_{15}$ amorphous alloy ribbon measured at a constant heating rate of 20°Cmin^{-1} [10][39].

Evaluation of stability for amorphous structures is based on the activation energy necessary for crystallization, which is responsible for dramatic alteration of properties. Therefore, the DSC curves were also determined at different heating rates, i.e. 5, 10, 15 and 20°Cmin^{-1}. They are presented in Figure 1.28. The appearance of the endothermic event associated to the glass transition is even more faded when the heating rate for isochronal experiment decreases. This is obvious, because the slow heating allows structural relaxation prior crystallization. However, for further analyses the exothermic peak temperatures are of first importance.

The formation of crystalline entities usually proceeds with different rates, according to the reaction kinetics [129]. The transformation of the amorphous phase into crystalline phase takes place through nucleation and growth. Both events are temperature dependent, therefore the rates at which they proceed is easily determined upon isothermal experiments. However, in the case of isochronal DSC measurements, the maximum crystallization rate would correspond to the temperature of the exothermic peak, as marked at T_v in Figure 1.28. Table 1.8 summarizes the

[39] Reprinted with permission by Akadémiai Kiadó Zrt. Budapest, Hungary.

experimentally determined temperatures, which further allow the calculation of Kissinger plot as represented in Figure 1.29.

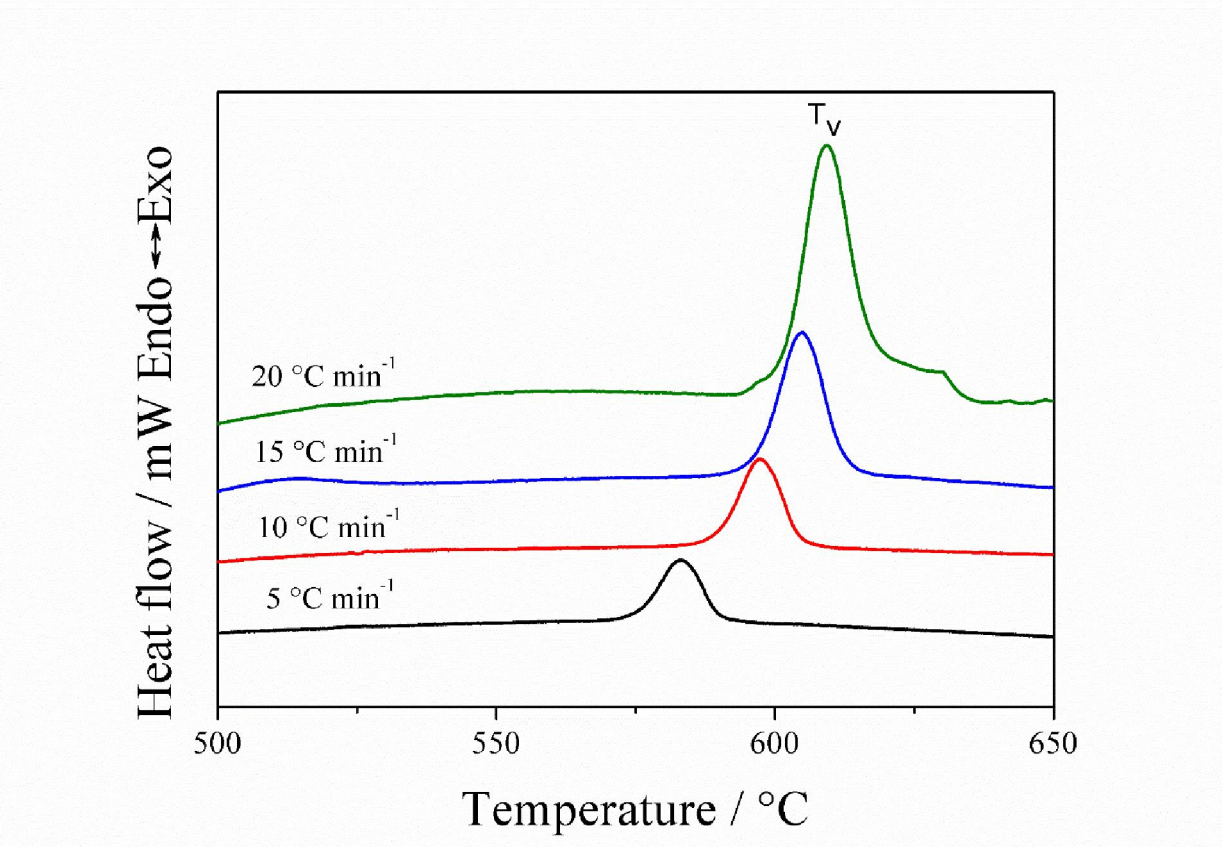

Figure 1.28. DSC curves measured at different heating rates. Peak temperatures T_v are considered further for Kissinger analysis [10][40].

Table 1.8. Parameters of DSC heating curves [10][39].

No.	Heating rate V_i/°Cmin^{-1}	Tip of the peak T_v/°C
1	5	583
2	10	597
3	15	605
4	20	609

The activation energy for crystallization of the $Ti_{42}Zr_{40}Ta_3Si_{15}$ amorphous alloy was determined based on representation in Figure 1.29, and is numerically equivalent to the slope of the line. The value is E_a = 310 kJmol^{-1}, and is comparable with activation energies determined for similar amorphous alloys. For example, the activation energy of amorphous $Ti_{40}Zr_{10}Cu_{36}Pd_{14}$, which is considered to have high thermal stability of crystallization, determined with Kissinger's method is 287.6 kJmol^{-1} [58].

Calculations of activation energies for crystallization of different amorphous Ti-based alloys have attracted considerable interest, since higher crystallization stability could facilitate conservation of amorphous character during subsequent thermal processing. Although the method based on Kissinger's plots, calculated from DSC

[40] Reprinted with permission by Akadémiai Kiadó Zrt. Budapest, Hungary.

curves that are obtained by isochronal heating at different rates, is considered less accurate, comparative studies on glassy Ti alloys reveal good agreement with isothermal investigations. For comparison, activation energy for crystallization of $Ti_{48}Ni_{32}Cu_8Si_8Sn_4$ BMG is 369.1 kJ/mol^{-1} for isochronal heating, calculated after Kissinger, and 381.8 kJ/mol^{-1} for isothermal annealing [139].

Non-isothermal methods are extensively used to determine the effect of different alloying elements on thermal stability to crystallization of amorphous alloys. For example, Pratap et al. [140] determined that partial replacement of Cu with Ni in Ti-based amorphous alloys was producing an increase of activation energy, calculated after Kissinger, from 207 kJ/mol^{-1} for $Ti_{50}Cu_{50}$ to 406 kJ/mol^{-1} in the case of $Ti_{50}Ni_{30}Cu_{20}$. It is worth noting that similar values of activation energies resulted by mean of Augis-Bennet or Ozawa methods of calculation. Similarly, the two crystallization reaction of $Ti_{20}Zr_{20}Cu_{60}$ metallic glass, calculated by Kissinger's method, have activation energies of 392 and 320 kJ/mol^{-1}, respectively, close to the values resulting from alternative methods (Augis-Bennet, Boswell, Ozawa, Gao-Wang) [141]. Other authors also emphasize that in the case of amorphous alloys, Kissinger's calculations are in good accordance with results obtained by other methods, such as Moynihan or Augis [142]. Another study [143] evidences that the amorphous $Ti_{41.5}Zr_{2.5}Hf_5Cu_{37.5}Ni_{7.5}$ Si_1 Sn_5 has an activation energy of crystallization of 409.51 kJ/mol^{-1} (after Kissinger), and therefore has a higher stability than the corresponding Sn-free alloy, with an activation energy of only 399.84 kJ/mol^{-1}. In the case of $Ti_{53}Cu_{27}Ni_{12}Zr_3Al_7Si_3B_1$ BMG, which evidences three distinct crystallization peaks on DSC curves, the activation energies calculated after Kissinger's are 377.86, 322.97 and 311.17 kJmol^{-1}, respectively, for the three resulting crystalline phases, although their compositions remain partially uncertain [144]. Additional alloying of the same BMG with small quantities of Sc, Hf, Ta and Nb results in activation energies for primary crystallization of 356.31, 355.02, 437.27, and 375.55 kJmol^{-1}, respectively, which emphasizes the stabilizing effect of Ta, which significantly increases the activation energy [145]. The effect of different alloying elements on the crystallization stability of Ti–Zr–Be bulk metallic glasses was evaluated also by mean of Kissinger's method. The activation energy for basic amorphous $Ti_{41}Zr_{25}Be_{34}$ is 181.3 kJmol^{-1}, which increases with addition of Cu, Al, Cr, V, and especially Ag that provides the highest activation energy of 242.5 kJmol^{-1}, while Fe, and Ni have the opposite effect. Crystallization of initial $Ti_{41}Zr_{25}Be_{34}$ alloy normally produces α-Ti_2Zr, Be_2Zr and α-Ti phases, but addition of elements like Fe, V, Cr results in formation of β-Ti, or some unknown phases when Cu and Ni are added [146]. Alloying the $Ti_{41}Zr_{25}Be_{28}Fe_6$ BMG with 7%at Cu also determines the growth of activation energy of crystallization, determined with the Kissinger method, for the first DSC crystallization peak, from 179 kJmol-1 to 188 kJmol^{-1}. The effect of Cu-alloying consists also in some modification of crystallization kinetics, since the isochronal DSC curve of the basic $Ti_{41}Zr_{25}Be_{28}Fe_6$ alloy has only two exothermic reactions of crystallization, while modified $(Ti_{41}Zr_{25}Be_{28}Fe_6)_{93}Cu_7$ has four such peaks. This effect is considered to reduce the nucleation and growth rate, making atomic diffusion more difficult and, therefore increasing the glass forming ability (GFA) [147].

The Kissinger's method is used also for comparative characterization of amorphous Ti-based powders produced by mechanical alloying from pure elements or mechanical milling of intermetallic compounds. For example, the activation energy for crystallization of $Ti_{60}Cu_{15}Ni_{15}Al_{10}$ amorphous powders is 260.5 kJ/mol^{-1} and 266.5 5 kJ/mol^{-1} if obtained by mean of mechanical alloying or mechanical milling, respectively [148]. In conclusion, activation energies for crystallization of amorphous $Ti_{42}Zr_{40}Ta_3Si_{15}$

is situated approximately in the same range with many Ti-based or Zr-based alloys [149], [150] that are considered highly stable against crystallization, but still lower than in the case of Fe-based amorphous alloys [151].

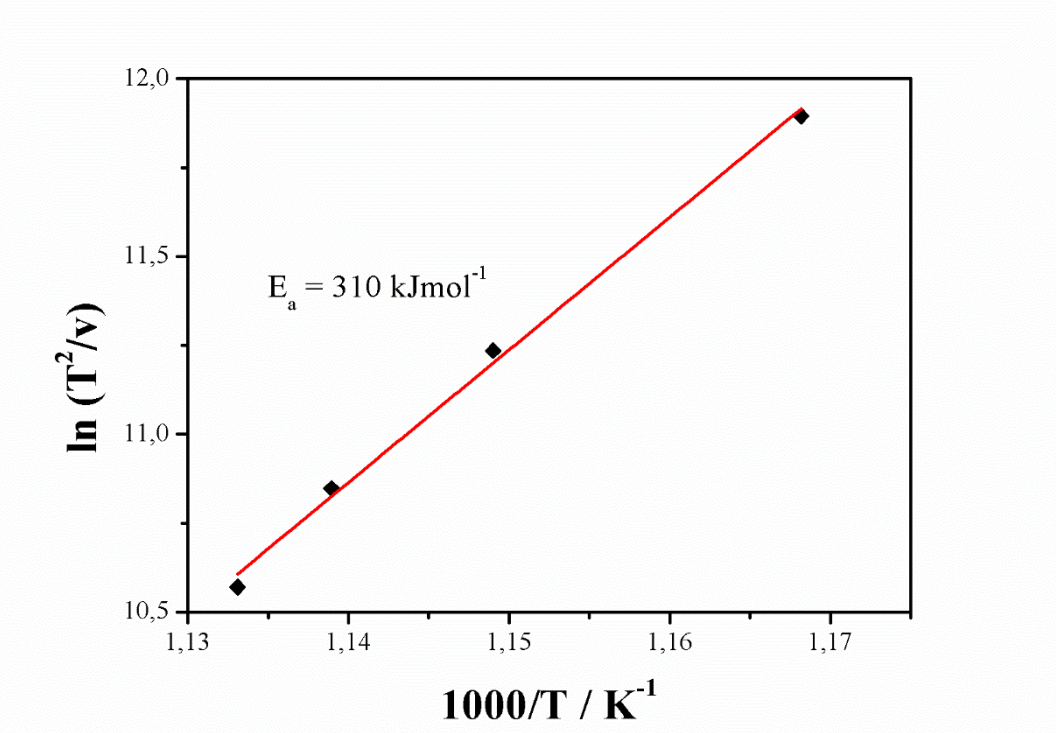

Figure 1.29. Kissinger's line of $Ti_{42}Zr_{40}Ta_3Si_{15}$ amorphous alloy [10][41] [42].

Information about the high activation energy of crystallization that was determined by mean of Kissinger's method for amorphous $Ti_{42}Zr_{40}Ta_3Si_{15}$ alloy should be corroborated with isothermal DSC investigations performed on the same alloy by Lin et al. [78]. They determined that incubation time during isothermal annealing range between 3000 s at 550°C and 1000 s at 580°. The combination of high activation energy and relatively long incubation time opens important perspective for subsequent processing of melt spun ribbons into massive components by mean of powder metallurgical routes, without affecting the amorphous character.

Regarding the thermal stability of the new alloy it may be concluded that despite a reduced glass-forming ability, the results clearly show the possibility to cast fully amorphous ribbons of $Ti_{42}Zr_{40}Ta_3Si_{15}$ alloy that have a high thermal stability. The calculated value of activation energy for crystallization is close to the typical values presented in literature for similar Ti-based alloys, and recommends this new alloy as suitable for processing by mean of powder metallurgy, without alterations of amorphous character or relevant properties. Considering the composition, which is completely free of any harmful elements, this new alloy has considerable potential as biomaterial for applications as orthopedic or dental implants.

[41] The author of this thesis is grateful to A. Raduta, co-author of [10] [11] for consistent help in application of Kissinger's method.
[42] Reprinted with permission from Akadémiai Kiadó Zrt. Budapest, Hungary.

2.5. Mechanical properties of the new porous BMG

Since the mechanical properties of the resulting porous alloy are of utmost importance for their biomechanical performance, room temperature compression tests were performed on an INSTRON 8562 electromechanical device coupled with a laser extensometer. The tests were performed on 3x3x6 mm^3 block-shaped specimens under quasistatic loading in track-control mode (displacement speed 10^{-3} mm/s). The samples used for the mechanical tests were cut perpendicular to the pellet faces (i.e. along the main axis of the cylinder) and carefully polished plan-parallel.

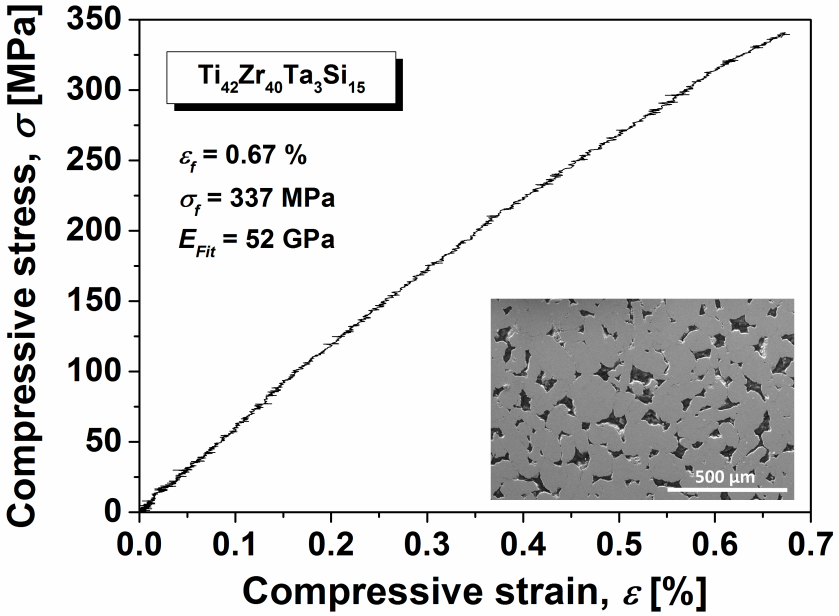

Figure 1.30. Compressive stress-strain curve measured for a 3 mm x 3 mm x 6 mm parallelepiped cut from a $Ti_{42}Zr_{40}Ta_3Si_{15}$ glassy alloy pellet. The inset (SEM micrograph) shows the morphology of the investigated samples [9][43] [44].

A typical stress– strain curve is presented in Figure 1.30. Additionally, the inset (SEM micrograph, SE mode) shows the morphology of the investigated sample. The global behavior is characteristic of a brittle material. However, the curve changes its slope continuously. This could be interpreted as a tendency towards plastic deformation. The continuous change in slope may be also amplified by a further, purely mechanical consolidation, triggered by the high loads used in compression test. Also, by a slight deviation from the parallelism of all faces of the cut and polished sample. Despite the fact that these two aspects cannot be ruled out, the change in slope is anyway very small and the stress-strain curve can be approximated as linear with no substantial errors.

There is no obvious yield point and the fracture occurred at 337 MPa at a strain of 0.67 %. The linear fitting of the entire curve gives a Young's modulus of 52 GPa. It should be mentioned that these are *apparent* values, which characterize the porous structure and not the material itself. For this kind of alloy, a typical value for Young's modulus is somewhere in the range of 80-90 GPa [152] [153].

[43] Special thanks to R. Parthiban, co-author of [8], [9] for consistent help in performing of material testing.
[44] Reprinted with permission by Elsevier.

As already mentioned, the bone is essentially a hierarchical composite, therefore it is *anisotropic*. In turn, the $Ti_{42}Zr_{40}Ta_3Si_{15}$ glassy alloy pellets should behave *isotropic*, because the compacted milled ribbon fragments are randomly oriented and no texture is induced during hot compression. The mechanical properties of the bone are given in Table 3 [128]. Besides the very low Young's modulus, the bone fractures in compression at a maximum stress of 205 ± 17.3 MPa, while the $Ti_{42}Zr_{40}Ta_3Si_{15}$ glassy alloy pellets can withstand 337 MPa. Most probably the $Ti_{42}Zr_{40}Ta_3Si_{15}$ bulk metallic glass compacts behaves brittle in tension as well, but certainly the ultimate stress level is comparable with that measured in compression, as it is generally the case for metallic glasses [31] [119].

Table 3 Anisotropic elastic properties of human femoral cortical bone and the anisotropic and asymmetrical ultimate stresses of human femoral cortical bone. In parenthesis the standard deviations are given (data taken from Ref. [128]).

	Modulus [GPa]	**Poisson's ratio**	**Ultimate stress tension [MPa]**	**Ultimate stress compression [MPa]**
Longitudinal	17.9 (3.9)	0.40 (0.16)	135 (15.6)	205 (17.3)
Transverse	10.1 (2.4)	0.62 (0.26)	53 (10.7)	131 (20.7)
Shear	3.3 (0.4)	---	65 (4.0)	

Comparatively smaller differences in modulus and strength have been reported between the radial and circumferential directions, indicating that human cortical bone may be treated as *transversely isotropic*. Cortical bone is also stronger in compression than in tension (Table 3). The strength-to-modulus ratio for cortical bone is about 1.14 and 0.75 for longitudinal compression and tension, respectively. Compared with high-performance metallic engineering alloys such as aluminum 6061-T6 and Ti-6Al-4V with corresponding ratios of about 0.45 and 0.73, respectively [128] it is seen that cortical bone has a relatively large strength-to-modulus ratio. In this sense, it can be considered as a relatively high-performance material, particularly for compression. With the data presented in Fig. 8, the $Ti_{42}Zr_{40}Ta_3Si_{15}$ glassy alloy pellets show in compression a strength-to-modulus ration of almost 0.65, comparable with the other typical alloys, but there are no toxic elements like V or Al. Moreover, even if brittle, an implant based of $Ti_{42}Zr_{40}Ta_3Si_{15}$ glassy alloy compacts would mechanically fail at loads at which the surrounding bone has already fractured.

The typical stress-strain behavior for human cortical bone exhibits 1…1.5 % plastic deformation [128]. The bone is stiffer in the longitudinal direction, indicative of its elastic anisotropy. It is also stronger in compression than in tension, indicative of its strength asymmetry (as can be seen also from the data presented in Table 3). While it is often appropriate to assume average properties for cortical bone, as shown in Table 3, it may be necessary in some cases to account for the heterogeneity that can arise from variations in microstructural parameters such as porosity and percentage of mineralization. Both modulus and ultimate stress can drop to half of their values when the porosity is increased from 5 to 30 percent [128]. Small increases in the amount of mineralization cause large increases in both modulus and strength, and while this parameter does not vary much in adult humans, it can vary substantially across species [128].

2.6. Biocompatibility of the $Ti_{42}Zr_{40}Ta_3Si_{15}$ alloy

Although the alloy contains only biocompatible elements, comprehensive *in-vitro* and *in-vivo* investigations are envisaged for the future. However, some preliminary corrosion tests were performed using simulated body fluid (SBF).

Due to the fact that on the compacted pellets and/or the powder grains might be difficult to detect the modifications provoked by the liquid (because of the geometrical irregularities of the grains), the chosen samples were small fragments of ribbons. However, as it will be shown in next sections, the amorphous nature of the samples at all stages (i.e. ribbon, milled powder and compacted pellets) was preserved, therefore it is not wrong to assume that the (bio)chemical behavior of the starting ribbons is identical with that of the final product. The samples were visualized by SEM (SE mode) before and after test. In order to asses as accurate as possible the modifications, we tried to record the before-and-after micrographs in the same place of the sample. Also, the appearance of both sides of the ribbons were investigated. It is known that the two sides of such melt-spun ribbons show different morphologies. The surface in contact with the Cu-wheel is much rough than the free-solidified surface, in principal because of the contact between the molten alloy and the wheel. Also, typical gas-pockets may form, due to the gas trapped between wheel and molten alloy bath during rapid solidification. Therefore, the free solidified surface is shiny and almost featureless, while the wheel side is matt.

Fragments of amorphous ribbons were immersed for 7 days in Kokubo solution at 36.5°C [154] [155] and, in order to determine as accurate as possible the subsequent modifications, both shining and matt surfaces were observed by mean of SEM, before and after test. For comparison, fragments of crystallized ribbons were as well tested and analyzed in the same conditions.

Figures 1.31, 1.32 and 1.33 summarize the results. The 1.31 (a), 1.32 (a), and 1.33 (a), SEM micrographs present the appearance of different ribbon specimens before immersing in SBF, while the 1.31 (b), 1.32 (b), and 1.33 (b) the appearance of the same samples after 7 days of immersion. Figures 1.31 (a) and (b) show the appearance of the free (shinny) side. It can be seen that the featureless surface of the as-spun ribbon is preserved after one week immersion in the SBF. However, some small traces may be observed on the surface (Figure. 1.31 (b)), but it is not clear if they are real chemical attacks or artefacts stemming from the sample itself. The few observable (darker contrast) parallel lines are along the ribbon direction, hence there geometric imperfection might still be present. In turn, the BSE mode of the SEM (i.e. contrast upon composition) did not show visible differences, so this surface is characterized by compositional uniformity. More clearly are the micrographs presented in Figures 1.32 (a) and (b), taken from the matt surface. Due to the higher roughness and in order to have a better view, the pictures were recorded at lower magnification as in the case of bright side. There, by analyzing matching geometrical features present in both 1.32 (a) and (b) micrographs (not specially marked here because the pictures are very similar and the reader can freely choose any feature to follow), one can clearly see that the ribbon was not visible affected by the immersion in the SBF.

The resistance against corrosion in SBF may be due not only to the chemical elements, but also to the amorphous nature of the ribbons. For comparison, Figures 1.33 (a) and (b) show the appearance of a crystallized ribbon, before and after immersing 7 days in SBF. For complete crystallization, the ribbons were kept for 1 hour at 973 K. As it was shown before, by heating at this temperature the amorphous samples crystallize completely.

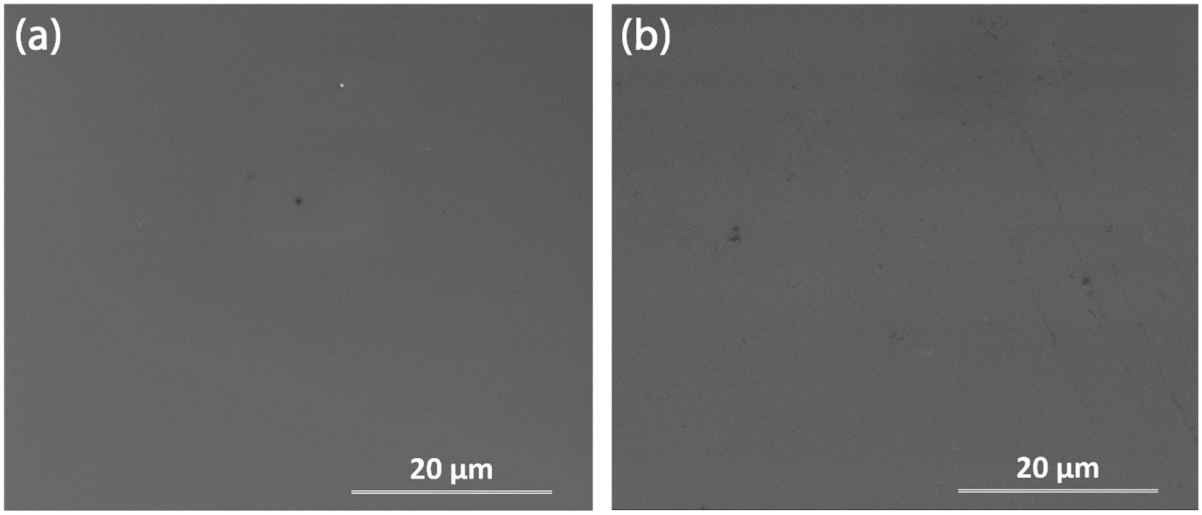

Figure 1.31. Appearance of ribbon samples on the free side of the ribbon: (a) before, and (b) after immersion for 7 days at 36.5 °C in SBF (SEM image, SE mode) [9][45].

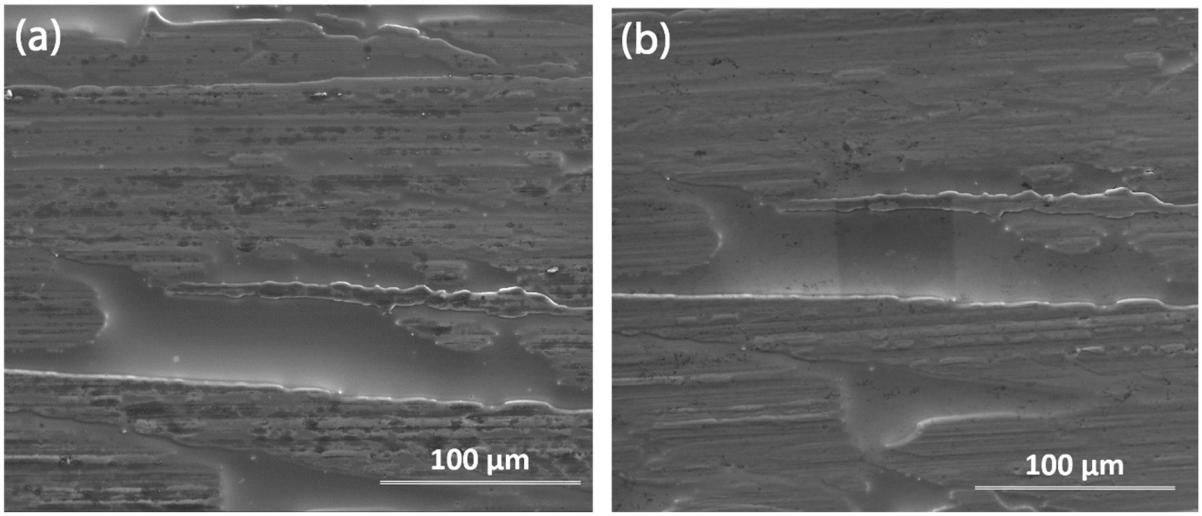

Figure 1.32. Appearance of ribbon on the wheel side of the ribbon: (a) before, and (b) after immersion for 7 days at 36.5 °C in SBF (SEM image, SE mode) [9][45].

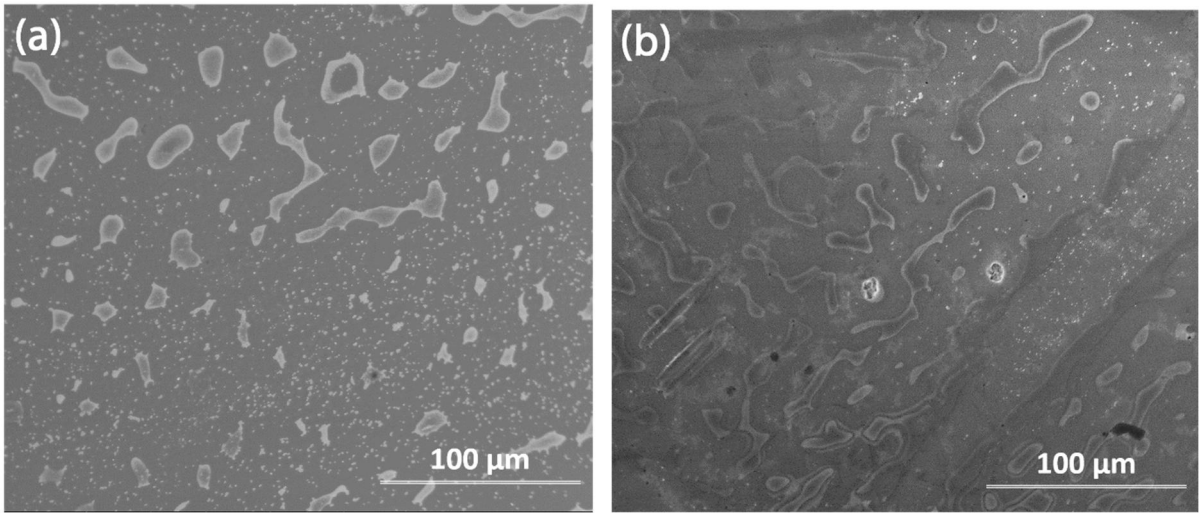

Figure 1.33. Appearance of crystallized ribbon samples: (a) before, and (b) after immersion for 7 days at 36.5 °C in SBF (SEM image, SE mode) [9][45].

[45] Reprinted with permission by Elsevier.

The micrographs clearly show the crystalline entities and, after immersion, one can observe traces of pitting corrosion. However, the magnification is still coarse and further investigations are necessary. Hence, in order to conclude about biocompatibility of the samples, further *in-vitro* and *in-vivo* tests are necessary and currently under consideration.

2.7. Conclusions

A new, porous bulk glassy $Ti_{42}Zr_{40}Ta_3Si_{15}$ alloy was developed and characterized. The samples were prepared by hot compaction of cryo-milled melt-spun ribbons. XRD, HR-TEM and DSC investigations proved that the samples were amorphous at every stage of preparation. However, small nanocrystals may form in the final product upon hot pressing. The carbon contamination of the ribbons due to the use of graphite crucibles upon melt-spinning eventually assist the formation of some carbides, if the ribbon is kept long enough at high temperatures.

The morphology of the compacted pellets is by some means close to that seen in cortical bone and most probably can be further tuned by refining the preparation parameters. Preliminary corrosion tests in simulated body fluid did not show substantial modifications on the melt-spun ribbons.

The mechanical properties, which are very close to that of the bone, together with the absence of any harmful elements in the composition, make the new porous bulk glassy $Ti_{42}Zr_{40}Ta_3Si_{15}$ alloy suitable for applications as biocompatible structural material.

The new alloy has a relatively high activation energy and long incubation time, which allow interesting perspectives for development of new processing routes based on powder metallurgy techniques to transform the amorphous melt spun ribbons into massive components, with amorphous or composite amorphous/nano-crystalline character.

Chapter 3. Advanced Al-based hybrid composites

3.1. Basic concept

As stated in the *Introduction* to present thesis, DRAMCs still have significant potential for engineering applications because they combine low specific weight with enhanced mechanical properties [17], [21]. Reinforcement particles are still subject to intensive researches based on their well-documented effect on improving stiffness and mechanical strength, fatigue and wear behavior, and also on significantly decreasing thermal expansion of resulting material [156] [157], [158].

From the technological point of view, powder metallurgy tends to impose itself as the main fabrication method for aluminum matrix composites, because its flexibility and potential for higher microstructural quality of materials, but some technological problems still persists, which impede large scale applications [159].

Development of a new class of Al-based MMCs is proposed based on this actualities. The following modern concepts have been used as foundation for the researches:

- Composites are of hybrid-type, i.e. they have two reinforcements. Synthetic alumina (Al_2O_3) is embedded via a classical PM technique to provide basic reinforcement at a level considered to be acceptable to avoid fragility (20%vol.).
- An additional reinforcement is produced *in-situ* as secondary alumina by mean of reactive sintering, as reaction between iron oxide (Fe_2O_3) and Al matrix.

3.2. Hybrid Al-composites by fabricated by mean of reactive sintering

The main difficulty in augmentation of mechanical of Al-based composites consists in providing higher particle reinforcement. Ceramic and metallic powders are difficult to mix uniformly, because metallic particles usually have larger diameters [160]. Therefore ceramic particles tend to agglomerate, especially for more than 15- 20 % vol. of reinforcement, and final microstructure is characterized by clusters, or even networks of ceramic particles, which could produce extreme fragility. Rearrangement of ceramic particles is difficult to achieve, requiring additional hot deformations. Some ceramic reinforcements could also have poor bonding with matrix, and therefore load transfer is reduced, affecting mechanical properties [161] [162].

Alternative fabrication based on *in-situ* methods, using chemical or structural reactions inside metallic matrix, show interesting perspectives, because matrix and reinforcement have interfacial compatibility and good bonding. Uniform distribution could also be achieved, but the main inconvenience is that proportion of reinforcement could be too low for significant gain in mechanical properties [23], [163], [164], [165], [166].

Combining both *in-situ* and *ex-situ* fabrication concepts could result in the production of composites, which have two different fractions of reinforcement. For the present experimental program, basic reinforcement of 20% vol. was provided *ex-situ* by mixing high purity alumina and aluminum powders. Supplementary reinforcement was achieved by adding 7.5 % vol. of Fe_2O_3 powder, which was transformed into alumina particles, as result of *in situ* reaction with aluminum [167]:

$$Al + Fe_2O_3 \rightarrow Al_2O_3 + 2Fe + \sim 850kJ \qquad (3.1)$$

Secondary alumina produced *in-situ* is meant to increase the proportion of reinforcement above 20% vol., while resulting iron atoms combine to form different intermetallic phases. Kinetics of Al- Fe_2O_3 thermite reaction for fabrication of in-situ composites have been studied extensively, which reveal that many internal and external factors could affect the rather complicated mechanisms of reactions [167], [168], [169], [170]. Therefore, the present research include differential scanning calorimetry (DSC) investigations to determine the kinetics of *in-situ* reactions during production of secondary alumina. The ultimate aim is optimization of reactive sintering treatment for final consolidation of powders [13].

3.2.1. Experimental materials and investigations

The blend of powders used for fabrication of composite material contained 3 different grades provided by Alfa Aesar: 7.5 % vol. iron (III) oxide (Fe_2O_3, purity >99.94 % wt., particle size <5 μm), 20 % vol. alumina (Al_2O_3, purity >99.99% wt., predominantly α-phase, 10-20% γ-phase, particle size <0.3 μm) and commercially pure aluminum (purity >99.5 % wt., particle size <44 μm) up to balance.

The powders were blended in a planetary mill (Retsch PM400) under argon atmosphere, using hardened steel balls and vials at 300 rpm, for a total time of 12 hours, every 5 minutes of milling alternating with 5 minutes of pause, in order to avoid excessive heating. The ball-to-powder weight ratio was about 10:1 and 0.8–1wt% stearic acid was used as a process control agent (PCA) material. All powder handling was carried out in a glove box under purified argon atmosphere (less than 0.1 ppm O_2 and H_2O).

Hot pressing of powder blend was performed at 550°C, under a pressure of about 900 MPa, which was applied for 10 min to fabricate small disks, 10 mm in diameter and about 3 mm thick. The pressing was performed in a double action pressing die, heated by induction. The Huttinger/Weber-Pressen type pressing machine had an automatic hydraulic system that allowed continuous pressure control. Hot pressing was carried after vacuum-degassing under argon gas protection.

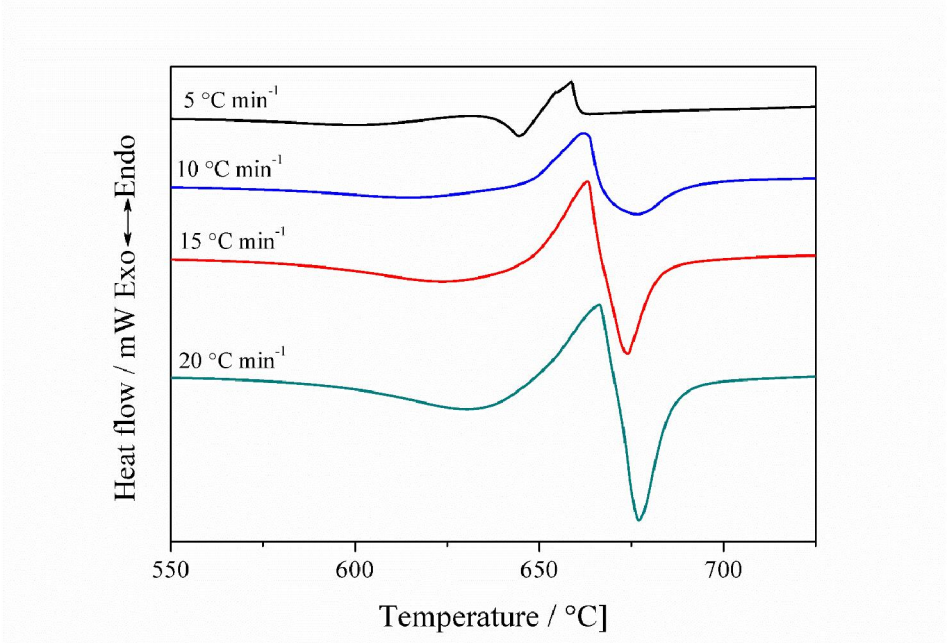

Figure 3.1. DSC curves at different heating rates [13][46].

[46] Reprinted with permission by Akadémiai Kiadó Zrt. Budapest, Hungary.

Isochronal differential scanning calorimetry (DSC) investigations were performed under argon gas on a Netzsch STA 449F1 calorimeter in order to determine transformation points and calculate activation energies of thermal reactions occurring during heating, and further optimization of sintering parameters, i.e. processing temperature and duration. Samples of hot-pressed powders were heated at different rates, i.e. 5, 10, 15 and 20° min^{-1}. All samples had a mass of approximately 40 mg, same as the alumina reference material. Standard Al_2O_3 DSC/TG pans with lids were used, and all heating operations were performed using high-purity argon gas. Resulting DSC curves around the theoretical melting point of aluminum are presented by figure 3.1.

Analysis of curves in figure 3.1 evidences the complex nature of possible thermal reactions:

- Endothermic melting of aluminum, which could be identified as the peak around the theoretical point of 660°C;
- Some exothermic effects, which partially superpose the aluminum melting.

So far researches have been focused mostly on thermite reaction between aluminum and iron above 900°C, and therefore exothermic reactions below 700°C are usually neglected [167], [168], [169], [171], although they obviously appear on some DSC curves. However some authors reported these exothermic reactions at moderate temperatures, especially in context with fabrication of intermetallic materials from elemental Al-Fe powders, and putted them in relation with formation of Fe-Al solid solutions or intermetallic phases, such as $FeAl_3$, $FeAl_2$, Fe_2Al_5, Fe_3Al or FeAl [170], [172], [173], [174], [175], [176], [177].

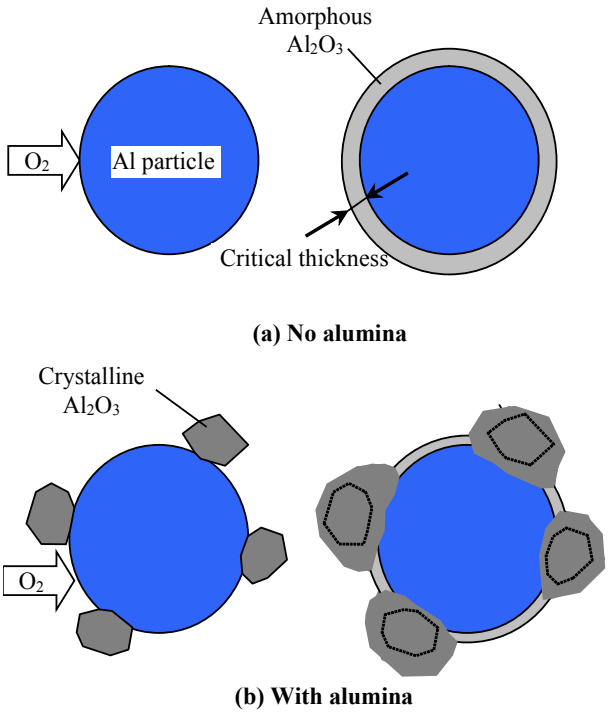

Figure 3.2. Oxidation process of aluminum particles. (a) no presence of alumina particles; (b) germinating effect of alumina particles [13][47].

[47] Reprinted with permission by Akadémiai Kiadó Zrt. Budapest, Hungary.

Exothermic reactions were also connected by some authors with some complex oxidation phenomena [178], [179], [180], initiated below the melting temperature of Al. It may be considered that at relatively low temperatures (T<300°C), an initial thin layer of amorphous alumina forms on surface of aluminum particles, having a lower (non-stoichiometric) concentration of Al. Eventually the processes is slowing down and even stops, when the amorphous oxide layer reaches a critical thickness (0.5 – 4 nm), that is able to temporarily block oxygen access. As temperature increases, the amorphous layer crystallizes (T>300°C), which creates new diffusion paths for oxygen through a network of grain boundaries, inside the new crystalline layer. The presence of some small alumina particles changes the kinetics of reaction, since they could more easily germinate the transformation of amorphous alumina in more stable crystalline phases [178], [181], [182], [183], [180]. Therefore, oxidation of aluminum and transformation to crystalline alumina could be more intense when fine alumina particles are added as germination "seeds" [181], which is actually the case of Al-based composites that contain *ex-situ* Al_2O_3 particles (figure 3.2). Consequently, an almost complete decomposition of Fe_2O_3 and formation of *in-situ* alumina could be possible at moderate temperatures, around melting point of Al.

Table 3.1. EDX compositions of characteristic areas of composite [13][48].

CHARACTERISTIC AREA	CHEMICAL ELEMENTS					
	Aluminum		Iron		Oxygen	
	Mass %	At. %	Mass %	At. %	Mass %	At. %
WHITE	84.97	92.13	15.03	7.87	-	-
DARK GREY	72.62	61.85	1.15	0.47	26.23	37.68
BLACK	100	100	0	0	0	0

In order to confirm the hypothesis of iron oxide decomposition, hot pressed samples of composite material were sintered for 1 hours at 700°C and subsequently investigated by mean of quantitative scanning electron microscopy (SEM), using a FEI Quanta 250 FEG scanning electronic microscope equipped with an EDAX SDD Apollo X sensor. Microstructure after reactive sintering is presented in figure 3.3, and table 3.1 gives the compositions determined by mean energy of dispersive X-ray spectroscopy (EDX) of all the three characteristic constituents that could be evidenced on SEM images.

White constituents in figure 3.3 seem to contain only aluminum and iron atoms, with no traces of oxygen and only low proportion of iron (approximately 8% at.), and therefore could be identified more likely as solid solution of iron in aluminum, or other metastable Al-Fe phases, with low content of Fe.

Grey areas in SEM image contain almost exclusively aluminum and oxygen atoms, with practically no iron (less than 0.5 % at.). Since aluminum has almost twice the atomic proportion of oxygen, it may be consider that these areas contain aluminum and alumina. Because atomic oxygen was not evidenced in any other zone, both ex-situ and in-situ alumina should coexist within this grey area, which has a heterogeneous nature.

Black area contain exclusively aluminum and represent the consolidated aluminum matrix of composite, resulting from initial aluminum particles. Remarkably,

[48] Reprinted with permission by Akadémiai Kiadó Zrt. Budapest, Hungary.

oxygen and iron do not coexist in any areas of the composite, and therefore complete decomposition of iron oxide could be presumed.

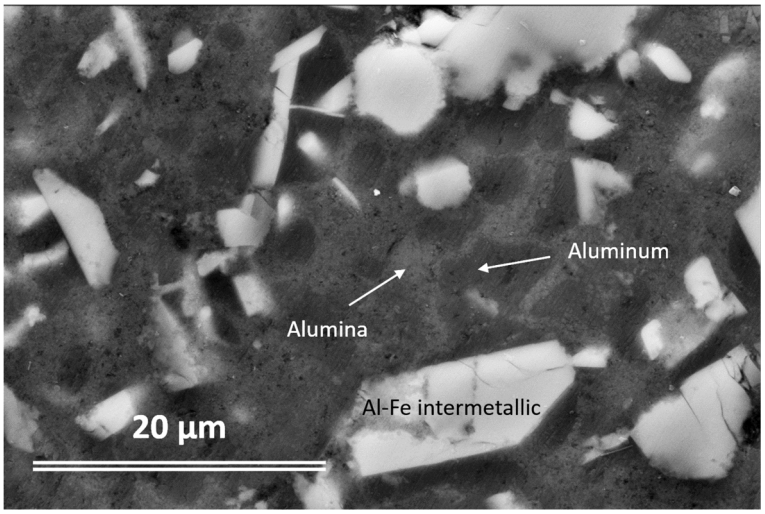

Figure 3.3. SEM microstructure of Al-Al_2O_3 composite after reactive sintering at 700°C/1 hour [13][49].

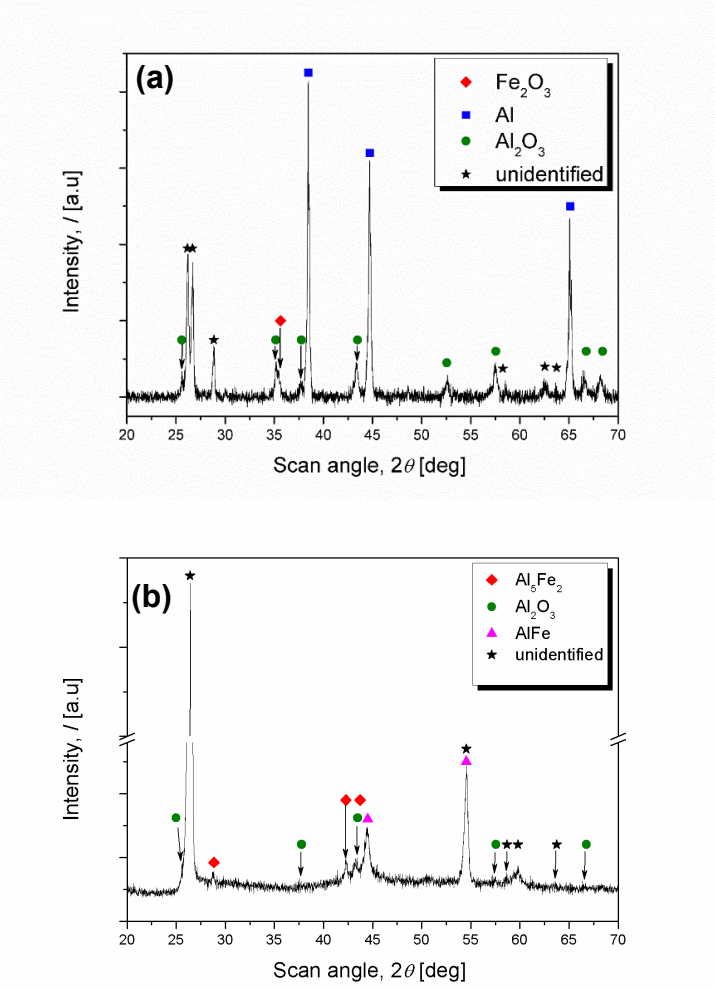

Figure 3.4. XRD patterns of composite samples: (a) hot pressed preforms; (b) sintered 700°C/1 hour [13][49].

[49] Reprinted with permission by Akadémiai Kiadó Zrt. Budapest, Hungary.

Investigations of X-rays diffraction (XRD) were performed on both hot pressed preforms and samples sintered at 700°C for 2 hours, using a FEI X'Pert PRO MPD diffractometer with a copper anode X-ray tube (λ = 0.0155 nm), PixCEL detector, vertical $\theta - \theta$ goniometer and spinning sample holder. Resulting XRD patterns that are presented by figure 3.4, reveal the complex nature of transformations that occur during fabrication route. The normal sequence of transformations reported for reaction between Al and Fe is Al (Fe) solid solution, $FeAl_3$, Fe_2Al_5, $FeAl_2$ and finally the FeAl [176], but many other metastable phases had been reported [184], [185], [186], and interaction with thermite reaction could complicate even more the kinetic of transformations.

In this particular case, it seems that hot pressing at 550°C for 10 minutes probably does not produce complete decomposition of iron oxide, but still cause formation of some complex metastable phases that could not be positively identified at this stage. The XRD patterns are more dispersed after reactive sintering at 700°C, and peaks of Al_2O_3 are attenuated, which could indicate formation of metastable phases. Some small peaks could be assigned to Al_5Fe_2, which formation was reported by some authors to occur between 650 and 700°C [175], however, the analysis of XRD curve by mean of X'Pert HighScore Plus software reveals that other intermetallic phases, such as $Al_{86}Fe_{14}$, $Al_{82}Fe_{18}$, $Al_{75}Fe_{25}$, etc., have similar patterns in the range $2\theta = 40..45°$. Some diffraction peaks also indicate the possible presence of AlFe, but also formation of some unidentified phases. All these considerations still leave open the question for reasons that produce the exothermic reactions detected during composite fabrication. Surprisingly, no Al peaks were evidenced on sintered samples, although EDX results indicated that areas composed exclusively by Al still exists, which could suggest that some of unidentified peaks could be related not only to some metastable phases, but also with the distorted crystalline structure of Al matrix, which may altered the Al XRD pattern.

Further sintering experiments, as well as investigations by mean of transmission electron microscopy (TEM) are envisaged in the future to determine the nature of newly formed microstructural constituents.

3.2.2. Optimization of sintering parameters

In order to interpret the results of DSC investigations, the experimental data were subjected to further analysis, on the hypothesis that recorded DSC data had been the result of a linear combination of different thermal reactions, i.e. endothermic melting of aluminum and other exothermic effects.

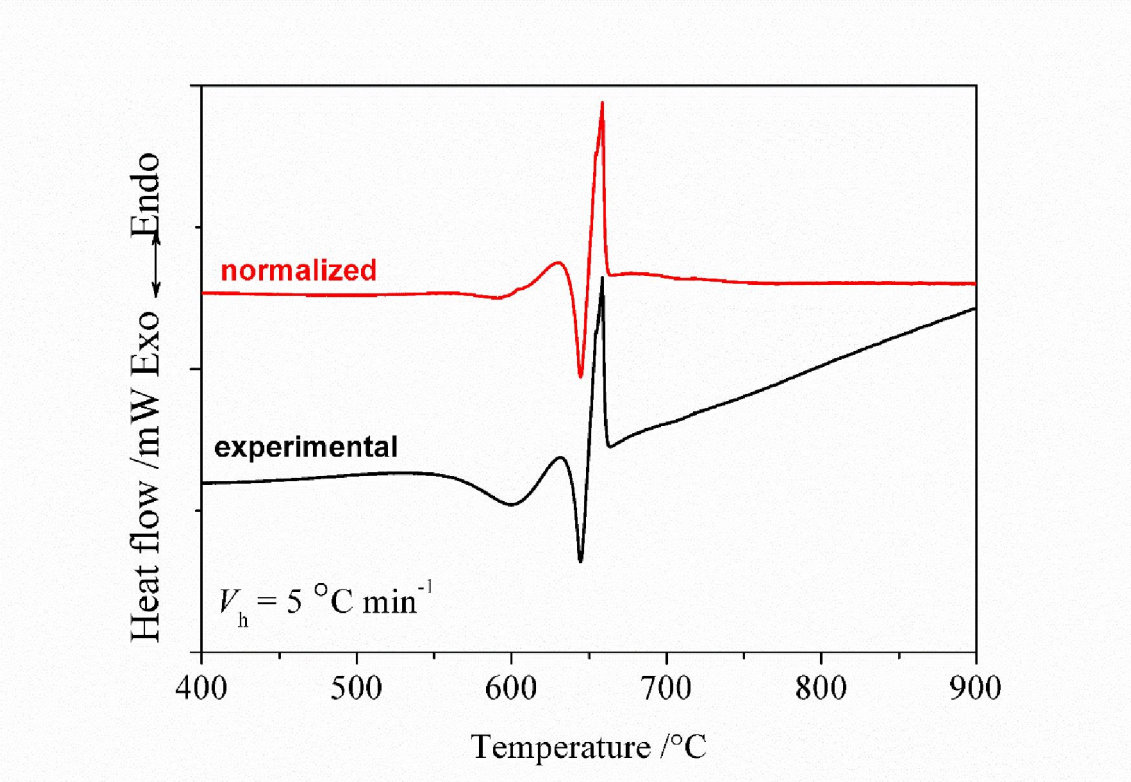

Figure 3.5. Normalization of DSC experimental data for the 5°C min^{-1} heating rate [13][50] [51].

The first step in data manipulation was normalization of the DSC curves in order to eliminate the possible differences of specific heat between sample and reference, which induced curve slopes. This procedure proved to be useful for consistency in subsequent calculations. Figure 3.5 illustrates the effect of normalizing the experimental DSC curve for the heating rate of 5°C min^{-1}.

Endothermic and exothermic peaks were detected using the first derivative method, in order to optimize the data fitting. Deconvolution process began with the endothermic peak, which obviously corresponded to aluminum melting. Subsequently the input data were processed starting near previously detected peak. The result consisted in three individual peaks, from which two were exothermic and one was endothermic. Resulting exothermic peaks could be attributed to formation of new intermetallic phases and processes of aluminum oxidation. All resulting peaks were fitted using general Gaussian model, equation (3.2):

$$f(T) = a_i e^{-\left(\frac{T-b_i}{c_i}\right)^2} \qquad (3.2)$$

[50] Special thanks to C. Locovei, co-author of [13] for consistent help in mathematical processing of DSC curves.
[51] Reprinted with permission by Akadémiai Kiadó Zrt. Budapest, Hungary.

Where a_i, b_i and c_i were the height of the peak, the center of the peak and the standard deviation, respectively. Peak detection and fitting were performed using commercially available software. Figure 3.6 exemplifies the calculated curves for the endothermic reaction and two distinct exothermic reactions, as well as the combination of them resulting by summarization, for the heating rate of 5 °C min^{-1}.

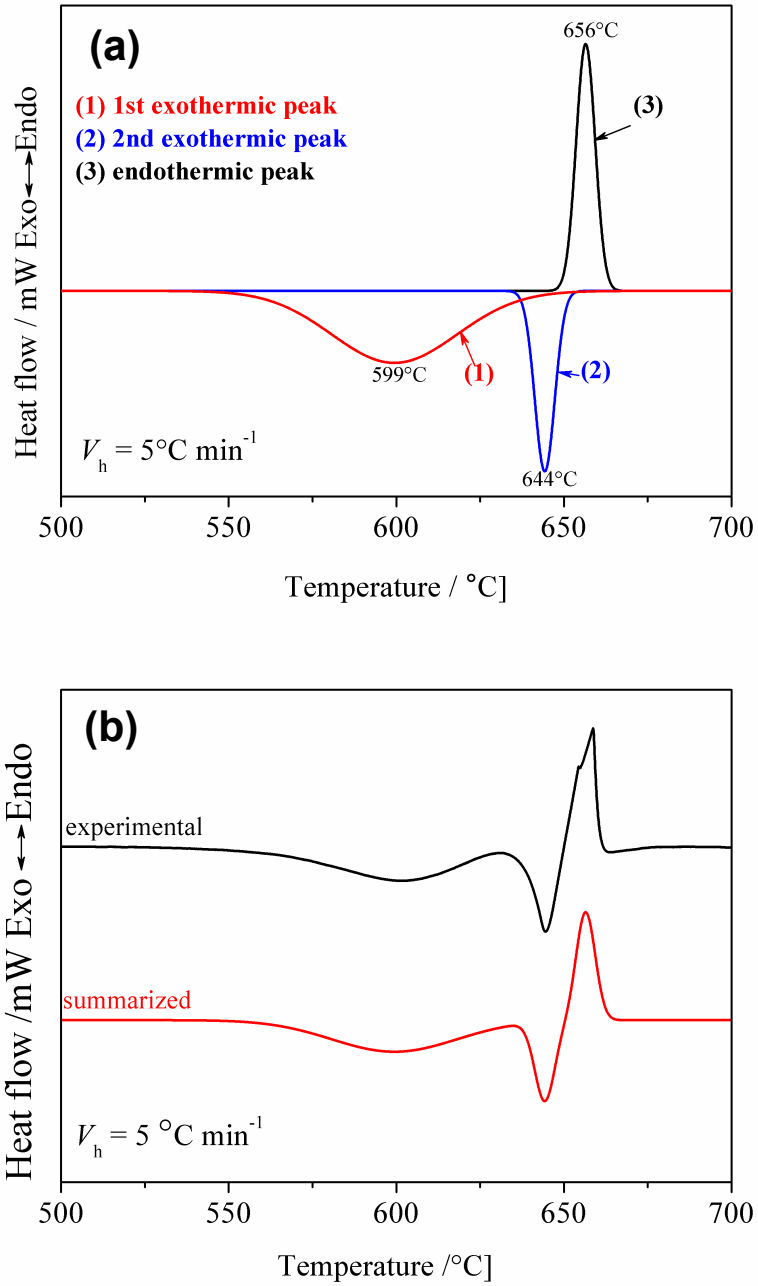

Figure 3.6. Resulting peaks for deconvolution of 5°C min^{-1} DSC curve: (a) calculated peaks; (b) comparison between the experimental curve and the calculated curve resulting as sum of the 3 deconvoluted peaks [13][52].

Calculated coordinates of the peaks for all heating rates (5, 10, 15 and 20°C min^{-1}), with 95% confidence interval are presented in Table 3.2.

[52] Reprinted with permission by Akadémiai Kiadó Zrt. Budapest, Hungary.

Table 3.2. Gaussian coefficients (with 95% confidence bounds) for the fitting of experimental DSC curve [13][53].

DSC Experiment	Coefficient	Exothermic Peak 1	Exothermic Peak 2
5°C min^{-1}	a_1 /mW mg^{-1}	-7.19±0.06	-2.86±0.02
	b_1 /°C	599.44±0.14	644.29±0.02
	c_1 /°C	37.31±0.32	5.93±0.05
10 C min^{-1}	a_2 /mW mg^{-1}	-11.49±0.13	-15.20±0.60
	b_2 /°C	609.52±0.19	672.86±0.38
	c_2 /°C	41.19±0.44	18.04±0.41
15 C min^{-1}	a_3 /mW mg^{-1}	-14.44±0.13	-35.38±3.88
	b_3 /°C	619.55±0.14	671.99±0.09
	c_3 /°C	33.63±0.33	10.58±0.19
20 C min^{-1}	a_4 /mW mg^{-1}	-22.48±0.24	-38.03±1.18
	b_4 /°C	625.85±0.25	676.87±0.03
	c_4 /°C	35.21±0.41	9.77±0.09

Resulting values suggest that endothermic peak, as expected, is close to the theoretical melting point of aluminum (660°C). The exothermic effects could be the result of several concurrent phenomena, such as formation of new Al-Fe compounds [173], and oxidation processes [178], both of them implying in this particular case decomposition of Fe_2O_3, and formation of additional quantities of alumina, since no flux of oxygen atoms may be available from the exterior. However, two separate exothermic reactions were determined, one of them more or less superposed to aluminum melting, the other one at much lower temperatures. Considering the relatively high energy of the exothermic effects, evidenced on deconvoluted curves, it could be expected that decomposition of the small addition of iron oxide (7.5 % vol.) may be achieved even at relatively moderate temperatures, around 700°C.

The energy needed for activation of exothermic reactions is generally calculated based on DSC curves using the Johnson-Mehl-Avrami (JMA) equation and Kissinger's method, which are consecrated as rapid and convenient instruments for studying kinetics of phase transformations and mechanisms of chemical reactions [187] [135] [136] [188] [189] [190]. This procedure to calculate activation energy E_a is based on non-isothermal experiments and considered less accurate, because peaks became weaker and broader for slower heating rates, limiting the plotting ranges of $1/E_a$. The Kissinger line could be written as in equation (3.3):

$$ln\left(\frac{T_v^2}{V_i}\right) = \frac{E_a}{RT_v} + A \qquad (3.3)$$

Symbols have the following meanings: E_a [J mol^{-1} K^{-1}] activation energy of reaction, Tv [K] – temperature point corresponding to maximum reaction rate (maximum temperature of reaction peak), Vi [K s^{-1}] – heating rate used to determine

[53] Reprinted with permission by Akadémiai Kiadó Zrt. Budapest, Hungary.

the DSC curve, R [J mol^{-1} K^{-1}] – universal constant of gases, A – constant specific to analyzed material.

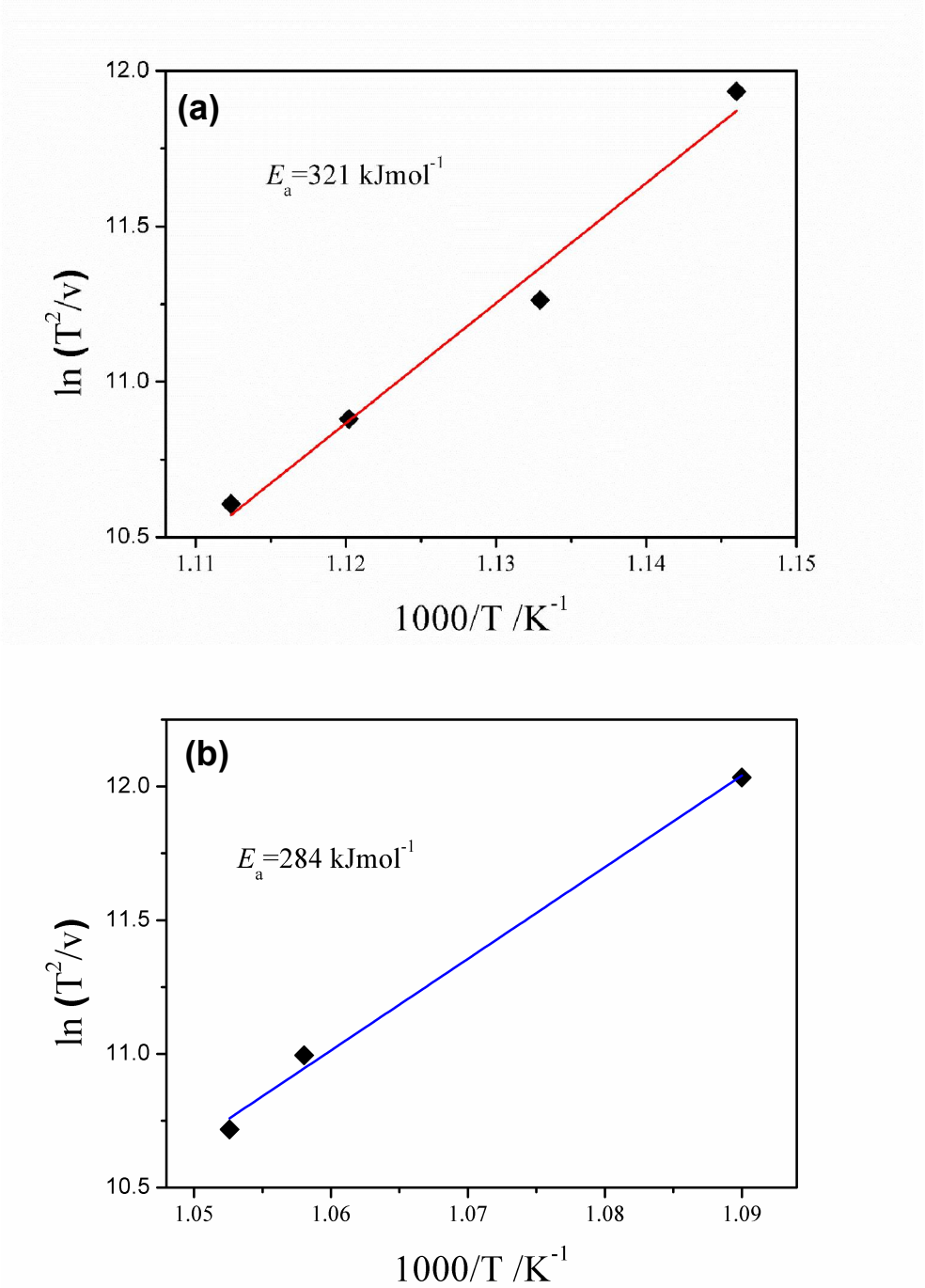

Figure 3.7. Kissinger's lines of exothermic reactions: (a) 1st exothermic reaction; (b) 2nd exothermic reaction [13][54].

Activation energy of reaction E_a could be determined based on equation (3) as the slope of line represented in following coordinates:

$$ln\left(\frac{T_V^2}{V_i}\right) = F\left(\frac{1}{T_V}\right) \qquad (3.4)$$

[54] Reprinted with permission from Akadémiai Kiadó Zrt. Budapest, Hungary.

For this particular case, the *Ea* values were calculated from the maximum temperatures of the two exothermic peaks that resulted from deconvolution process of experimental DSC curves for 5, 10, 15, and 20°Cmin^{-1}, given by Table 3.3. The maximum temperature values of exothermic peaks for different heating rate are given in Table 3.3. These values allowed calculation of Kissinger's line for the exothermic reactions that were represented in figure 3.7. Resulting activation energy for exothermic reaction was E_{a1} = 321 kJ mol^{-1} for the first exothermic peak and E_{a2} = 284 kJ mol^{-1} for the second one. The values of the second exothermic reaction for heating at 10°C min^{-1} were outliers for calculation of Kissinger's line.

The activation energies that were determined for the two exothermic reactions are comparable with activation energies necessary to form Al-Fe intermetallic phases. For example, activation energy for the formation of Al_5Fe_2 as reaction product between Al and Fe powders is *Ea*=146.8 kJ mol^{-1} [191] or *Ea*=144.7 kJ mol^{-1} (1.5 eV) [185], while activation energy of AlFe is *Ea*=202.6 kJ mol^{-1} (2.1 eV) [185]. If oxidation of aluminum is considered, activations energies are *Ea*=120 kJ mol^{-1} [180] for the formation of amorphous alumina, *Ea*=227 kJ mol^{-1} [180] for γ-alumina and *Ea*=306 kJ mol^{-1} [180] for α-alumina, values that are even closer to energies of the two exothermic reactions that were evidenced. However resulting values do not allow at this point to establish a univocal relation of each exothermic reaction with formation of intermetallics or oxidations phenomena, which probably occur simultaneously (figure 3.7).

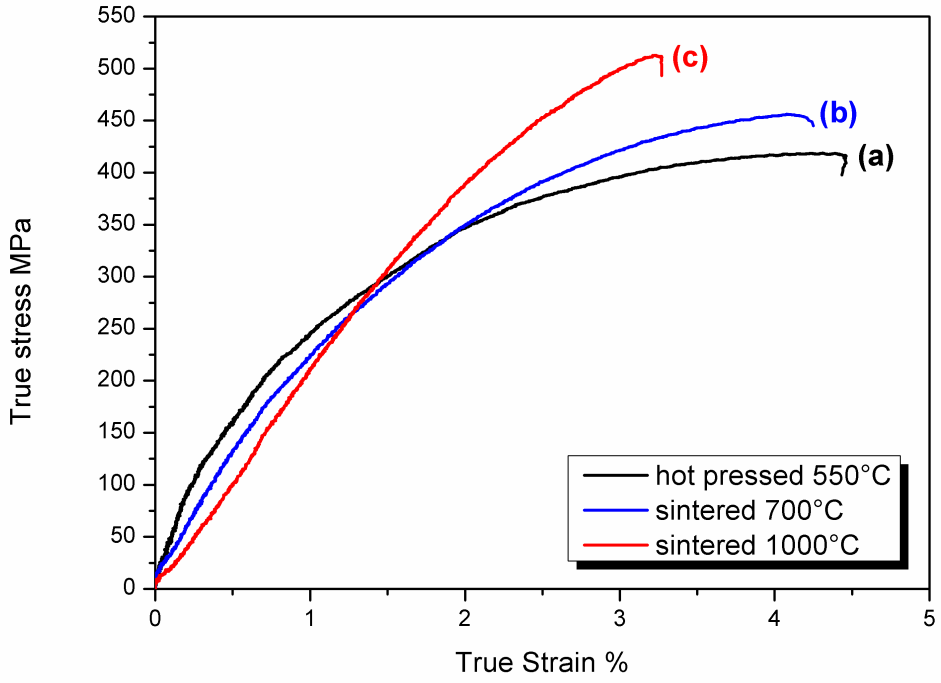

Figure 3.8. Compressive stress-strain curve measured for a 4 mm x 4 mm x 8 mm parallelepiped cut from composite samples[55].

[55] Mechanical properties are still in evaluations with consistent assistance from IFW Dresden, especially from Dr. M. Stoica and R. Parthiban.

Testing of mechanical properties at different structural stages are relevant for optimization of sintering treatment. Therefore, some initial compression tests were performed at room temperature on an INSTRON 8562 electromechanical device coupled with a laser extensometer. The tests were completed on 4x4x8 mm^3 block-shaped specimens under quasistatic loading in track-control mode (displacement speed 10^{-3} mm/s). The samples used for the mechanical tests were cut perpendicular to the pellet faces (i.e. along the main axis of the cylinder) and carefully polished plan-parallel.

As seen in figure 3.8, hot pressed samples already have an ultimate compressive stress of 420 MPa. Fracture occur at a strain value of 4.5%. These high mechanical properties could be attributed mainly to primary reinforcement with ex-situ alumina particles. Sintering at 700°C considerably increase compression strength up to 458 MPa, without significant reduction of strain, which is about 4.24%. This strength improvement could be attributed to formation of secondary alumina, although formation of *in-situ* reinforcement during hot pressing cannot be excluded. Increasing the sintering temperature up to 1000°C produces a higher compression strength of about 512MPa that could be attributed mainly to complete decomposition of Fe_2O_3 and a higher proportion of secondary alumina. However the composite has a lower ductility, since fracture strain decreases at only 3.3%. These testing results open way to optimization of the sintering parameters depending of properties required for different applications.

3.2.3. Conclusions

Both experimental results and mathematical modelling revealed the complex transformations that occur during *in-situ* fabrication of Al-Al_2O_3 composites at relatively low temperatures. Mathematical processing of DSC curves evidences the presence of two distinct exothermic reactions, under 700°C and partially superposed to the endothermic melting of aluminum matrix, that could be related with internal oxidations of Al and/or formation of new Al-Fe phases. Investigations performed by mean of EDX and XRD investigations on composite samples sintered for 1 hour at 700°C evidenced the *in-situ* decomposition of iron oxide particles (7.5% vol.) and formation of some Al_5Fe_2 and AlFe intermetallic phases, as well as some constituents that could not be determined at this stage. Some of microstructural transformations seemed to affect even the aluminum matrix, since the peaks of aluminum could not be evidenced on the XRD pattern of sintered composites. Some alteration of alumina peaks that were evident on hot pressed preforms and attenuated on sintered samples, also suggests some metastable formations of alumina. Although the results indicate that fabrication of *in-situ* composites at temperatures below 700°C is possible, further microstructural investigations would be necessary to differentiate between fractions of alumina that were introduced *ex-situ* or produced *in-situ* by mean of reactive sintering, as well as the effect that secondary alumina may have on mechanical properties.

Chapter 4. Advanced microstructural characterization of composites by mean of image processing

4.1. Basic concepts

The present chapter is focused on the use of *image processing* techniques applied to evaluation of DRAMC microstructures resulting from light microscopy investigations [14], [15]. These contributions are relevant since distribution of reinforcement particles is considered critical for some mechanical properties, such as ductility and toughness [1], [2], [17], [21], [157].

As stated before in Chapter 3, the particle reinforcement is unanimously considered a most promising method to improve mechanical properties of lightweight alloys, based mostly on aluminum, magnesium or titanium. Consequently, significant increase of strength, stiffness, wear resistance and fatigue limit may be achieved. Among the fabrication techniques, powder metallurgy has a special role, based on some major advantages such as structural homogeneity or possibility to embed even very small particles at reinforcement proportions up to 60%. Since fabrication costs seem to be critical for applications, some general tendencies have been observed in the fabrication by mean of ex-situ methods:

- Fabrication techniques should be based on standard P/M technologies, usually a *blending-pressing-sintering* route similar to classic materials, that are easy to reproduce and could be implemented with minor technological modifications;
- Both metallic particles and ceramic reinforcements have to be cheap and produced in large quantities, preferably already available on the market;

This last requirement usually produces large difference in particle size between metallic and ceramic powder that could affect material homogeneity, especially when ceramic reinforcements are added in higher proportion [160]. Therefore, conventional PM techniques will determine formation of clusters and pores, where ceramic particles are agglomerated inside metallic matrix, as seen in Figure 4.1 and Figure 4.2.

Reinforcement clustering is responsible for dramatic loss of material toughness and ductility, and for this reason secondary processing by mean of high-ratio plastic deformation; becomes necessary for improvement of particle distribution. Clustering is more pregnant as reinforcement proportion increases, which is evident if microstructures are compared, as for example a composites with 5% vol. and another one with 15% vol. Some examples of images realized by mean of light microscopy and scanning electron microscopy (SEM) are presented in Figure 4.1 and Figure 4.2, respectively. While at the 5% vol. composite the clusters of composite are evident, but discontinuous and relatively reduced in number (Figure 4.1(a) and Figure 4.2(a)), higher levels of reinforcement levels seems also to produces of networks of ceramic particles at the limit of metallic grains, which is responsible for extreme fragility of resulting composites, as seen in Figure 4.1(b) and 4.2(b) for the composite with 15% vol. of ceramic particles.

Another important observation on Figure 4.1 is the important presence of pores, which is rather unusual after liquid phase sintering that is customary for Al alloys, which usually fill majority of gaps between particles. Larger magnifications reveal that pores are caused by ceramic agglomerations (Figure 4.1 (c)). It seems that metallic melt does not wet ceramic and superficial tension prevent the liquid phase to penetrate inside cluster. The result consists in a large proportion of pores that are present inside material after sintering. Since clusters are more frequent for larger reinforcement proportion, pore incidence follows the same tendencies.

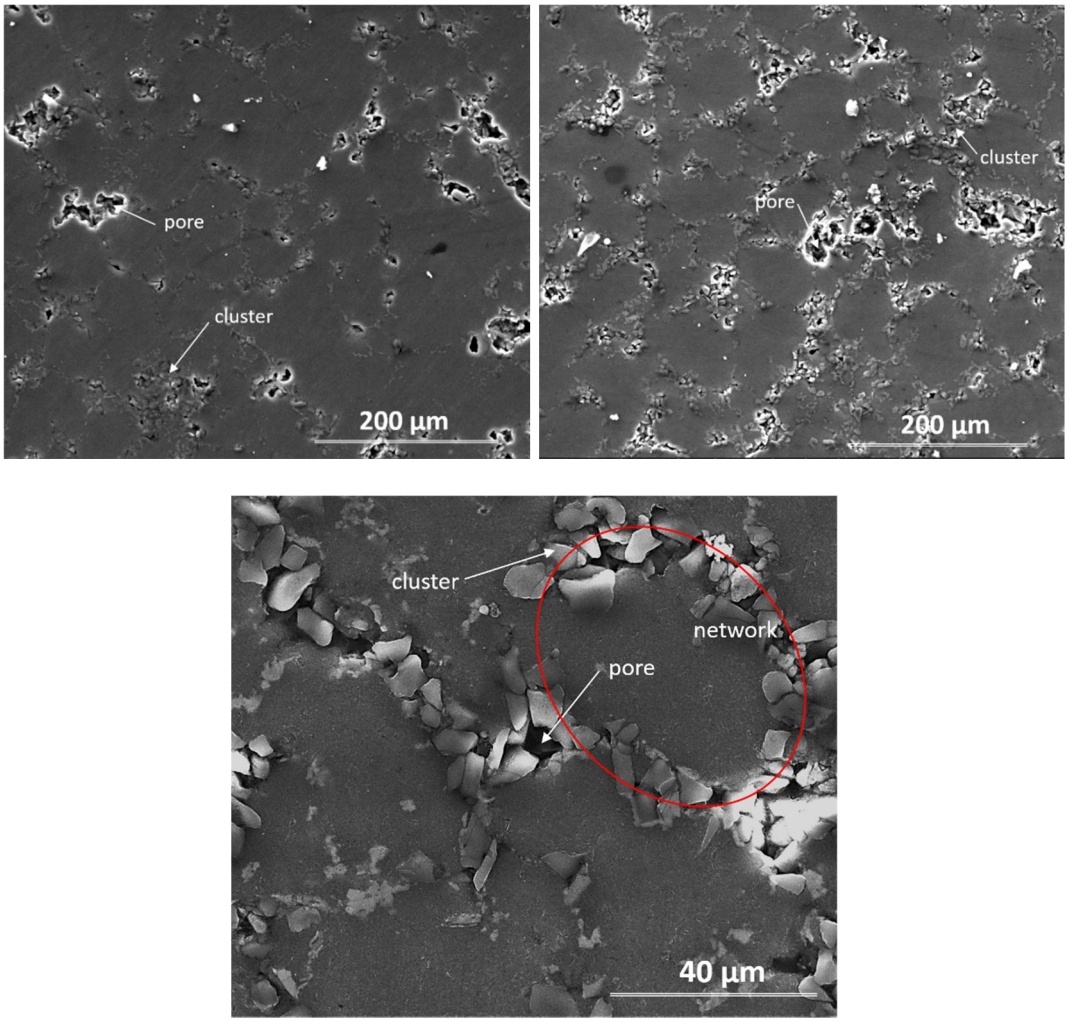

Figure 4.1. SEM images of Al-matrix composites reinforced with SiC particles: (a) 5% vol. SiC – some particle clusters and pores are visible; (b) 15% vol. - clusters are more frequent and network of particles is formed; (c) higher magnification of 15% vol. composite reveals that some particles are only partially embedded [3].

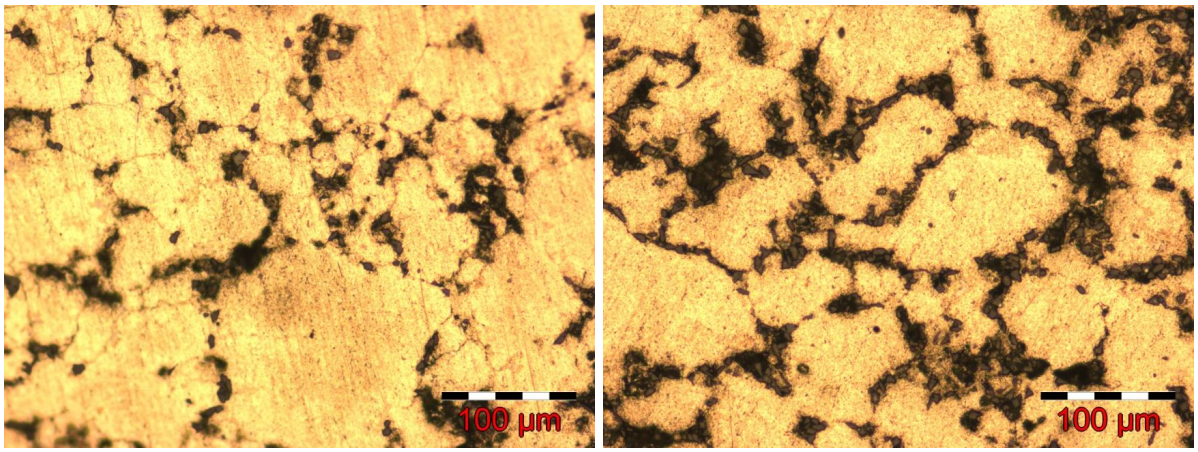

Figure 4.2. Light microscopy images of Al-matrix composites reinforced with SiC particles: (a) 5% vol. SiC – dark colored clusters of ceramic particles; (b) 15% vol. – a network of particles is formed at the limits of metallic grains [3].

In order to improve material quality, especially by mean of ceramic redistribution and elimination of pores, hot deformation operations are usually included in the fabrication route. Only high degree of hot plastic deformation is able to provide a re-distribution of particle reinforcement and removal of clusters. Meanwhile the pore that still exist after sintering the *blend-press-sintering* route could also be closed. The effects of microstructural changes represented by the removal of clusters and pores changes are concretized in the improvement of mechanical properties.

So far both clustering of ceramic particles during PM processing and redistribution of reinforcement have been evaluated mostly qualitative. This research program is proposing a more objective tool that could better evaluate microstructural effects of plastic deformation as secondary processing, based on image processing. The computerized processing of the images assumes that a number of mathematical operations have to be followed and logical decisions have to be made in a precise and organized manner.

4.2. Experimental materials

Computerized image processing of microstructural images is exemplified on some DRAMCs fabricated by mean of classic *blending-pressing-sintering* PM technique. The powder blends consists of a mix of polyhedral-shaped metallic powders of Ecka ALUMIX 123 aluminum alloy with particle diameters between 75 – 95 μm and polygonal silicon carbide (SiC) particles with nominal diameter size of 8,5 μm. The nominal composition of aluminum alloy is given in Table 4.1. The SiC powders are produced at larger scale as grade F800 abrasive powder for polishing suspensions. Volume proportions of reinforcements are 5, 10, 15 and 20%.

Table 4.1. Theoretical composition of ALUMIX 123 powder.

Type	Sint.-Alloy	Cu [%]	Mg [%]	Si [%]	Zn [%]	Lubricant [%]	Al
ALUMIX 123	AlCuSiMg	4,5	0,5	0,7	-	1,5	Bal.

Considering that diameter ratio between metallic and ceramic powder is approximately (D/d)=10, it may be concluded that theoretically, homogeneous mixing is possible only for reinforcement proportion of up to 5% vol., as seen in Table 4.2 . Higher reinforcement proportion is likely to produce agglomeration of smaller ceramic particles at limits of larger metallic particles. These agglomerations are likely to produce clustering after the metallic matrix is sintered.

Table 4.2. Limits of acceptable diameter ratio for homogenous mixing [160].

Reinforcement Proportion V [% Vol.]	$(D/D)_{Min}$	$(D/D)_{Max}$
5	2,3	17
10	1,7	8
15	1,6	5
20	1,5	3,4
25	1,5	2,4
30	-	-

Compaction of powder blend was performed at 650 MPa in a unidirectional double-action die, using preliminary lubrication of tool surface with graphite grease. Apparent density above 90% were achieved for all green compacts, regardless the proportion of reinforcement.

Since ceramic particles seem to have no influence over the position of solidus or liquidus temperature of the Al alloy [2], the sintering treatment was applied at 600°C for 30 minutes in argon atmosphere. Because the solidus point of the Al-alloy is at approximately 550°C and liquidus at 650°C, it may be concluded that sintering was made in the presence of the liquid phase.

Redistribution of ceramic reinforcement was achieved by mean of direct hot extrusion. Initial samples of 18 mm diameter were deformed at diameter values of 12, 9 and 6 mm, which corresponded to deformation ratios between incident and resulting section areas ($i = d_o^2/d_1^2 = A_0/A_1$) of 2.25, 4 and 9 respectively.

Direct hot extrusion of composites requires special attention, since friction between ceramic particles and tool may cause stick-and –slip deformation involving poor surface quality. Therefore a special technique has been developed using a pure aluminum pads, to reduce friction. Optimum deformation temperature has been determined to be 500°C. Remarkably, metallographic investigations determined that pores are no longer present after extrusion, even at low deformation ratio.

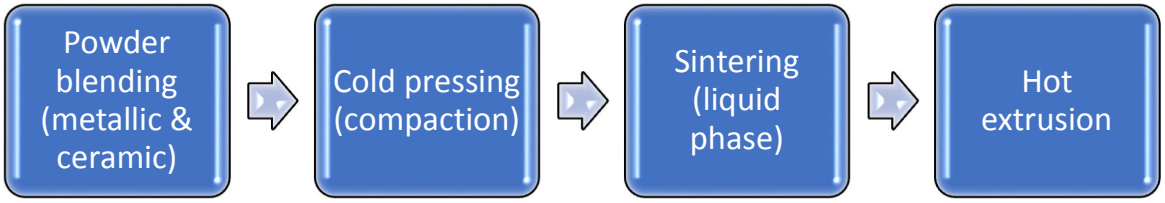

Figure 4.2. Fabrication route for the composite samples.

The sequence of technological operations is illustrated in Figure 4.3 and fabrication details are presented elsewhere [3].

4.3. Computerized image processing method[56]

The algorithm that is used for the image processing of composite microstructures contains a succession of logical mathematical and scientific operations that are resumed in figure 4.4 [192].

Image acquisition. Image acquisition assumes digitalization (transformation of analog images into numerical ones) of the virtual image of the real objects obtained using the microscope. During the entire program of test and experiments two microscopes have been used: an optical Olympus BX51M microscope and a SEM FEI Inspect S. In order to digitize the optical images a 4.8 MP discrete sensor array on an Olympus ColorView microscope digital camera has been used. During SEM acquisition both backscattered and secondary electron detectors has been used, on 1 MP images.

Image Compression. During all mathematical calculations and transformations only 256 gray levels, monochrome images and 2 levels black and white images has been processed. The optical microscope images are acquired in colors and therefore need to be compressed from 16.7 million colors (24 bits images) to a 256 gray levels

[56] Special mention to C. Locovei, co-author of [14] [15] [16], for contribution to mathematical model of image processing.

monochrome (8 bits) images. The color information is stored in 24 bits RGB quantized images using 8 bits for each color, R,G,B, including 256 levels of gray. The gray tones are obtained when R = G = B. The color to grayscale image transformation is done by calculating a luminance value, L, for each pixel of the digital RGB color image using a linear transformation as in Equation 4.1.

$$L = 0.299 \cdot R + 0.587 \cdot G + 0.114 \cdot B \qquad (4.1)$$

The SEM images could be processed as they are, no compression needed as the depth of the SEM images is 8 bits, only.

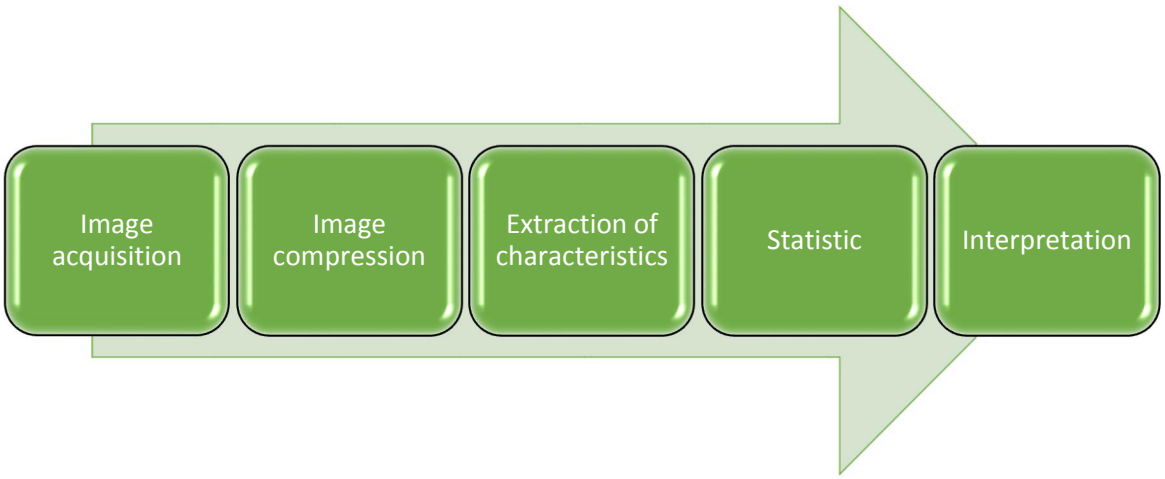

Figure 4.4. The algorithm used in image processing (after [14].

Extraction of characteristics. Extraction of characteristic is the most complex step in terms of mathematical calculus. First step in extraction of characteristics is the evaluation of the background illumination. The background illumination is evaluated using morphological operations. Morphology is a broad set of image processing operations based on shapes. Morphological operations are nonlinear operations that apply a structuring element to an input image in order to generate the output image. The input and output images are the same size and depth. When a morphological operation is applied to a digital image, the value of each pixel of the output image is calculated by means of comparison of the corresponding pixel in the input image with the pixels in its neighborhood. The shape and size of the neighborhood defines the structuring element of the morphological operation. The way the shape and size of the structuring element are assigned sets the morphological operation sensitivity to a specific shape in the input image.

The more often two primitives used in morphological operations are *dilation* and *erosion*. Dilation is defined as the morphological operation that assigns to the output pixel the maximum value of the pixels in the neighborhood of the input pixel, as the "neighborhood" is defined by the structuring elements. As a consequence, the dilation adds pixels to the boundaries of objects in an image and the number of added pixels depends on the size and shape of the structuring element. Suppose a 3x3 structuring element (SE) as follows, Equation 4.2:

$$SE = \begin{pmatrix} 0 & 1 & 0 \\ 1 & 1 & 1 \\ 0 & 1 & 0 \end{pmatrix} \qquad (4.2)$$

Assume the *input binary image* (IBI), Equation 4.3:

$$IBI = \begin{pmatrix} 1 & 0 & 0 & 0 & 0 & 0 & 0 & 0 & 1 \\ 0 & 1 & 0 & 0 & 0 & 0 & 0 & 1 & 0 \\ 0 & 0 & 1 & 0 & 0 & 0 & 1 & 0 & 0 \\ 0 & 0 & 0 & 1 & 0 & 1 & 0 & 0 & 0 \\ 0 & 0 & 0 & 0 & 1 & 0 & 0 & 0 & 0 \\ 0 & 0 & 0 & 1 & 0 & 1 & 0 & 0 & 0 \\ 0 & 0 & 1 & 0 & 0 & 0 & 1 & 0 & 0 \\ 0 & 1 & 0 & 0 & 0 & 0 & 0 & 1 & 0 \\ 1 & 0 & 0 & 0 & 0 & 0 & 0 & 0 & 1 \end{pmatrix} \qquad (4.3)$$

Applying the dilation operation on the pixel (2, 3) of the input binary image – Equation 4.3 - using the structuring element – Equation 4.2 – the value of the output pixel (2, 3) is 1. In a similar manner the dilated calculated output pixel (6, 8) is 0. The entire *dilated output binary image* (DOBI) using structured element as defined in Equation 4.2 is as follows, Equation 4.4:

$$DOBI = \begin{pmatrix} 1 & 1 & 0 & 0 & 0 & 0 & 0 & 1 & 1 \\ 1 & 1 & 1 & 0 & 0 & 0 & 1 & 1 & 1 \\ 0 & 1 & 1 & 1 & 0 & 1 & 1 & 1 & 0 \\ 0 & 0 & 1 & 1 & 1 & 1 & 1 & 0 & 0 \\ 0 & 0 & 0 & 1 & 1 & 1 & 0 & 0 & 0 \\ 0 & 0 & 0 & 1 & 1 & 1 & 1 & 0 & 0 \\ 0 & 0 & 1 & 1 & 0 & 1 & 1 & 1 & 0 \\ 0 & 1 & 0 & 0 & 0 & 0 & 1 & 1 & 1 \\ 1 & 0 & 0 & 0 & 0 & 0 & 0 & 1 & 1 \end{pmatrix} \qquad (4.4)$$

Erosion is defined as the morphological operation that assigns to the output pixel the minimum value of the pixels in the neighborhood of the input pixel, as the "neighborhood" is defined by the structuring elements. As a consequence, the erosion removes pixels from the boundaries of objects in an image and, similar to dilation, the number of removed pixels depends on the size and shape of the structuring element.

$$EOBI = \begin{pmatrix} 0 & 0 & 0 & 0 & 0 & 0 & 0 & 0 & 0 \\ 0 & 0 & 1 & 0 & 0 & 0 & 0 & 0 & 0 \\ 0 & 0 & 0 & 0 & 0 & 0 & 0 & 0 & 0 \\ 0 & 0 & 0 & 0 & 0 & 0 & 0 & 0 & 0 \\ 0 & 0 & 0 & 0 & 0 & 0 & 0 & 0 & 0 \\ 0 & 0 & 0 & 0 & 0 & 0 & 0 & 0 & 0 \\ 0 & 0 & 0 & 0 & 0 & 0 & 0 & 0 & 0 \\ 0 & 0 & 0 & 0 & 0 & 0 & 0 & 0 & 0 \\ 0 & 0 & 0 & 0 & 0 & 0 & 0 & 0 & 0 \end{pmatrix} \qquad (4.5)$$

Applying the erosion operation on the pixel (2, 3) of the input binary image – Equation 4.3 - using the structuring element as defined in Equation 4.2, the value of the output pixel (2, 3) is 0. In a similar manner the eroded calculated output pixel (6, 8)

is 0. The entire eroded output binary image (EOBI) using structured element defined in Equation 4.2 is – Equation 4.5:

The input binary image (left) and of the output binary images (center and right) are presented in Figure 4.5.

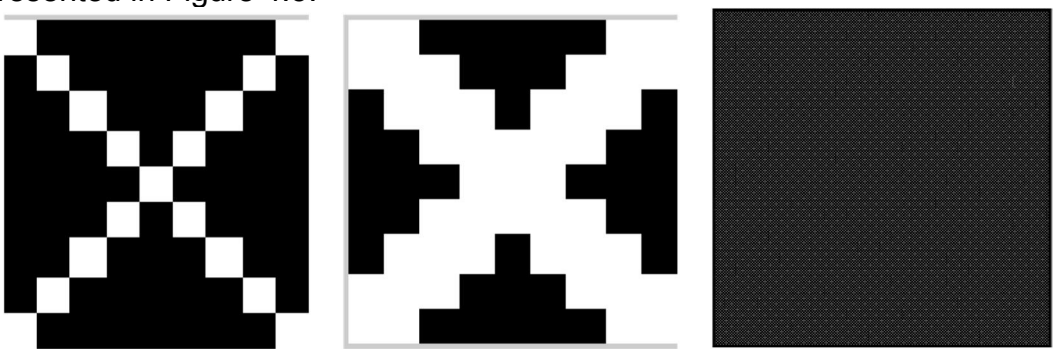

Figure 4.5. Optical representation of the IBI (left), DOBI (center) and EOBI (right) [14][57].

Morphological functions position the center of the structuring element, also named the origin, over the corresponding pixel in the input image. For pixels at the edge of the image, it is possible that the structuring element is extended over the border of the image. In order to process these border pixels, the morphological functions have to assign a value to the undefined pixels. The value of supplementary added pixels depends of the morphological function. In the case of morphological dilation, the supplementary pixels are set to 0, for binary and gray images. In the case of the morphological erosion, the value of the supplementary pixels is set to 1 if a binary image is processed. For grayscale images, the value of the supplementary pixels is set to 255.

Two more complex morphological operations are *opening* and *closing*. The morphological opening is defined as morphological erosion followed by morphological dilation using the same structuring element. The morphological closing is defined as morphological dilation followed by morphological erosion using the same structuring element.

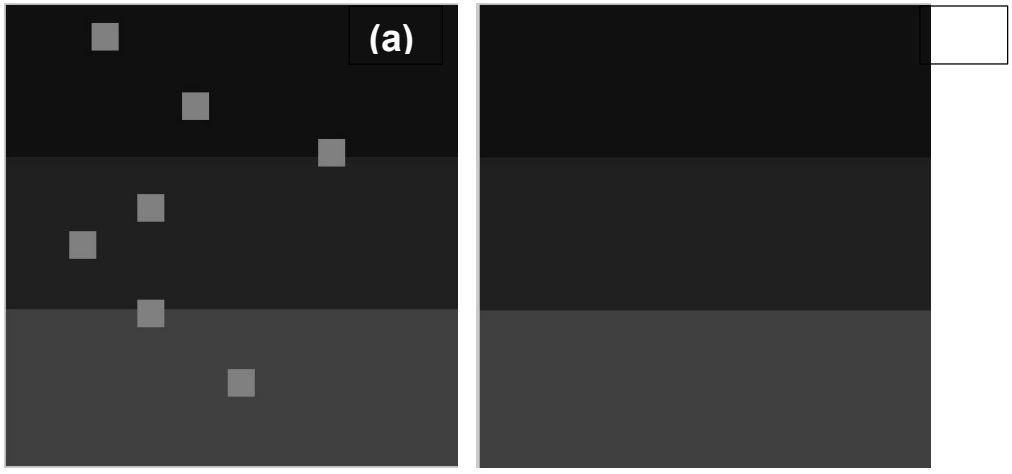

Figure 4.6. Morphological opening of an image: (a) non uniform illumination on a computer generated image; (b) background image resulted after morphological opening of the sample input image [14][57].

[57] Reprinted with permission by Trans Tech Publications Inc., Basel, Switzerland.

In order to calculate the background illumination of any sample image it is necessary to apply a morphological opening to that image. The shape and size of the structuring element depends on the shape and sizes of the particles in the given image. As a means to avoid the shape related issues of the particles the most common option is to choose circular or octagonal shape for the structuring element. The size of the structuring element should be bigger than the diameter of any particle or cluster of particles. In this respect, the size of the structuring element was chosen to be 1/20 of the minimum dimension of the processed images, while the chosen shape was circular.

A theoretical example of background illumination calculus is presented as follows. Assume that an acquired 100 x 100 pixel image has a non-uniform background illumination as in Fig. 4. The particles to be counted are 5x5 squares, randomly distributed, with 2 particles situated on transition illumination area.

After applying the morphological opening to the sample image, using a 10x10 square structuring element, the resulting image is presented in figure 4.6 (b).

The next step to follow is to mathematically subtract the background matrix – as in Figure 4.6 (b) – from the sample image matrix – as in Figure 4.6 (a). The result of the subtraction is presented in Figure 4.7 (a).

The following step is to extract the particles from the background and this is accomplished by converting the 255 gray levels image to a pure 2 levels black and white image. In order to convert the image to a pure black and white it is necessary to set a threshold that will separate the pixels that belongs to particles from the background pixels. This separation is based on the fact that particles are brighter than the background, as the background after morphological opening and subtraction is close to 0. The resulting image after reducing the depth to a pure black and white image is presented in Figure 4.7 (b). After separation the pixels that belong to particles are set to 1 and the background pixels are set to 0.

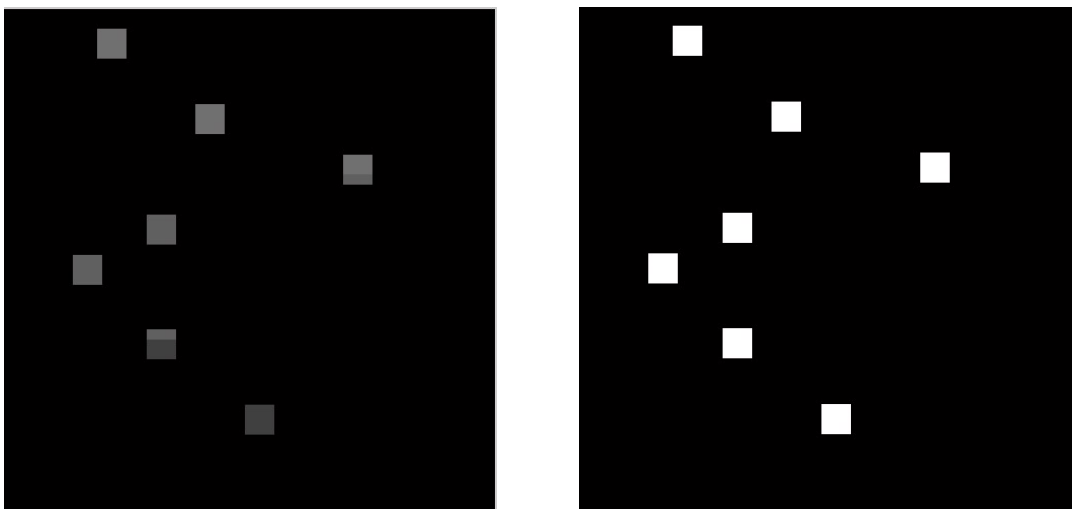

Figure 4.7. Image subtraction: (a) resulting image after subtracting the morphological opening image from the input image; (b) resulting black-white image [14][58].

Statistics. In order to quantify the particles a connectivity test is needed. Connectivity defines which pixels form an object. In a binary image, an object consists

[58] Reprinted with permission by Trans Tech Publications Inc., Basel, Switzerland.

in a group of pixels that are set to 1 and are connected to each other. The shape and dimension of an object depends on how connectivity is defined. In two dimensions, standard morphological connectivity is of two types: 4 connected and 8 connected. 4 connected type connectivity assumes that a 1 value pixel is connected to other pixels if at least one of up, down, left or right neighbor pixels are set to 1. The mask for a 4 connected type connectivity test is shown in Equation 4.6. The mask is placed centered on the test pixel.

$$4CTM = \begin{pmatrix} 0 & 1 & 0 \\ 1 & 1 & 1 \\ 0 & 1 & 0 \end{pmatrix} \qquad (4.6)$$

The 8 connected type connectivity assumes that a 1 value pixel is connected to other pixels if at least one of its neighbor pixels are set to 1. The mask for an 8 connected type connectivity test is shown in Equation 4.7.

$$8CTM = \begin{pmatrix} 1 & 1 & 1 \\ 1 & 1 & 1 \\ 1 & 1 & 1 \end{pmatrix} \qquad (4.7)$$

The masks for connectivity tests can be modified to test for multiple pixel touch as a pixel is set to be a part of an object if a minimum predefined number of neighbor pixels belong to that object. In all processed images a 4 connected type with multiple pixel touch connectivity tests were applied.

All objects have been identified and tagged and the following information was processed:

- Area of objects
- Equivalent diameter (D_{eq}), calculated by area.

Deeper statistics are discussed furtherly.

4.4. Results and discussion

In order to illustrate the above procedure a complete image processing procedure is undergone using the commercially available image analysis software (Olympus AnalySIS Five). The image processing includes particle detection, particle measurement and classification. The following procedure is applied:

- the threshold gray values is set to the values that enables particle separation from the background information;

The detection parameters are defined as follows:

- all particles under 0.75 μm are considered as noise;
- all the border particles are truncated and counted;
- all holes inside particles are filled;
- after the detection of the particles the area of each particle is measured;
- the classification scheme of area is defined as in Table 4.3;
- an equivalent diameter is calculated, based on the median value of area for each class each class;

Table 4.3. Equivalent Diameter Scheme.

Class ID	*From [μm²]*	*To [μm²]*	*D_{eq} [μm]*
1	0	10	3
2	10	20	4
3	20	40	6
4	40	80	9
5	80	160	12
6	160	320	17
7	320	640	25
8	640	1280	35
9	1280	2560	49
10	2560	5120	70

A number of three samples of deformed composites are processed, which are compared with a reference sample of undeformed composite (as sintered state):

- for all the samples the particles to matrix ratio is 10% in volume;
- the deformation ratio *i* is different (*i*= 2.25, 4, and 9).

The particle count for the 10 vol.% particle-matrix ratio and *i* = 2,25, 4, 9 deformation ratio over equivalent diameter are presented in Table 4.5. The resulting images after image processing with Olympus AnalySIS Five are presented in Figure 4.9.

The histograms of the total counted particles is presented in Figure 4.10, while the number of counted particles depending on equivalent diameter is presented are presented in Figure 4.11.

Table 3. Particle count over equivalent diameter (10% particle-matrix ratio; *i* = 2.25, 4, 9 deformation ratio) [14][59]

Class ID	*D_{eq} [μm]*	*Particle count*			
		Sintered	***i* = 2.25 deformation ratio**	***i* = 4 deformation ratio**	***i* = 9 deformation ratio**
1	3	44	89	204	234
2	4	14	19	89	77
3	6	13	13	70	90
4	9	9	14	32	57
5	12	9	10	27	30
6	17	14	8	12	19
7	25	8	7	2	1
8	35	4	2	0	0
9	49	4	5	0	0
10	70	3	0	0	0

[59] Reprinted with permission from Trans Tech Publications Inc., Basel, Switzerland.

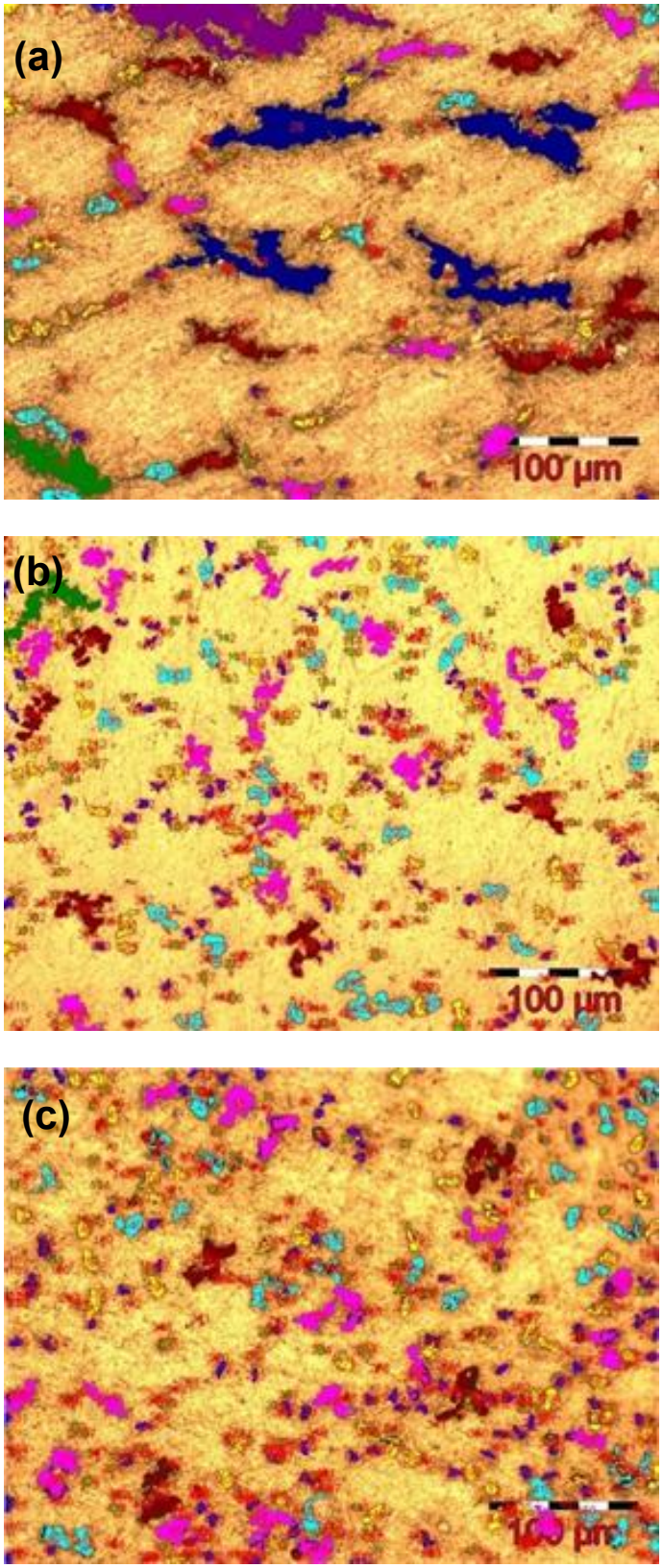

Figure 4.9. Microstructures after computerized image processing: (a) deformation ratio i=2.25; b) deformation ratio i=4; (c) deformation ratio i=9 [14][60].

[60] Reprinted with permission from Trans Tech Publications Inc., Basel, Switzerland.

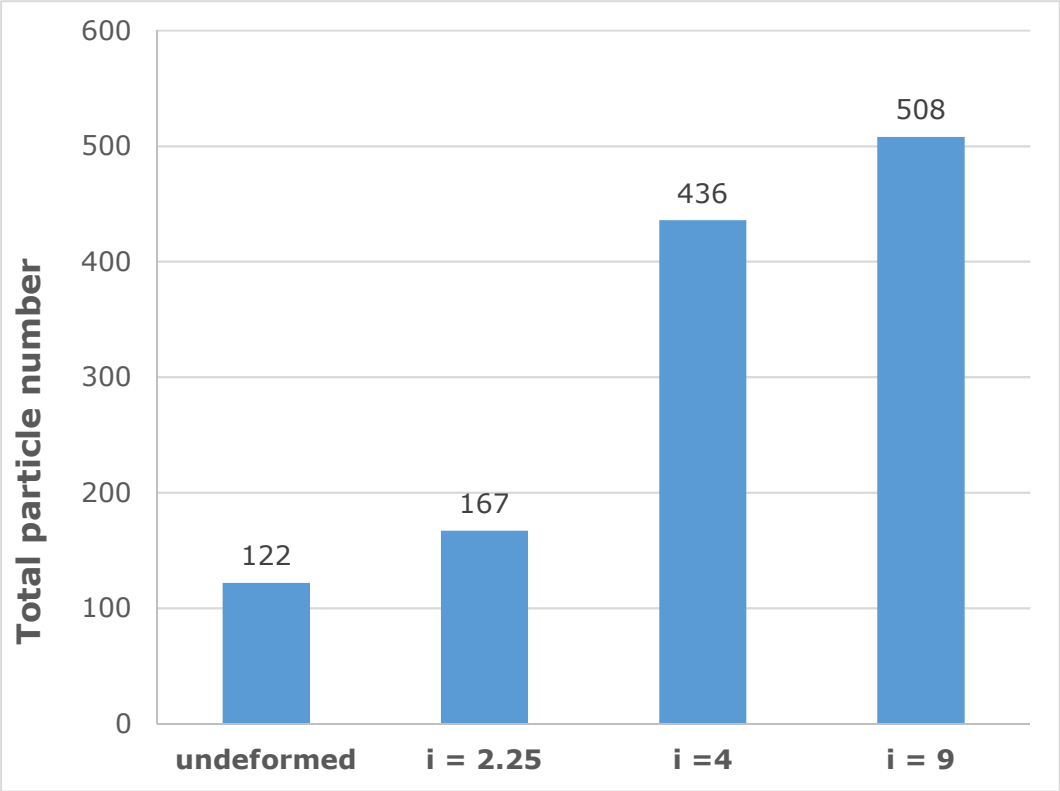

Figure 4.10. Evolution of the total number of counted particles over the deformation ratio of composite material (after [14]).

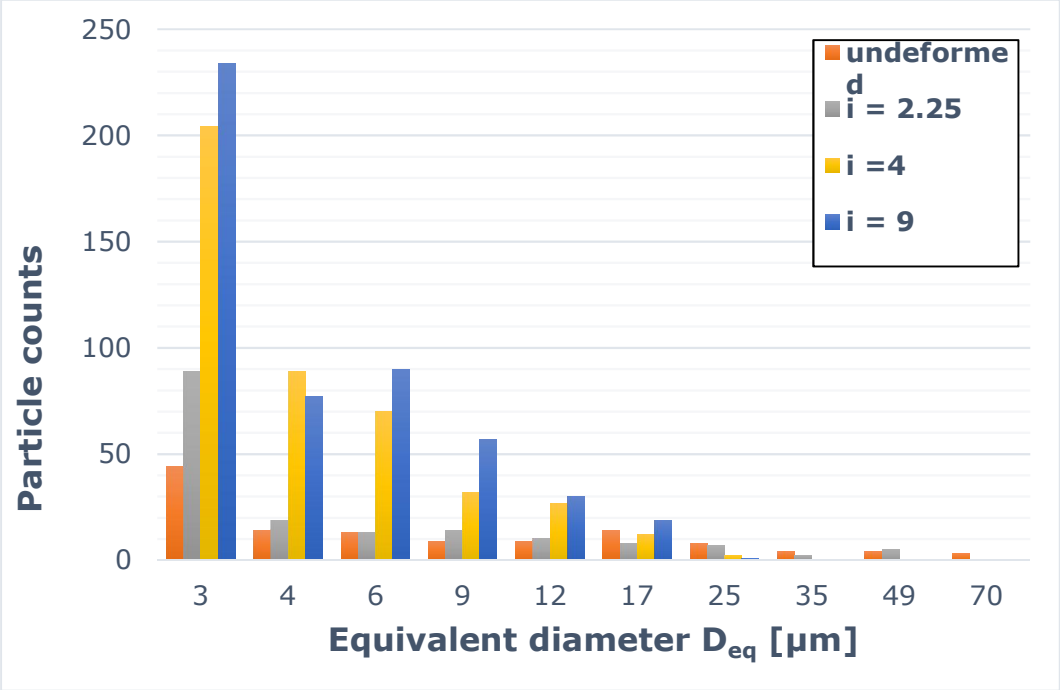

Figure 4.11. Distribution of particles over equivalent diameter of the particle (after [14]).

4.5. Conclusions.

Until recently microstructural analysis has relied mostly on subjective interpretation of images obtained by light of electronic microscopy. The computer aided method of microstructural analysis allows calculation of some quantitative parameters that could be related with morphological changes during processing, and could result in optimization of deformation operations. Evaluation of particles distribution could be considered of primary importance In the case of DRAMCs, since it influences some critical properties like ductility and toughness.

One of the most important conclusion that resulted from the analysis of image processing results is that, as the deformation ratio of composite material increases, there is a significant increase, in the number of total counted particles. Figure 4.10 shows that undeformed composite samples has a number of 122 counted particles, while after deformation at i=9 ratio the number of counted particles on the same size of investigated area increases almost 4 times to 508. However the volume proportion of ceramic particles is the constant. Therefore, it may be concluded that the increase of the counted particle number is a consequence of the fact that the clusters tend to brake in more, but smaller clusters when the composite material is subjected to a higher deformation state, which is reducing the clustering phenomenon, inherited during the material fabrication.

In all the samples subjected to optical computer processing clustering of the particles is present, but the dimension of the clusters tends to decrease with the increase of the deformation ratio of the sample.

In the as sintered conditions there are 11 clusters with an area exceeding 640 μm^2 as follows: 4 clusters exceeding 640 μm^2, but less than 1280 μm^2, 4 clusters exceeding 1280 μm^2, but less than 2560 μm^2 (equivalent diameter D_{eq} = 35 μm), and 3 clusters exceeding 2560 μm^2 (D_{eq} > 70 μm). For a deformation ratio of 2.25 there are 7 clusters exceeding 640 μm^2 (D_{eq} = 35 μm). Remarkably, for higher deformation factors there are no clusters exceeding 640 μm^2.

Further investigations reveal that the tendencies observed on 10 vol. % (the reduction of the number of huge clusters with the increase of deformation factor and the increase in the uniformity of the spatial distribution of the particles with the increase of deformation factor) remain valid for the 5 and 20 vol.%, but the phenomena is more pronounced as the vol.% of the samples increases.

It may be concluded the computerized image processing of microstructural images represent a reliable tool to evaluate the effects of secondary processing of particle-reinforced composite for amelioration of reinforcement distribution within the metallic matrix.

Chapter 5. Career evolution and development prospects

The career evolution is seen on two concurrent levels, with synergic effects on each other, one of them covering academic activities, and the other dedicated to research, both of them in the field of materials science and engineering.

Research activities are intended to follow the main directions that were synthetized in the present habilitation thesis:

- Development of new Ti-based amorphous/crystalline composites for biomedical applications, with suitable mechanical composites, and totally free of harmful additions;
- New amorphous biomaterials with controlled porosity (also known as bulk metallic glass foams - BMGFs) that are compatible with human bone and containing only biocompatible elements;
- Fabrication and characterization of Al-based composites, for applications that require high mechanical properties and low specific weight, especially aeronautics, automotive industry, industrial equipment, electric and electronic devices, home appliances, etc.

Considering the very complex nature of the research activities, creative ideas of even new directions of research could emerged from the future development of the new composites, also in relation with the scientific contributions that will be published in relevant sources, which will be followed closely.

5.1. Development of new Ti-based amorphous/crystalline composites

The concept of replacing the Cu with Ag for development of new Ti-based alloys is an original one, and preliminary results have been proved to be promising, therefore this line of research will be continued in the future.

5.1.1. Optimization of compositions

The design of the new $Ti_{42}Zr_{10}Pd_{14}Ag_{26}Sn_8$ was based on the total replacement of Cu with Ag from the classic $Ti_{45}Zr_{10}Pd_{10}Cu_{31}Sn_4$. Final optimization of composition relied on the molecular orbital method, which predicted that the new alloy complied with the condition for BMG domain. However the final structure of the alloy was composite amorphous/crystalline, with a rather reduced proportion of amorphous matrix, which showed the limits of the method, and require further optimization of the compositions.

Some experimental results presented in Chapter 1 suggest that the new $Ti_{42}Zr_{10}Pd_{14}Ag_{26}Sn_8$ alloy is off eutectic and shows a large temperature interval over which liquid and solid coexists, which is causing an early phase separation of an Ag-rich phase. The morphological study reveals the spherical appearance of this phase, which could indicate that the precipitation takes place in the liquid state and is frozen afterwards by quenching, so the microstructural development of each domain is totally separated. Considering also that Ag is not miscible with Ti and Zr, it may be concluded that the total content of Ag should be subject to optimization, perhaps reduced, in order to eliminate the early separations from liquid state and increase the final proportion of amorphous phase. Indeed preliminary casting tests with a $Ti_{30}Zr_{32}Pd_{24}Ag_7Sn_7$ composition revealed that fully amorphous ribbons may be fabricated by mean of melt spinning, and other compositions are also considered for experiments. Optimization of compositions should also address some improvement of other properties, such as higher GFA, broader SLR etc.

5.1.2. Structural characterization of the Ti-Zr-Pd-Ag-Sn system

Investigations on the newly developed $Ti_{42}Zr_{10}Pd_{14}Ag_{26}Sn_8$ alloy reveal the very complex structure of the Ti-Zr-Pd-Ag-Sn system, containing phases that have not been identified at this stage, therefore further analyses should be carried on, especially at larger magnifications by mean of HR-TEM, SEM, STEM, EDS mapping etc.

So far, DSC analyses have been performed up to 1000°C because of technical limitations, but extensions above that range could be useful in order to elucidate the dynamic of phase transformations.

XRD investigations during heating/cooling, as well as the use of synchrotron radiation are also envisaged, using a similar procedure that was followed for the characterization of the $Ti_{41.5}Zr_{2.5}Hf_5Cu_{37.5}Ga_{7.5}Si_1Sn_5$ alloy.

5.1.3. Design of fabrication technologies

Previous contributions for development of Ti-Zr-Pd-Ag-Sn alloys have relied on experimental samples fabricated by centrifugal and suction casting, for rods up to 5mm in diameter. Results have shown a strong dependence of resulting structure to the fabrication technique, which suggests that for consistent results new fabrications route should be considered. Based on the experience in fabrication of new materials achieved so far, combined ultra-rapid cooling and powder metallurgy techniques could provide solutions for production of BMGs when the GFA ability of alloys is too low.

For example, since preliminary tests show that some Ti-Zr-Pd-Ag-Sn compositions result as amorphous ribbons or powders, these could be consolidated to bulk products by mean of thermomechanical, i.e. hot pressing, sintering, SPS etc.

5.1.4. Evaluation of corrosion behavior and biocompatibility

So far the biologic effects of metallic Ag remain ambiguous in scientific references that were published. A considerable number of contributions are based on the use of bactericidal effects of Ag nano-particles, surface implantation of Ag ions, addition of Ag as alloying elements, etc. The beneficial effects on preventing infections with many bacteria related with the use of orthopedic implants are already well-documented.

On the other hand some researchers stress out the possible cytotoxic effects of Ag, which could be detrimental to recovery and proliferation of living tissues. It may be concluded at the present level of knowledge that the effects of Ag rely on the rate of ion release and are strongly dependent on each application and host organism. Therefore a comprehensive evaluation of biocompatibility for each alloy and type of applications is critical.

Assessment of biocompatibility will be based on several stages of investigations:

Preliminary investigations should determine the electrochemical properties in the phosphate buffered saline electrolyte, as well as corrosion behavior in simulated body fluids (SBFs). In vitro response of cell cultures in terms of cell viability, seeding and proliferation, as well the possible morphological changes are also crucial to determine potential cytotoxicity or other toxic effects of newly developed alloys.

Approved in-vivo experiments on animals will be conducted in collaboration with the University of Medicine and Pharmacy Timisoara on compositions that already show excellent anti-corrosion properties during preliminary tests, following procedures that

are generally accepted. Biological effects of implanted samples will be evaluated considering some biological responses. Blood samples will be analyzed to determine levels of metallic ions that are known to have documented or possible toxic effects, such as Cu, Ni, Al, etc. [5] Samples that are sub-periosteally implanted on the surface of the bone, to determine their potential for use for osteosynthetic devices, should also be investigated histologically by light microscopy, to exclude possible harmful effects, such as bone resorption, inflammations, necrosis, wear debris etc.

Possible superficial modifications of materials after implantation periods of several weeks or month are determined after extraction by mean of scanning electron microscopy (SEM), while changes of composition, especially inclusion of new elements, are evaluated by energy dispersive spectroscopy (EDS).

Ethical issues on animal use for research, will the strictly observed. In accordance with the applicable law – Council Directive 86/609/EEC on the Approximation of Laws, regulations and administrative provisions of the Member States regarding the protection of animals used for experimental and other scientific purposes, Law No. 43/2014 of the Romanian Parliament on the protection of animals used for scientific purposes – the researchers will observe the following aspects:

- Type, number, source and habitat of animals. As the project involves animal experiments, the researchers recognize the “3Rs” rule in the design of study protocols: Reduction, Replacement, Refinement. On these premises, the number of animals must be kept as low as possible, as there is no alternative for their use. All experimental animals will receive adequate housing, nutrients, water and care in accordance to their health and well-being as well providing the environmental conditions in which they are kept, to be be checked on a regular basis. The provider of animals will be a certified commercial enterprise / animal facility.
- Approval of the experiments by the relevant local committee. Approval by the ethics committee in regards with the animal experimental protocol will be obtained before the start of the experiments proposed in the present application.
- At the end the experiments, animals will be euthanized when no follow-up is required.

5.1.5. Characterization of mechanical properties

In view of the primary application of these new materials as orthopedic implants, which are subject to complex mechanical stress, mechanical testing is of utmost importance.

Beside compression tests that are customary as intermediate investigations for small sized samples, a complex testing program will be setup to determine tensile strength, ductility, toughness, hardness, fatigue and wear behavior.

Special attention will be given to rigidity that should be as closed as possible to human bone, and to the relation between mechanical strength and Young’s modulus, which is important especially for long-term implants.

If the processing by mean of PM will be used for fabrication, fabrication of materials with controlled porosity will be considered, as a way for reduction of rigidity and better connection to living tissue.

5.2. Bulk metallic glass foams

Development of the new porous new $Ti_{42}Zr_{40}Ta_3Si_{15}$ alloy proved to be very successful, and the results were published in *Acta Biomaterialia*, which is a leading publication in the field of biomaterials.

The new BMGF contains only biocompatible elements, has an amorphous structure and 14 vol.% porosity, which assure some interesting properties: the rigidity around 52 GPa, close to the Young's modulus of cortical bone, which is between 4 and 30 GPa, a compressive strength over 337 GPa and good biocompatibility in simulated body fluid.

5.2.1. New BMGFs compositions and morphologies

The new $Ti_{42}Zr_{40}Ta_3Si_{15}$ alloy seems to have considerable potential for development, however optimization of composition may still be needed. Although structural investigations (DSC, XRD, TEM) indicate that melt-spun ribbons are amorphous, some crystalline fractions may still be present, at least in some batches of samples. Therefore, additional investigations may be necessary, especially large magnification microscopy. Some changes of compositions, including addition of new elements like Nb, could improve the GFA and guarantee the fully amorphous character. A larger SLR and higher thermal stability could also be beneficial for subsequent mechanical processing. DSC results achieved so far should be corroborated with TMA results to confirm or determine T_g, T_x, tensile and compression modulus, thermal expansion, etc.

Apart from new compositions, different porosity fractions and size distribution of pores should be investigated, regarding their influence on Young's modulus, strength, fatigue, as well as the biological behavior, since the size of superficial pores and surface topology influence the viability and proliferation of living tissues.

5.2.2. New processing routes

So far, the starting point of the processing route for the new Ti-Zr-Ta-Si BMGFs has been the fabrication of melt-spun ribbons that have considerable ductility and have to be fragmented by mean of cryo-milling, which is difficult, expensive and time-consuming. Therefore, experiments should determine if direct production of amorphous powder via melt atomization or mechanical alloying techniques could be feasible.

Powders, regardless of the fabrications techniques (cryo-milling or atomization), will be also selected in several granulometric fractions, for better uniformity of resulting pores, which did not happened so far because of the very small quantities of available powder.

Although consolidation by mean of hot pressing seems to be successful, it obviously has limitations, especially in controlling the fraction, size of shape of the pores. For these reasons, other techniques of porosity control should be experienced, like for example the use of soluble or vaporizable replicators.

One of the most important issue of BMGFs fabrication is final consolidations, since processing temperature should avoid crystallizations. Besides the hot pressing that has been used so far, other procedures are envisaged, for example HIP or SPS.

Valorization of the deformation ability of BMGs inside the SLR will be made by mean of hot deformation experiments, for example hot extrusion or rolling.

5.2.3. Assessment of biocompatibility

The newly developed $Ti_{42}Zr_{40}Ta_3Si_{15}$ alloy contains only elements that are considered biocompatible, without any estimated toxic effects to human body, which represents a solid fundament for biocompatibility.

Nevertheless, assessment of biocompatibility is a very complex process, which should contained some mandatory phases, such as evaluation of electrochemical properties and corrosion behavior in simulated body fluids, as well as specific *in vitro* and *in-vivo* experiments, similarly with the procedure described by the paragraph 5.1.4.

5.2.4. Characterization of mechanical properties

Characterization of mechanical properties represents a major task, since the main applications of the Ti-Zr-Ta-Si BMGFs rely on orthopedics. Apart from the mechanical strength, rigidity, ductility and toughness, which are regularly tested on this class of biomaterials, special attention should be given to fatigue behavior, since as presented in Chapter 2, some authors indicate possible negative influence of the pores on this very important property.

One of the major breakthrough of this new development of the Ti-Zr-Ta-Si BMGFs could be represented by the possibility to control the *apparent* Young's modulus by mean of material porosity. Values of rigidity close to human bone could be of key importance in avoiding the stress shielding effect produced by the conventional implants.

5.3. Discontinuously reinforced Al-matrix composites

Researches that where undergone so far indicated the possibility of increasing the proportion of reinforcement using the *hybrid composite* concept, based on both in-situ and ex-situ methods.

Future researches will have the objective to determine some aspects related with phase transformations and their influences on mechanical properties:

- Comprehensive testing of mechanical properties (mechanical strength, rigidity, ductility, toughness, hardness, fatigue, etc.) as function of reinforcement proportion and fabrication parameters;
- Some of resulting phases resulting from the reactive sintering treatments have not been so far identified, neither their contribution to the changes in properties, which require further microstructural characterization;
- The practical limits of *in-situ* reinforcement still have to be determined, as well as its contribution to the total reinforcement effects.
- The micro-mechanical mechanism that is producing the Al-matrix hardening (stress transfer, dislocation pinning, grain-size effect, etc.) have to be described and quantified, as well as the possible interactions between *in-situ* and *ex-situ* reinforcements, or other phases formed inside the metallic matrix.

The computerized processing methods applied to the analysis or particle distributions that was illustrated with some examples in Chapter 4 has considerable potential for further researches:

- Statistical results of image processing should be put in relation with changes of mechanical properties that are critically influenced by reinforcement distribution (ductility, toughness);

- The described method could be extended to other types of microstructural images, obtained by mean of SEM, EDS mapping, TEM etc.
- The same procedure that has been used for particles distribution will be applied to evaluation of porosity, which is critical for properties of BMGFs that are described in Chapter 2.

5.4. Applicative research for new industrial products and technologies

Technical assistance activities for industrial companies from the western part of Romania will be continued based on already existent solid partnership relations. Future research activities will promote especially the transfer of knowledge related to advanced materials and new processing technologies.

Acknowledgements

Accomplishment of the scientific contributions presented in this habilitation thesis have significantly benefited of support from Romanian and international institutions.

The access to the facilities of the Leibniz Institute for Solid State and Materials Research (IFW) Dresden was supported by German Academic Exchange Service (Deutscher Akademischer Austausch Dienst – DAAD) with the kind recommendation of prof. Jürgen Eckert, director of IFW and exquisite help of Dr. Mihai Stoica, head of department at the same institute, to whom the author will be forever in debt. Special thanks to the staff of IFW, especially to Mariana Calin, Ramasamy Parthiban, Birgit Opitz, Birgit Bartusch, Harald Merker, and Sven Donath.

Researches in the field of DRAMCs was supported by UEFISCDI Romania, within the frame of the Grant PN-II-PT-PCCA-2011-3.2-0423 CERMETSINTREACT

Investigations were performed in the laboratories of Politehnica University Timișoara, department of Materials and Manufacturing Engineering, and microscopy center of the Research Institute for Renewable Energy (ICER). Special thanks go to the colleagues of PUT who sustained these efforts and provided valuable contributions - Cosmin Locovei, Aurel Raduta, Carmen Opriș, Dragos Buzdugan, Lazăr Soveja, Traian Bena. The author is grateful to prof. Viorel Aurel Serban for fruitful discussions and encouragement.

Some structural investigations were also performed at the Technical University Cluj-Napoca, with the kind assistance of prof. Ioan Vida-Simiti, prof. Ionel Chicinaș and dr. Gyorgy Thalmaier.

Preliminary determinations of biocompatibility have benefited from the contributions of prof. Fabian Tatu and dr. Adrian Catalin Miu MD from ‘‘Victor Babeș” University of Medicine and Pharmacy. Some of the XRD investigations were completed at the National Institute for R. D. in Electrochemistry and Condensed Matter by Dr. Daniel Ursu.

Last, but not least, I am most grateful for the understanding, help and encouragement of my family.

References

[1] M. Nicoara, L. R. Cucuruz and I. Cartis, " Partikelverstäkter Verbundwerkstoffe – Particle-reinforced composites," *Metall,* no. 1-2, pp. 30-36, 2000.

[2] M. Nicoara and A. Raduta, "The Effect of Particle Reinforcement upon Precipitation of Secondary Phases in Composites with Aluminum Matrix," in *Summer School on Mechanical Spectroscopy Q-1*, Aussois, France, 2002.

[3] M. Nicoara, A. Raduta, C. Locovei and V.-A. Serban, "Contribution to Thermo-Mechanical Processing of Al-Based Particle-Reinforced Composites," in *Proceedings of the International Colloquium of the European Centre For Emerging Materials And Processes Dresden ECEMP 2010*, Dresden, 2010.

[4] M. Lita and M. Nicoara, "The Use of Amorphous And Quasi-Amorphous Fe–Cr–P-Powder for Fabrication of Magnetic Rheological Suspensions," *Journal of Magnetism and Magnetic Materials,* vol. 201, pp. 49-52, 1999.

[5] A. Raduta, M. Nicoara, C. Locovei, J. Eckert and M. Stoica, "Ti-based bulk glassy composites obtained by replacement of Ni with Ga," *Intermetallics,* vol. 69, pp. 28-34, 2016.

[6] A. Raduta, M. Nicoara, C. Locovei, M. Stoica and J. Eckert, "About Replacement of Nickel as Amorphization Element for Fabrication of Ultra-Rapidly Solidified Ti-Zr Alloys," in *Solid State Phenomena - Advanced Materials and Structures V*, Zurich, 2014.

[7] C. Locovei, M. Nicoara and A. Raduta, "Sample Preparation and HR-TEM Investigation Techniques of Ti Based, Ga Containing, Amorphous Alloys," in *Solid State Phenomena (Advanced Materials and Structures V)*, Zurich, 2014.

[8] M. Nicoara, C. Locovei, V. A. Serban, R. Parthiban, M. Calin and M. Stoica, "New Cu-Free Ti-Based Composites with Residual Amorphous Matrix," *Materials,* vol. 331, no. 9, pp. 1-14, 2016.

[9] M. Nicoara, A. Raduta, R. Parthiban, C. Locovei, J. Eckert and M. Stoica, "Low Young's modulus Ti-based porous bulk glassy alloy without cytotoxic elements," *Acta Biomaterialia,* vol. 36, pp. 323-331, 2016.

[10] M. Nicoara, A. Raduta, C. Locovei, D. Buzdugan and M. Stoica, "About Thermostability of Biocompatible Ti-Zr-Ta-Si Amorphous Alloys," *Journal of Thermal Analysis and Calorimetry,* vol. 124, pp. 1-7, 2016.

[11] A. Raduta, M. Nicoara and C. Locovei, "About Thermostability of Fe-Ni-P Amorphous Alloys," in *Solid State Phenomena-Advanced Materials and Structures IV*, Zurich, 2012.

[12] G. Thalmaier, I. Vida-Simiti, N. Jumătate, V. A. Şerban, C. Codrean, M. Nicoară and L. Bukkosi, "Thermal Stability of Ni40Ti40Nb20 and Ni32Ti48Nb20 Tapes Obtained by Rapid Solidification Technique," in *Solid State Phenomena - Advanced Materials and Structures IV*, Zurich, 2012.

[13] M. Nicoara, C. Locovei, C. Opris, D. Ursu, R. Vasiu and M. Stoica, "Optimizing the parameters for in-situ fabrication of hybrid al-Al2O3 composites," *Journal of Thermal Analysis and Calorimetry,* vol. in press, 2016.

[14] M. Nicoara, A. Raduta and C. Locovei, "Computerized Image Processing for Evaluation of Microstructure in Metallic Matrix Composites," *Solid State Phenomena,* vol. 188, no. Advanced Materials and Structures IV, pp. 124-133 , 2012.

[15] M. Nicoara, A. Raduta and C. Locovei, "Computer-aided evaluation of particle distribution in metallic matrix composites," in *Proceedings of the European International Powder Metallurgy Congress and Exhibition - Euro PM 2011*, Barcelona, 2011.

[16] C. Locovei, M. Nicoara, A. Raduta and V.-A. Serban, "Contributions to computer-aided evaluation of microstructure for particle reinforced composites by mean of image processing," in *Proceedings of the 4th International Conference "Advanced Composite Materials Engineering"* , Brasov, 2012.

[17] D. E. Alman, "Properties of Metal-Matrix Composites," in *ASM Handbook, vol. 21 Composites*, vol. 21, Novelty, OH: ASM International, 2001.

[18] J. Eckert, J. Das, S. Pauly and C. Duhamel, "Mechanical properties of bulk metallic glasses and composites," *J. Mater. Res.,* vol. 22, no. 2, pp. 285-301, February 2007.

[19] K. Hajlaoui, A. Yavari, J. Das and G. Vaughan, "Ductilization of BMGs by optimization of nanoparticle dispersion," *Journal of Alloys and Compounds,* vol. 434–435, p. 6–9, 2007.

[20] J. Li, H. Lin, J. K. C. Jang and J. Huang, "Novel open-cell bulk metallic glass foams with promising characteristics," *Materials Letters,* no. 105, p. 140–143, 2013.

[21] A. Mortensen and J. Llorca, "Metal Matrix Composites," *Annual Review of Materials Research,* vol. 40, p. 243–270, 2010.

[22] M. O. Bodunrin, K. K. Alaneme and L. H. Chown, "Aluminium matrix hybrid composites: a review of reinforcement philosophies; mechanical, corrosion and tribological characteristics," *Journal of Materials Research and Technology,* vol. 4, no. 4, pp. 434-445, 2015.

[23] R. Casati and M. Vedani, "Metal Matrix Composites Reinforced by Nano-Particles—A Review," *Metals,* vol. 4, pp. 65-83, 2014.

[24] L. Lü, M. Lai, Y. Su, H. Teo and C. Feng, "In situ TiB2 reinforced Al alloy composites," *Scripta Materialia,* vol. 45, no. 9, p. 1017–1023, 2001.

[25] R. B. S. B., K. Das and S. Das, "A review on the synthesis of in situ aluminum based composites by thermal, mechanical and mechanical–thermal activation of chemical reactions," *Journal of Materials Science,* vol. 42, p. 9366–9378, 2007.

[26] M. A.-H. Gepreel and M. Niinomi, "Biocompatibility of Ti-alloys for long-term implantation," *Journal of the mechanical behavior of biomedical materials,* vol. 20, p. 407–415, 2013.

[27] M. Niinomi, Metals for Biomedical Devices, Woodhead Publishing, 2010.

[28] B. Basu, D. S. Katti and A. Kumar, Advanced Biomaterials — Fundamentals, Processing, and Applications, Wiley, 2009.

[29] M. Geetha, A. Singh, R. Asokamani and A. Gogia, "Ti based biomaterials, the ultimate choice for orthopaedic implants - a review," *Progress in Materials Science,* vol. 54, p. 397–425, 2009.

[30] Y. Oshida, Bioscience and Bioengineering of Titanium Materials, Elsevier, 2007.

[31] M. M. Trexler and N. N. Thadhani, "Mechanical properties of bulk metallic glasses," *Progress in Materials Science,* vol. 55, p. 759–839, 2010.

[32] Q. Chen and G. A. Thouas, "Metallic implant biomaterials," *Materials Science and Engineering R 87,* p. 1–57, 2015.

[33] M. G. Abdel-Hady and M. Niinomi, "Biocompatibility of Ti-alloys for long-term implantation," *Journal of the Mechanical Behavior of Biomedical Materials,* vol. 20, pp. 407-415, 2013.

[34] Q. Chen and G. A. Thouas, "Metallic implant biomaterials," *Materials Science an Engineering R,* vol. 87, pp. 1-57, 2015.

[35] M. Niinomi, Metals for Biomedical Devices, CRC Press, 2010.

[36] M. Niinomi, "Mechanical biocompatibilities of titanium alloys for biomedical applications," *Journal of the Mechanical Behavior of Biomedical Materials,* vol. 1, no. 1, p. 30–42, 2008.

[37] A. Biesiekierski, J. Wang, M. A.-H. Gepreel and C. Wena, "A new look at biomedical Ti-based shape memory alloys," *Acta Biomaterialia,* vol. 8, p. 1661–1669, 2012.

[38] M. Calin, A. Gebert, A. C. Ghinea, P. F. Gostin, S. Abdi, C. Mickel and J. Eckert, "Designing biocompatible Ti-based metallic glasses for implant applications," *Materials Science and Engineering C,* pp. 875-833, 2013.

[39] F. Qin, Z. Dan, X. Wang, G. Xie and A. Inoue, "Ti-Based Bulk Metallic Glasses for Biomedical Applications," in *Biomedical Engineering, Trends in Materials Science*, Shanghai, InTech, 2011, pp. 249-266.

[40] M. Niinomi, "Recent Titanium R&D for Biomedical Applications in Japan," *Journal of the Minerals, Metals and Materials Society,* vol. 51, no. 6, pp. 32-34, June 1999.

[41] A. Inoue and A. Takeuchi, "Recent development and application products of bulk glassy alloys," *Acta Materialia 59,* pp. 2243-2267, 2011.

[42] A. L. Greer, "Metallic glasses... on the threshold," *Materials Today,* vol. 12, no. 1-2, pp. 14-23, Jan-Feb 2009.

[43] A. Yavari, J. Lewandowski and J. Eckert, "Mechanical Properties of Bulk Metallic Glasses," *MRS BULLETIN,* pp. 635-638, August 2007.

[44] E. Axinte, "Metallic glasses from ‘‘alchemy’’ to pure science: Present and future of design, processing and applications of glassy metals," *Materials and Design,* vol. 35, p. 518–556, 2012.

[45] J. Schroers, G. Kumar, T. M. Hodges, S. Chan and T. R. Kyriakides, "Bulk Metallic Glasses for Biomedical Applications," *JOM,* vol. 61, no. 9, pp. 21-29, 2009.

[46] W. Klement, R. H. Willens and P. Duwez, "Non-crystalline structure in solidifed Gold-Silicon alloys," *Nature,* vol. 187, no. 4740, p. 869–870, 1960.

[47] A. Inoue, "Stabilization of metallic supercooled liquid," *Acta mater. 48,* pp. 279-306, 2000.

[48] A. Inoue, "Stabilization of metallic supercooled liquid and bulk amorphous alloys," *Acta mater. 48,* no. 48, pp. 279-306, 2000.

[49] A. Peker and W. Johnson, "Beryllium bearing amorphous metallic alloys formed," *US Patent 5 288 344,* 1994.

[50] F. Guo, H.-J. Wang, J. S. Poon and G. J. Shiflet, "Ductile titanium-based glassy alloy ingots," *APPLIED PHYSICS LETTERS,* p. 091907, 2005.

[51] T. Zhang and A. Inoue, "Ti-based amorphous alloys with a large supercooled liquid region," *Materials Science and Engineering,* vol. A304–306, p. 771–774, 2001.

[52] D. Louzguine and A. Inoue, "Nanocrystallization of Ti-Ni-Cu-Sn amorphous alloy," *Scripta materialia,* vol. 43, p. 371–376, 2000.

[53] J. Fornell, N. V. Steenberge, S. Suriñach, M. Baró and J. Sort, "Influence of the Si content on the microstructure and mechanical properties of Ti–Ni–Cu–Si–Sn nanocomposite alloys," *Journal of Alloys and Compounds,* vol. 536, pp. 186-189, 2012.

[54] J. Park, H. Chang, K. Han, W. Kim and D. Kim, "Enhancement of plasticity in Ti-rich Ti–Zr–Be–Cu–Ni bulk metallic glasses," *Scripta Materialia,* vol. 53, pp. 1-6, 2005.

[55] P. Gong, K.-F. Yao, X. Wang and Y. Shao, "Centimeter-sized Ti-based bulk metallic glass with high specific strenght," *Progress in Natural Science: Materials International,* vol. 22, pp. 401-406, 5 2012.

[56] P. Gong, K. Yao and Y. Shao, "Effect of Fe addition on glass-forming ability and mechanical properties of Ti-Zr-Be bulk metallic glass," *Journal of Alloys and Compounds,* vol. 536, pp. 26-29, 2012.

[57] M. Tang, H. Zhang, Z. F. H. Zhu, A. Wang, H. Li and Z. Hu, "TiZr-base Bulk Metallic Glass with over 50 mm in Diameter," *J. Mater. Sci. Technol.,* vol. 26(6, pp. 481-486, 2010.

[58] S. L. Zhu, X. M. Wang, F. X. Qin, M. Yoshimura and A. Inoue, "New TiZrCuPd Quaternary Bulk Glassy Alloys with Potential of Biomedical Applications," *Materials Transactions, Vol. 48, No. 9,* pp. 2445-2448, 2007.

[59] M. Jakubowski and C. PałczyŃski, "Chapter 30 – Beryllium," in *Handbook on the Toxicology of Metals*, Academic Press, 2015.

[60] H. Wang, E. Park, A. D. Setywan, S. Zhu, X. M. Wang, T. A. and H. Kato, "Effect of cobalt microalloying on the glass forming ability of Ti-Cu-Pd-Zr metallic-glass," *Journal of Non-Crystalline Solids, 379,* pp. 155-160, 2013.

[61] Z. Suo, K. Qiu, Q. Li, Y. Ren and Z. Hu, "Effect of Nb on glass forming ability and plasticity of (Ti–Cu)-based bulk," *Materials Science and Engineering A 527,* p. 2486–2491, 2010.

[62] S. Zhu, X. Wang and A. Inoue, "Glass-forming ability and mechanical properties of Ti-based bulk," *Intermetallics 16,* p. 1031–1035, 2008.

[63] J.-J. Oak, D. V. Louzguine-Luzgin and A. Inoue, "Fabrication of Ni-free Ti-based bulk-metallic glassy alloy having potential for application as biomaterial, and investigation of its mechanical properties, corrosion, and crystallization behavior," *Journal of Materials Research,* vol. 22, no. 5, pp. 1346-1353, 2007.

[64] H. Wang, E. Park, J. Oak, A. Setyawan, S. Zhu, T. Wada, X. Wang, A. Takeuchi and H. Kato, "Effect of cobalt microalloying on the glass forming ability of Ti-Cu-Pd-Zr metallic-glass," *Journal of Non-Crystalline Solids,* vol. 379, pp. 155-160, 2013.

[65] J.-J. Oak, D. V. Louzguine-Luzgin and A. Inoue, "Fabrication of Ni-free Ti-based bulk-metallic glassy alloy having potential for application as biomaterial, and investigation of its mechanical properties, corrosion, and crystallization behavior," *Journal of Materials Research,* vol. 22, no. 5, pp. 1346-1353, 2007.

[66] N. Zheng, R. T. Qu, S. Pauly, M. Calin, T. Gemming, Z. F. Zhang and J. Eckert, "Design of ductile bulk metallic glasses by adding “soft” atoms," *APPLIED PHYSICS LETTERS,* vol. 100, pp. 1-4, 2012.

[67] F. X. Qin, X. M. Wang and A. Inoue, "Effects of Ta on Microstructure and Mechanical Property of Ti-Zr-Cu-Pd-Ta Alloys," *Materials Transactions,* vol. 48, no. 9, pp. 2390-2394, 2007.

[68] J.-J. Oak, H. Kimura and A. Inoue, "Effects of Additional Elements on Structure, Mechanical Strength and Chemical Properties of Ni-free Ti-based Bulk Metallic Glasses for Biomaterials," *Advanced Materials Research,* Vols. 26-28, pp. 785-788, 2007.

[69] F. Qin, X. Wang, G. Xie and A. Inoue, "Distinct plastic strain of Ni-free Ti–Zr–Cu–Pd–Nb bulk metallic glasses with potential for biomedical applications," *Intermetallics,* vol. 16, p. 1026–1030, 2008.

[70] J.-J. Oak, G.-W. Hwang, Y.-H. Park, H. Kimura, S.-Y. Yoon and A. Inoue, "Characterization of Surface Properties, Osteobalst Cell Culture in Vitro and Processing with Flow-Viscosity of Ni-Free Ti-Based Bulk Metallic Glass for Biomaterials," *Journal of Biomechanical Science and Engineering ,* vol. 4, no. 3, pp. 384-391, 2009.

[71] K. Merritt, "Role of medical materials, both in implant and surface applications, in immune response and in resistance to infection," *Biomaterials,* vol. 5, pp. 47-53, 1984.

[72] E. Schlede, W. Aberer, T. Fuchs, I. Gerner, H. Lessmann, T. Maurer, R. Rossbacher, G. Stropp, E. Wagner and D. Kayser, "Chemical substances and contact allergy - 244 substances ranked according to allergenic potency," *Toxicology,* no. 193, pp. 219-259, 2003.

[73] A. Biesiekierski, J. Wang, M. A.-H. Gepreel and C. Wen, "A new look at biomedical Ti-based shape memory alloys," *Acta Biomaterialia 8,* p. 1661–1669, 2012.

[74] J. Hornez, A. Lefevre, D. Joly and H. Hildebrand, "Multiple parameter cytotoxicity index on dental alloys and pure metals," *Biomolecular Engineering,* vol. 19, pp. 103-117, 2002.

[75] W. M. Elshahawy, I. Watanabe and P. Kramer, "In vitro cytotoxicity evaluation of elemental ions released from different prosthodontic materials," *Dental materials,* vol. 25, pp. 1551-1555, 2009.

[76] D. Kuroda, M. Niinomi, M. Morinaga, Y. Kato and T. Yashiro, "Design and mechanical properties of new b type titanium alloys for implant materials," *Materials Science and Engineering A,* vol. 243, pp. 244-249, 1998.

[77] M. Long and H. Rack, "Titanium alloys in total joint replacement—a materials science perspective," *Biomaterials,* vol. 19, pp. 1621-1639, 1998.

[78] H. Lin, P. Tsai, J. Ke, J. Li, J. Jang, C. Huang and J. Haung, "Designing a toxic-element-free Ti-based amorphous alloy with remarkable supercooled liquid region for biomedical application," *Intermetallics,* no. 55, pp. 22-27, 2014.

[79] S. Abdi, M. Samadi Khoshkhoo, O. Shuleshova, M. Bönisch, M. S. L. E. J. Calin, M. Baró, J. Sort and A. Gebert, "Effect of Nb addition on microstructure evolution and nanomechanical properties of a glass-forming TiZrSi alloy," *Intermetallics,* no. 46, pp. 156-163, 2014.

[80] J.-J. Oak and A. Inoue, "Formation, mechanical properties and corrosion resistance of Ti–Pd base glassy alloys," *Journal of Non-Crystalline Solids ,* no. 354, p. 1828–1832, 2008.

[81] J.-J. Oak and A. Inoue, "Attempt to develop Ti-based amorphous alloys for biomaterials," *Materials Science and Engineering A,* no. 449–451, p. 220–224, 2007.

[82] J. Ke, C. Huang, Y. Chen, W. Tsai, T. Wei and J. Huang, "In vitro biocompatibility response of Ti–Zr–Si thin film metallic glasses," *Applied Surface Science,* no. 322, pp. 41-46, 2014.

[83] C. Lin, C. Huang, J. Chuang, J. Huang, J. Jang and C. Chen, "Rapid screening of potential metallic glasses for biomedical applications," *Materials Science and Engineering C,* vol. 33, p. 4520–4526, 2013.

[84] K. Zhuravleva, A. Chivu, A. Teresiak, S. Scudino, M. Calin, L. Schultz, J. Eckert and G. A., "Porous low modulus Ti40Nb compacts with electrodeposited hydroxyapatite coating for biomedical applications,," *Materials Science and Engineering C 33 (2013) ,* vol. 33, pp. 2280-2287, 2013.

[85] W. Xue, B. V. Krishna, A. Bandyopadhyay and S. Bose, "Processing and biocompatibility evaluation of laser processed porous titanium," *Acta Biomaterialia,* no. 3, p. 1007–1018, 2007.

[86] V. Karageorgiou and D. Kaplan, "Porosity of 3D biomaterial scaffolds and osteogenesis," *Biomaterials,* no. 26, p. 5474–5491, 2005.

[87] C. Wen, Y. Yamada and P. Hodgson, "Fabrication of novel TiZr alloy foams for biomedical applications," *Materials Science and Engineering C,* vol. 26, p. 1439 – 1444, 2006.

[88] Y. Huang, J. Shen, J. Sun and X. Yu, "A new Ti–Zr–Hf–Cu–Ni–Si–Sn bulk amorphous alloy with high glass-forming ability," *Journal of Alloys and Compounds 427, Issues 1–2 Volume 427,* pp. 171-175, 2007.

[89] S. Pang, C.-H. Shek, C. I. A. Ma and T. Zhang, "Corrosion behavior of a glassy Ti–Zr–Hf–Cu–Ni–Si alloy," *Materials Science and Engineering: A, Volumes 449–451 ,* p. 557–560, 2007.

[90] P. Melnikov, A. Malzac and M. de Barros Coelho, "Gallium and bone pathology," *Acta Ortopedica Brasileira 16 (1),* pp. 54-57, 2008.

[91] E. Verron, M. Masson, S. Khoshniat, L. Duplomb, B. Bujoli, P. P. Janvier, J.-C. Scimeca, J.-M. Bouler and J. Guicheux, "The in vitro effects of gallium on bone cells," *Bone,* pp. 144-145, 2012.

[92] P. Melnikov, A. Teixeira, A. Malzac and M. d. B. Coelho, "Gallium-containing hydroxyapatite for potential use in orthopedics," *Materials Chemistry and Physics 117,* pp. 86-90, 2009.

[93] S. Valappil, D. Ready, E. Abou Neel, D. Pickup, L. O'Dell, W. Chrzanowski, J. Pratten, R. Newport, M. Smith, M. Wilson and J. Knowles, "Controlled delivery of antimicrobial gallium ions from phosphate-based glasses," *Acta Biomaterialia 5 ,* p. 1198–1210, 2009.

[94] G. Lusvardi, G. Malavasi, L. Menabue and S. Shruti, "Gallium-containing phosphosilicates: Functionalization and in-vitro bioactivity," *Materials Science and Engineering C, 33,* pp. 3190-3196, 2013.

[95] M. Franchini, G. Lusvardi, G. Malavasi and L. Menabue, "Gallium containing phospho-silicate glasses:Synthesis and in-vitro bioactivity," *Materials Science and Engineering C vol. 32,* pp. 1401-1406, 2012.

[96] S. Shruti, A. J. Salinas, G. ,. L. G. Malavasi, L. Menabue, C. Ferrara, P. Mustarelli and M. Vallet-Regi, "Structural and in vitro study of cerium, gallium and zinc containing sol–gel," *Journal of Materials Chemistry 22,* p. 13698–13706, 2012.

[97] A. Inoue, "Stabilization of metallic supercooled liquid and bulk amorphous alloys," *Acta materialia. 48,* pp. 279-306, 2000.

[98] O. M. D. Senkov, "Effect of the atomic size distribution on glass forming," *Materials Research Bulletin 36,* pp. 2138-2198, 2001.

[99] A. Takeuchi and A. Inoue, "Classification of bulk metallic glasses by atomic size difference, heat of mixing and period of constituent elements and its application to characterization of the main alloying element," *Materials Transactions, Vol. 46, No. 12,* pp. 2817-2829 , 2005.

[100] S. Sachdev and D. Nelson, "Theory of the structure factor of metallic glasses," *Physical Review Letters,* vol. 53, no. 20, pp. 1947-1950, 1984.

[101] K. F. Kelton, G. G.W. Lee, A. K. Gangopadhyay, R. Hyers, T. J. Rathz, J. R. Rogers, M. B. Robinson and D. S. Robinson, "First X-Ray Scattering Studies on Electrostatically Levitated Metallic Liquids: Demonstrated Influence of Local Icosahedral Order on the Nucleation Barrier," *Physical Review Letters,* vol. 90, no. 19, pp. 1-4, 2003.

[102] S. B. Goodman, Z. Yao, M. Keeney and F. Yang, "The future of biologic coatings for orthopaedic implants," *Biomaterials,* vol. 34, pp. 3174-3183, 2013.

[103] E. Schlede, W. Aberer, T. Fuchs, I. Gerner, H. Lessmann, T. Maurer, R. Rossbacher, G. Stropp, E. Wagner and D. Kayser, "Chemical substances and contact allergy - 244 substances ranked according to allergenic potency," *Toxicology,* vol. 193, pp. 219-259, 2003.

[104] J. Hornez, A. Lefevre, D. Joly and H. Hildebrand, "Multiple parameter cytotoxicity index on dental alloys and pure metals," *Biomolecular Engineering,* vol. 19, pp. 103-117, 2002.

[105] R. Craig and C. Hanks, "Cytotoxicity of Experimental Casting Alloys Evaluated by Cell Culture Tests," *Journal of Dental Research,* vol. 69, pp. 1539-1542, 1990.

[106] J. Wataha, P. Lockwood and A. Schedle, "Effect of silver, copper, mercury, and nickel ions on cellular proliferation during extended, low-dose exposures," *Journal of Biomedical Materials Research,* vol. 52, p. 360–364, 2000.

[107] S.-h. Hsu, H.-J. Tseng and Y.-C. Lin, "The biocompatibility and antibacterial properties of waterborne polyurethane-silver nanocomposites," *Biomaterials,* vol. 31, pp. 6796-6808, 2010.

[108] M. Long and H. Rack, "Titanium alloys in total joint replacement - a materials science perspective," *Biomaterials,* vol. 19, pp. 1621-1639, 1998.

[109] S. Stohs and D. Bagchi, "Oxidative mechanisms in the toxicity of metal ions," *Free Radical Biology & Medicine,* vol. 18, no. 2, pp. 321-336, 1995.

[110] O. Choi, C.-P. Yu, G. E. Fernandez and Z. Hua, "Interactions of nanosilver with Escherichia coli cells in planktonic and biofilm cultures," *Water Research,* vol. 44, pp. 6095 -6103, 2010.

[111] K. Kalishwaralal, S. BarathManiKanth, S. R. K. Pandian, V. Deepak and S. Gurunathan, "Silver nanoparticles impede the biofilm formation by Pseudomonas aeruginosa and Staphylococcus epidermidis," *Colloids and Surfaces B: Biointerfaces,* vol. 79, p. 340–344, 2010.

[112] K. D. Secinti, H. Özalp, A. Attar and M. F. Sargon, "Nanoparticle silver ion coatings inhibit biofilm formation on titanium implants," *Journal of Clinical Neuroscience,* vol. 18, p. 391–395, 2011.

[113] M. Abdel-Hady, K. Hinoshita and M. Morinaga, "General approach to phase stability and elastic properties of beta-type Ti-alloys using electronic parameters," *Scripta Materialia,* vol. 55, p. 477–480, 2006.

[114] J.-J. Oak, D. V. Louzguine-Luzgin and A. Inoue, "Synthetic relationship between titanium and alloying elements in designing Ni-free Ti-based bulk metallic glass alloys," *Applied Physics Letters,* vol. 91, pp. 1-4, 2007.

[115] ASM International, "Alloy Phase Diagram Database".

[116] T. Wada, A. Inoue and A. L. Greer, "Enhancement of room-temperature plasticity in a bulk metallic glass by finely dispersed porosity," *Applied Physical Letters,* vol. 86, no. 251907, pp. 1-2, 2005.

[117] A. H. Brothers and D. C. Dunand, "Syntactic bulk metallic glass foam," *Applied Physical Letters,* vol. 84, no. 1108, pp. 1-2, 2004.

[118] A. Inoue, "Stabilization of metallic supercooled liquid and bulk amorphous alloys," *Acta materialia,* vol. 48, pp. 279-306, 2000.

[119] C. Suryanarayana and A. Inoue, Bulk Metallic Glasses, CRC Press, Taylor & Francis Group, 2011.

[120] A. Inoue, F. Kong, S. Zhu, E. Shalaan and F. Al-Marzouki, "Production methods and properties of engineering glassy alloys and composites," *Intermetallics,* vol. 58, pp. 20-30, 2015.

[121] J. Schroers, T. M. Hodges, G. Kumar, H. Raman, A. J. Barnes, Q. Pham and T. A. Waniuk, "Thermoplastic blow-molding of metals," *Materials Today,* vol. 14, no. 1-2, pp. 14-19, 2011.

[122] A. Inoue and A. Takeuchi, "Recent development and application products of bulk glassy alloys," *Acta Materialia,* vol. 59, p. 2243–2267, 2011.

[123] A. Inoue, T. Wada and D. Louzguine-Luzgin, "Improved mechanical properties of bulk glassy alloys containing spherical pores," *Materials Science and Engineering A,* vol. 471, no. 1-2, pp. 144-150, 2007.

[124] C. Wen, Y. Yamada and P. Hodgson, "Fabrication of novel TiZr alloy foams for biomedical applications," *Materials Science and Engineering C,* vol. 26, p. 1439 – 1444, 2006.

[125] G. Ryan, A. Pandit and D. P. Apatsidis, "Fabrication methods of porous metals for use in orthopaedic applications," *Biomaterials,* vol. 27, p. 2651–2670, 2006.

[126] Y. Tian, S. Ding, H. Peng, S. Lu, G. Wang, L. Xia and P. Wang, "Osteoblast growth behavior on porous-structure titanium surface," *Applied Surface Science,* no. 261, p. 25– 30, 2012.

[127] G. Xie, F. Qin, S. Zhu and D. Louzguine-Luzgin, "Corrosion behaviour of porous Ni-free Ti-based bulk metallic glass produced by spark plasma sintering in Hanks' solution," *Intermetallics,* vol. 44, pp. 55-59, 2014.

[128] T. M. Keaveny, E. F. Morgan and O. C. Yeh, "Bone mechanics," in *Standard Handbook of Biomedical Engineering and Design*, New York, Digital Engineering Library @ McGraw-Hill, 2003.

[129] C. Suryanarayana and A. Inoue, Bulk metallic glasses, CRC Press, 2011.

[130] M. G. Scott, Crystallization in Amorphous Metallic Alloys, Butterworth & Co Publishers Ltd., 1983.

[131] J. Yu, T. Jing, J. Yang and Q. Li, "Determination of activation energy for crystallizations in Ni–Sn–P amorphous alloys," *Journal of Materials Processing Technology,* vol. 209, p. 14–17, 2009.

[132] A. P. Srivastava, D. Srivastava, B. Mazumdar and G. K. Dey, "Thermoanalytical study of crystallization process in metallic glass of Co69Fe3Si18B10," *J Therm Anal Calorim,* vol. 119, no. DOI:10.1007/s10973-014-4231-3, p. 1353–1361, 2015.

[133] J. Wu, Y. Pan and J. Pi, "On non-isothermal kinetics of two Cu-based bulk metallic glasses," *J Therm Anal Calorim,* vol. 115, no. DOI:10.1007/s10973-013-3288-8, pp. 267-274, 2014.

[134] G. Strbac, D. Strbac, S. Lukic-Petrovic and M. Siljegovic, "Thermal characterization of glasses from Fe–Sb–S–I system," *J Therm Anal Calorim,* no. DOI:10.1007/s10973-016-5382-1, 2016.

[135] R. Svoboda and J. Malek, "Amorphous-to-crystalline transition in Te-doped Ge2Sb2Se5 glass," *J Therm Anal Calorim,* vol. 117, no. DOI:10.1007/s10973-014-3910-4, p. 1073–1083, 2014.

[136] R. Svoboda and J. Malek, "Is the original Kissinger equation obsolete today?," *J Therm Anal Calorim,* vol. 115, no. DOI:10.1007/s10973-013-3486-4, p. 1961–1967, 2014.

[137] H.-d. Wei, Q.-h. Bao, C.-x. Wang, W.-s. Zhang, Z.-Z. Yuan and X.-d. Chen, "Crystallization kinetics of (Ni0.75Fe0.25)78Si10B12 amorphous alloy," *Journal of Non-Crystalline Solids,* vol. 354, p. 1876–1882, 2008.

[138] J. Zhang, W. Wang, H. Ma, G. Li, R. Lia and Z. Zhang, "Isochronal and isothermal crystallization kinetics of amorphous Fe-based alloys," *Thermochimica Acta,* vol. 505, p. 41–46, 2010.

[139] H. E. Khalifa and K. S. Vecchio, "Thermal stability and crystallization phenomena of low cost Ti-based bulk metallic glass," *Journal of Non-Crystalline Solids,* vol. 357, p. 3393–3398, 2011.

[140] A. Pratap, T. L. S. Rao, K. N. Lad and H. D. Dhurandhar, "Kinetics of crystallization of titanium based binary and ternary amorphous alloys," *Journal of Non-Crystalline Solids,* vol. 353, p. 2346–2349 , 2007.

[141] S. Kasyap, A. T. Patel and A. Pratap, "Crystallization kinetics of Ti20Zr20Cu60 metallic glass by isoconversional methods using modulated differential scanning calorimetry," *J Therm Anal Calorim,* vol. 116, no. DOI:10.1007/s10973-014-3753-z, p. 1325–1336, 2014.

[142] X. C. Lu and H. Y. Li, "Kinetics of non-isothermal crystallization in Cu50Zr43Al7 and (Cu50Zr43Al7)95Be5 metallic glasses," *J Therm Anal Calorim,* vol. 115, no. DOI:10.1007/s10973-013-3364-0, p. 1089–1097, 2014.

[143] Y. Huang, J. Shen, J. Sun and X. Yu, "A new Ti–Zr–Hf–Cu–Ni–Si–Sn bulk amorphous alloy with high glass-forming ability," *Journal of Alloys and Compounds,* vol. 427, no. 1-2, pp. 171-175, 2007.

[144] M. X. Xia, C. L. Ma, H. X. Zheng and J. G. Li, "Preparation and crystallization of Ti53Cu27Ni12Zr3Al7Si3B1 bulk metallic glass with wide supercooled liquid region," *Materials Science and Engineering A,* vol. 390, p. 372–375, 2005.

[145] M. X. Xia, H. X. Zheng, L. Jian, C. L. Ma and J. G. Li, "Thermal stability and glass-forming ability of new Ti-based bulk metallic glasses," *Journal of Non-Crystalline Solids ,* vol. 351, p. 3747–3751, 2005.

[146] P. Gong, X. Wang and K. Yao, "Effects of alloying elements on crystallization kinetics of Ti–Zr–Be bulk metallic glass," *J Mater Sci,* vol. 51, p. 5321–5329, 2016.

[147] P. Gong, K. Yao and S. Zhao, "Cu-alloying effect on crystallization kinetics of Ti41Zr25Be28Fe6 bulk metallic glass," *J Therm Anal Calorim,* vol. 121, no. DOI 10.1007/s10973-015-4549-5, p. 697–704, 2015.

[148] H. Kishimura and H. Matsumoto, "Fabrication of Ti–Cu–Ni–Al amorphous alloys by mechanical alloying and mechanical milling," *Journal of Alloys and Compounds,* vol. 509, p. 4386–4389, 2011.

[149] Z. Yanxin, Z. Deqian, Z. W. W. Yong and P. Mingxiang, "Kinetics of glass transition and crystallization of multicomponent bulk amorphous alloys," *Science in China A,* vol. 43, no. 11, 2000.

[150] S. R. Prajapati, S. Kasyap, A. T. Patel and A. Pratap, "Non-isothermal crystallization kinetics of Zr52Cu18Ni14Al10Ti6," *J Therm Anal Calorim,* vol. 124, no. doi: 10.1007/s10973-015-4979-0, pp. 21-33, 2016.

[151] M. Stoica, R. Li, A. R. Yavari, G. Vaughan, J. Eckert, N. Van Steenberge and D. Ruiz Romera, "Thermal stability and magnetic properties of FeCoBSiNb bulk metallic glasses," *Journal of Alloys and Compounds,* vol. 504S, pp. 123-128, 2010.

[152] M. Ashby and A. Greer, "Metallic glasses as structural materials," *Scripta Materialia,* vol. 54, no. February, p. 321–326, 2006.

[153] J.-J. Oak, D. V. Louzguine-Luzgin and A. Inoue, "Fabrication of Ni-free Ti-based bulk-metallic glassy alloy having potential for application as biomaterial, and investigation of its mechanical properties, corrosion, and crystallization behavior," *Journal of Materials Research,* vol. 22, no. 5, pp. 1346-1353, 2007.

[154] T. Kokubo, H. Kushitani, S. Sakka, T. Kitsugi and T. Yamamuro, "Solutions able to reproduce in vivosurface-structure changes in bioactive glass-ceramic A-W," *J. Biomed. Mater. Res.,* vol. 24, pp. 721-734, 1990.

[155] T. Kokubo, S. Ito, Z. T. Huang, T. Hayashi, S. Sakka, T. Kitsugi and T. Yamauro, "Ca,P-rich layer formed on high-strength bioactive glass-ceramic A-W," *J. Biomed. MAter. Res.,* vol. 24, pp. 331-343, 1990.

[156] K. U. Kainer, Metal Matrix Composites. Custom-made Materials for Automotive and Aerospace Engineering, Weinheim: WILEY-VCH, 2006.

[157] N. Chawla and K. Chawla, Metal Matrix Composites, New York: Springer, 2006.

[158] D. Miracle, "Metal matrix composites – From science to technological significance," *Composites Science and Technology,* vol. 65, p. 2526–2540, 2005.

[159] T. W. Clyne and P. J. Withers, Introduction to Metal Matrix Composites, Cambridge: Cambridge University Press, 1993.

[160] H. Carvalhinhos, T. Marcelo and M. Carvalho, "Geometrical Limitation to the Homogenous Mixing of Metal and Ceramic Powders on Fabricating Al

Matrix/SiC Composites," in *Proceedings of the Tenth International Conference on Composite Materials: Processing and manufacturing*, Whistler, 1995.

[161] D. J. Whittenberger, T. K. Glasgow, M. Taya and H. Lilholt, Mechanical Properties of Metallic Composites, S. 0chiai, Ed., New York: Marcel Dekker, 1994.

[162] M. Nicoara, R. L. Cucuruz and I. Cartis, "Partikelverstäkter Verbundwerkstoffe," *Metall,* no. 1-2, 1999.

[163] S. Scudino, G. Liu, M. Sakaliyska, K. Surreddi and J. Eckert, "Powder metallurgy of Al-based metal matrix composites reinforced with β-Al3Mg2 intermetallic particles: Analysis and modeling of mechanical properties," *Acta Materialia,* vol. 57, no. 15, pp. 4529-4538, 2009.

[164] Z.-C. Chen, T. Takeda and K. Ikeda, "Microstructural evolution of reactive-sintered aluminum matrix composites," *Composites Science and Technology,* vol. 68, p. 2245–2253, 2008.

[165] B. S. B. Reddy, K. Das and S. Das, "A review on the synthesis of in situ aluminum based composites by thermal, mechanical and mechanical–thermal activation of chemical reactions," *Journal of Materials Science,* vol. 42, p. 9366–9378, 2007.

[166] S. Tjong and Z. Ma, "Microstructural and mechanical characteristics of in situ metal matrix composites," *Materials Science and Engineering,* vol. 29, pp. 49-113, 2000.

[167] L. Duraes, B. F. Costa, R. Santos, A. Correia, J. Campos and A. Portugal, "Fe2O3/aluminum thermite reaction intermediate and final products characterization," *Materials Science & Engineering A,* vol. 465, pp. 199-210, 2007.

[168] J. Mei, R. Halldearn and P. Xiao, "Mechanisms of the aluminium-iron oxide thermite reaction," *Scripta Materialia,* vol. 41, no. 5, p. 541–548, 1999.

[169] R.-H. Fan, H.-L. Lu, K.-N. Sun, W.-X. Wang and X.-B. Yi, "Kinetics of thermite reaction in Al-Fe2O3 system," *Thermochimica Acta,* vol. 440, p. 129–131, 2006.

[170] Y. Wang, X.-L. Song, W. Jiang, G.-D. Deng, X.-D. Guo, H.-Y. Liu and F.-S. Li, "Mechanism for thermite reactions of aluminum/iron-oxide nanocomposites based on residue analysis," *Trans. Nonferrous Met. Soc. China,* vol. 24, p. 263−270, 2014.

[171] S. Gedevanishvili and S. Deevi, "Processing of iron aluminides by pressureless sintering through Fe+Al elemental route," *Materials Science and Engineering A ,* vol. 325, no. 1-2, p. 163–176, 2002.

[172] D. Joslin, D. Easton, C. Liu, S. Babu and S. David, "Processing of Fe3Al and FeAl alloys by reaction synthesis," *Intermetallics,* vol. 3, no. 6, p. 467–481, 1995.

[173] E. Pochec, S. K. K. Jozwiak and Z. Bojar, "Fe–Al phase formation around SHS reactions under isothermal conditions," *Journal of Alloys and Compounds,* vol. 509, p. 1124–1128, 2011.

[174] D. Joslin, D. Easton, C. Liu and S. David, "Reaction synthesis of Fe-Al alloys," *Materials Science and Engineering A ,* vol. 192–193, no. 2, p. 544–548, 1995.

[175] H. Gao, Y. He, P. Shen, J. Zou, N. Xu, Y. Jiang, B. Huang and C. Liu, "Porous FeAl intermetallics fabricated by elemental powder reactive synthesis," *Intermetallics,* vol. 17, no. 12, pp. 1041-1046, 2009.

[176] S. Jóźwiak, K. Karczewski and Z. Bojar, "Kinetics of reactions in FeAl synthesis studied by the DTA technique and JMA model," *Intermetallics,* vol. 18, no. 7, p. 1332–1337, 2010.

[177] P. Matysik, S. Jozwiak and T. Czujko, "The kinetics of non-isothermal iron and aluminum powder mixtures sintering in protective atmosphere," *Journal of Alloys and Compounds,* no. 549, p. 92–99, 2013.

[178] S. Hasani, M. Panjepour and Shamanian, "Oxidation and Kinetic Analysis of Pure Aluminum Powder under Nonisothermal Condition," *Open Access Scientific Reports,* no. 8, pp. 1-8, 2012.

[179] L. P. H. Jeurgens, W. G. Sloof, F. D. Tichelaar and E. Mittemeijer, "Thermodynamic stability of amorphous oxide films on metals: Application to aluminum oxide films on aluminum substrates," *J.Physical Review B,* vol. 62, no. 7, pp. 4707-4719, 1999.

[180] M. Schoenitz, B. Patel, A. Osagie and E. L. Dreizin, "Oxidation of aluminum powders at high heating rates," *Thermochimica Acta,* vol. 507–508, p. 115–122, 2010.

[181] F. S. Yen, H. S. Lo, H. L. Wen and R. J. Yang, "Gamma- to Alfa-phase transformation subsystem induced by a-Al2O3-seeding in boehmite-derived nano-sized alumina powders," *Journal of Crystal Growth,* no. 249, p. 283–293, 2003.

[182] L. Jeurgens, W. Sloof, F. Tichelaar and E. Mittemeijer, "Structure and morphology of aluminium-oxide films formed by thermal oxidation of aluminium," *Thin Solid Films,* vol. 418, no. 2, p. 89–101, 2002.

[183] L. Jeurgens, W. Sloof, F. Tichelaar and E. Mittemeijer, "Composition and chemical state of the ions of aluminium-oxide films formed by thermal oxidation of aluminium," *Surface Science,* vol. 506, no. 3, p. 313–332, 2002.

[184] W. Gasior, A. Debski and Z. Moser, "Formation enthalpy of intermetallic phases from Al-Fe system measured with solution calorimetric method," *Intermetallics,* vol. 24, pp. 99-105, 2012.

[185] F. Haidara, M.-C. Record, B. Duployer and D. Mangelinck, "Phase formation in Al–Fe thin film systems," *Intermetallics,* vol. 23, no. 4, p. 143–147, 2012.

[186] Y. Xue, R. Shen, S. Ni, M. Song and D. Xiao, "Fabrication, microstructure and mechanical properties of Al–Fe intermetallic particle reinforced Al-based composites," *Journal of Alloys and Compounds,* vol. 618, p. 537–544, 2015.

[187] H. E. Kissinger, "Reaction Kinetics in Differential Thermal Analysis," *Analytical chemistry,* vol. 29, no. 11, pp. 1702-1706, 1957.

[188] N. M. Rendtorff, G. Suárez and E. F. Aglietti, "Non isothermal kinetic study of the aluminium titanate formation in alumina-titania mixtures," *Cerâmica,* vol. 60, pp. 411-416, 2014.

[189] K. A. Leyva-Gonzalez, R. Deaquino-Lara, D. Pourjafari, R. Martınez-Sanchez, M. A. L. Hernandez-Rodriguez and E. Garcıa-Sanchez, "Calorimetry study of the precipitation in an Al7075-graphite composite fabricated by mechanical alloying and hot extrusion," *J Therm Anal Calorim,* vol. 121, pp. 589-595, 2016.

[190] N. Hanene, D. M. Ibrahim and T. Abdelhafid, "The effect of heavy cold plastic deformation on the non-isothermal kinetics and the precipitation sequence of metastable phases in an Al–Mg–Si alloy," *J Therm Anal Calorim,* vol. 123, pp. 19-26, 2016.

[191] K. Bhanumurthy, W. Krauss and J. Konys, "Solid-State Diffusion Reaction and Formation of Intermetallic Phases in the Fe-Al System," *Fusion Science and Technology,* vol. 65, no. 2, pp. 262-272, 2014.

[192] L. Najman and T. Hugues, Eds., Mathematical morphology: from theory to applications, ISTE-Wiley, 2010.

[193] Imai, Kazuhiro and S. Hiromoto, "In vivo evaluation of Zr-based bulk metallic glass alloy intramedullary nails in rat femora," *Journal of Materials Science: Materials in Medicine,* vol. 25, p. 759–768, 2014.

[194] K. Imai, "In Vivo Investigation of Zr-Based Bulk Metallic Glasses Sub-Periosteally Implanted on the Bone Surface," *Journal of Materials Science and Chemical Engineering,* vol. 4, pp. 46-51, 2016.